High-resolution imaging with multi-parameter quantum metrology in passive remote sensing

Dissertation

der Mathematisch-Naturwissenschaftlichen Fakultät
der Eberhard Karls Universität Tübingen
zur Erlangung des Grades eines
Doktors der Naturwissenschaften
(Dr. rer. nat.)

vorgelegt von
Emre Köse
aus Niğde (Türkei)

Tübingen
2023

Gedruckt mit Genehmigung der Mathematisch-Naturwissenschaftlichen Fakultät der Eberhard Karls Universität Tübingen.

Tag der mündlichen Qualifikation:	22.05.2023
Dekan:	Prof. Dr. Thilo Stehle
1. Berichterstatter:	Prof. Dr. Daniel Braun
2. Berichterstatter:	Prof. Dr. Matteo Paris

Abstract

English Super-resolution quantum imaging is a recently developed technique that allows high-resolution imaging beyond the classical diffraction limit. To obtain super-resolution, one can use quantum tools, such as squeezed states, photon-number-resolving detectors, or mode demultiplexing, to get a better spatial or radiometric resolution. In this thesis, we study super-resolution imaging theoretically with a distant n-mode interferometer in the microwave regime. Interferometers play an essential role in passive remote sensing, particularly for observing the surface of the Earth in missions such as the Soil Moisture and Ocean Salinity (SMOS) mission. The SMOS is a passive remote sensing satellite in the microwave regime to measure the brightness temperature of Earth. The correlation of spatially-resolved electric field measurements obtained by SMOS helps determine Earth's surface's moisture level and ocean water's salinity and has a pixel size of approximately 35km. Our focus is a complete quantum mechanical analysis of estimating the parameters of the sources. Starting from the thermal distributions of microscopic currents on the surface leads to partially coherent quantum states of the electromagnetic field on the n-mode interferometer. In passive remote sensing, we have no control over the quantum states. However, we can look for a quantum enhancement in the measurement scheme. We combine incoming modes with an optimized unitary to achieve the optimal detection modes for that aim. This approach allows for the most informative measurement based on photon counting in the detection modes. It also saturates the quantum Cramér-Rao bound from the symmetric logarithmic derivative for the parameter set of temperatures. In our first work, we studied single-parameter estimation problems such as single source size, temperature, two-point source separation, and centroid. A quantum enhancement in spatial resolution is theoretically achievable for a single circular source to approximately 1m and less than 0.1 K when using the proposed maximum number of measurements with a single detector. We showed that one can resolve the source separation for any distance for two-point sources using the correct phase shift and a 50:50 beam splitter for a two-mode interferometer. The quantum Fisher information scales linearly with the number of modes when we keep the maximum

baseline constant for the array interferometer. In our second work, we focused on multiparameter estimations of the source temperature distributions. Unlike the single parameter case, quantum Cramér Rao Bound is not always saturable in the multiparameter scenario. It can be saturable asymptotically if the SLDs for different parameters commute on average. Then, one must find the optimal POVM, in our case, optimal unitary for mode mixing, to achieve the quantum limit. Our numerical analysis demonstrates quantum-enhanced super-resolution by reconstructing an image using the maximum likelihood estimator with a pixel size of 3 km. This resolution is ten times smaller than the spatial resolution of SMOS with comparable parameters. Furthermore, we identify the optimized unitary for uniform temperature distribution on the source plane, with the temperatures corresponding to the average temperatures of the image. Although this unitary was not optimized for the specific image, it yields a super-resolution compared to local measurement scenarios for the theoretically possible maximum number of measurements.

German Superauflösende Quantenbildgebung ist eine kürzlich entwickelte Technik, die eine hochauflösende Bildgebung jenseits der klassischen Beugungsgrenze ermöglicht. Um Superauflösung zu erreichen, kann man Quantenwerkzeuge wie gequetschte Zustände, Photonenzahl-auflösende Detektoren oder Moden-Demultiplexing einsetzen, um eine bessere räumliche oder radiometrische Auflösung zu erzielen. In dieser Arbeit untersuchen wir die superauflösende Bildgebung theoretisch mit einem entfernten n-Mode-Interferometer im Mikrowellenbereich. Interferometer spielen eine wesentliche Rolle in der passiven Fernerkundung, insbesondere bei der Beobachtung der Erdoberfläche in Missionen wie der Soil Moisture and Ocean Salinity (SMOS) Mission. SMOS ist ein passiver Fernerkundungssatellit im Mikrowellenbereich zur Messung der Helligkeitstemperatur der Erde. Die Korrelationen der mit SMOS gewonnenen räumlich aufgelösten elektrischen Feldmessungen helfen bei der Bestimmung des Feuchtigkeitsgehalts der Erdoberfläche und des Salzgehalts des Ozeanwassers und lösen Pixelgrößen von etwa 35 km auf. Unser Schwerpunkt liegt auf einer vollständigen quantenmechanischen Analyse zur Schätzung der Parameter der Quellen. Ausgehend von den thermischen Verteilungen der mikroskopischen Ströme auf der Oberfläche führt das zu teilkohärenten Quantenzuständen des elektromagnetischen Feldes auf dem n-Mode-Interferometer. Bei der passiven Fernerkundung haben wir keine Kontrolle über die Quantenzustände. Dennoch können wir nach einer Quantenverstärkung im Messverfahren suchen. Dafür kombinieren wir die eingehenden Moden mit einem optimierten unitären Operator, um die optimalen Detektionsmoden zu erreichen. Dieser Ansatz ermöglicht

die informativste Messung auf Grundlage der Photonenzählung in den Detektionsmodi. Er sättigt auch die Quanten-Cramér-Rao-Ungleichung aus der symmetrischen logarithmischen Ableitung für den Parametersatz der Temperaturen. In unserer ersten Arbeit untersuchten wir Probleme der Schätzung von Einzelparametern wie Größe der Einzelquelle, Temperatur, Zwei-Punkt-Quellentrennung und Schwerpunkt. Eine Quantenverbesserung der räumlichen Auflösung ist theoretisch für eine einzelne kreisförmige Quelle bis etwa 1 m und weniger als 0,1 K möglich, wenn die vorgeschlagene maximale Anzahl von Messungen mit einem einzigen Detektor verwendet wird. Wir haben gezeigt, dass man den Quellenabstand für beliebige Entfernungen für Zweipunktquellen auflösen kann, wenn man die richtige Phasenverschiebung und einen 50:50-Strahlenteiler für ein Zweimoden-Interferometer verwendet. Die Quanten-Fisher-Information skaliert linear mit der Anzahl der Moden, wenn wir die maximale Basislinie für das Array-Interferometer konstant halten. In unserer zweiten Arbeit haben wir uns auf Multiparameter-Schätzungen der Temperaturverteilungen der Quellen konzentriert. Im Gegensatz zum Ein-Parameter-Fall ist die Quanten-Cramér-Rao -Ungleichung im Mehr-Parameter-Szenario nicht immer sättigbar. Sie kann asymptotisch sättigbar sein, wenn die SLDs für verschiedene Parameter im Durchschnitt gleich sind. Dann muss man das optimale POVM finden, in unserem Fall der optimale unitäre Operator für die Modenmischung, um die Quantengrenze zu erreichen. Unsere numerische Analyse demonstriert die quantenverstärkte Superauflösung durch die Rekonstruktion eines Bildes mit dem Maximum-Likelihood-Schätzer mit einer Pixelgröße von 3 km. Diese Auflösung ist zehnmal kleiner als die räumliche Auflösung von SMOS mit vergleichbaren Parametern. Darüber hinaus ermitteln wir den optimierten unitären Operator für eine gleichmäßige Temperaturverteilung auf der Quellebene, wobei die Temperaturen den durchschnittlichen Temperaturen des Bildes entsprechen. Obwohl dieser unitäre Operator nicht für das spezifische Bild optimiert wurde, ergibt er eine Superauflösung im Vergleich zu lokalen Messszenarien für die theoretisch mögliche maximale Anzahl von Messungen.

List of publications and personal contribution

List of publications

1. E. Köse, G. Adesso, and D. Braun, *Quantum-enhanced passive remote sensing*, , Physical Review A **106**, 012601 (2022).

2. E. Köse, and D. Braun, *Super-Resolution Imaging with Multiparameter Quantum Metrology in Passive Remote Sensing*, Phys. Rev. A **107**, 032607 (2023)

Personal contribution of the candidate

No.	Author position	Scientific ideas (%)	Data generation (%)	Analysis and interpretation (%)	Paper writing (%)	Status
1	1	50	100	70	80	Published
2	1	50	100	70	80	Published

Acknowledgements

I would like to express my deepest gratitude to everyone who helped me complete this thesis.

First, I want to thank my advisor, Prof. Daniel Braun. This thesis would not have been possible without his expertise and insightful feedback. Above all, I am grateful for his patient guidance, enthusiastic encouragement, and valuable criticism at every stage of my Ph.D. from the first day I met him, I was fascinated by his unending curiosity, determination, and ability to understand physics. Ultimately, I will always be indebted to him for his extraordinary kindness and generosity in allowing me to join his research group.

I extend my appreciation to our collaborator Gerardo Adesso for his valuable insights and contributions and his guidance throughout the project. His critical feedback helped me to enhance the quality of our work.

Beyond the words, I thank every team member, especially Felix Spengler, for our fruitful discussions and for being good friends and colleagues from the beginning of my journey in Germany. I am thankful to Giovanni Gramegna, Ricardo Bellese, Matthias Hüls, Jakub Czartowski, and Jirawat Saiphet for their unwavering support, conversation, and cheering up whenever I needed it the most. I am grateful to Nadia Milazzo, Alessio Belenchia, Francis Headley, and Mahdi Rouhbakhshnabati for being excellent teammates and for their kind supporting personalities.

Many thanks to the love of my life, Gizem Özcan, for supporting me, always believing in me and encouraging me to pursue my passions. You always helped me stay motivated, especially during the most stressful times. Your love means everything to me, and I am truly fortunate to have you in this life by my side.

Lastly, I am thankful to my family members who have always believed in me, provided support and encouragement, and given me unconditional love.

Contents

Chapter 1

Framework

1.1 Introduction

This thesis focuses on applying quantum metrology to various imaging fields. The areas of interest include optical imaging of sub-wavelength structures in microscopy, imaging during astronomical observations, and lens-free imaging using phased optical arrays. In our calculations, we are particularly interested in the parameters of the SMOS, an array interferometer.

Conventionally, we have been using classical wave mechanics to calculate the best possible performance of microscopes, telescopes, and antenna arrays. As known almost 150 years ago, we have the bounds on resolution, such as the Abbe or Rayleigh diffraction limits, that limit resolution comparable to the wavelength of the used electromagnetic waves to distance how far we are away from the sources. At the same time, the van Cittert-Zernike theorem [46] limits resolution based on antenna arrays that record time-resolved electrical fields. However, it has become increasingly apparent in recent years that imaging analysis is too restrictive just using classical wave mechanics. Better experimental techniques like "super-resolved fluorescence microscopy" (Nobel Prize in Chemistry 2014) [18], in which one dresses a macro-molecule with point-like emitters selectively switched on and off, have helped resolve below the optical wavelength for imaging of macromolecules.

Over the last decade, quantum metrology has seen rapid growth. It is now well known that using non-classical quantum states can increase the precision with which specific parameters can be measured. So far, most of the quantum metrology community has focused on single-parameter estimation problems, like resolving the separation of the two-point sources, measuring magnetic fields, or temperature estimation. Thus, the quantum Cramér-Rao bound has become preferred for finding ultimate bounds for the sensitivity given specific resources such as the total available

energy, number of probes, or measurement time [22, 21]. It is optimized over all possible measurements and data-analysis schemes. In principle, it gives a bound that can be achieved in the limit of many measurements for the single-parameter estimation problems.

Tsang and his co-workers recently implemented quantum Cramér-Rao linked to imaging [42]. This caused immediate surprise and considerable excitement in the imaging community. They demonstrated that quantum Cramér-Rao allows a resolution well below the wavelength for estimating the distance between two equidistant emitters from an observer. They also suggested a method called SPADE (spatial mode demultiplexing), engineering of the modes in which light should be detected) that allows one to achieve such an advanced resolution. This work, meanwhile, has been generalized by relaxing constraints such as equal intensity or location in the same plane perpendicular to the line of sight of two sources.

Most of the interference effects in quantum optics rely on simple classical interference of the electromagnetic field modes. Classical mode interference gives rise to the resolution limits, such as the Abbe diffraction limit or the angular resolution of rays synthesized from a phased antenna array. However, since photons obey the laws of quantum mechanics, extra interference can happen at a much deeper level due to quantum interference in Hilbert space. Thus, quantum mechanical interference in Hilbert space can provide additional information. The quantum Cramér-Rao bound automatically considers all the information about the parameter in the quantum state of light. Detection of photons in different modes is involved in optimization over all possible measurement schemes for the parameter or a parameter vector. Also, once established, it can be used to determine optimum detection modes. A well-known example is the Hanbury-Brown-Twiss method, which determines the diameter of distant stars. It relies on receiving the light collected by the two telescopes as a function of the distances of the collected photons that provide access to the quantum correlation function, which contains information about the diameter of the emitting source that is not in the intensity distribution itself.

Helstrom considered the multi-parameter quantum estimation theory very beginning, leading to the multi-parameter quantum Cramer-Rao bound. It is a matrix-bound equal to the inverse of the quantum Fisher information matrix, which bounds the covariance matrix of the estimators of the parameters. However, unlike the single-parameter quantum Cramer-Rao bond, the multi-parameter quantum Cramer-Rao bond may not always be saturated. One reason is that the optimum quantum measurements typically required for each parameter are incompatible, meaning they cannot be measured simultaneously since the symmetric logarithmic

derivatives for different parameters do not commute. Recently, many questions arose in the quantum metrology community about when exactly the multi-parameter quantum Cramer-Rao bond can become saturated. A sufficient condition for the optimal quantum measurements for different parameters to be compatible is that the corresponding logarithmic derivatives commute. The Ref. [31] also finds a weaker sufficient condition: If the commutator of the symmetric logarithmic derivatives vanishes only on average over the quantum state, the bound can be saturated asymptotically; for pure states, that condition is also necessary [36].

Quantum multi-parameter estimation theory is developing very rapidly right now. This thesis aims to use these innovative techniques to establish ultimate quantum bounds for the performance of imaging techniques and measurement schemes for achieving them. For the first chapter, we will summarize the classical sources from the perspective of classical electromagnetic theory. Then we will continue with the semi-classical model depending on the minimal coupling between the classical sources and the quantized field modes. Further, we summarize the theoretical background for the classical and quantum parameter estimation theory. In the last chapter, we will summarize our results for the array interferometers based on our two papers in the Appendix.

1.2 Classical Analysis of Electromagnetic Field

1.2.1 Gauge Fields

In this section, I will give a simple introduction to gauge field theories. In general, we solve Maxwell's equations using the vector potential $\mathbf{A}(\mathbf{r}, t)$ and the scalar potential $\phi(\mathbf{r}, t)$, which are directly related to the magnetic and electric fields. As we know, these potentials are not unique and are subject to certain conditions known as gauge freedoms. The relation to electric $\mathbf{E}(\mathbf{r}, t)$ and magnetic $\mathbf{B}(\mathbf{r}, t)$ fields to vector and scalar potentials are given by the following equations

$$\mathbf{E} = -\nabla\phi - \frac{\partial \mathbf{A}}{\partial t}, \qquad \mathbf{B} = \nabla \times \mathbf{A}. \tag{1.1}$$

Then, $\nabla \cdot \mathbf{B} = 0$ (Gauss's law for magnetism) and $\nabla \times \mathbf{E} = -\frac{\partial \mathbf{B}}{\partial t}$ (Faraday's law of induction), both of the remaining Maxwell's equations are also satisfied. For any gauge, the two remaining equations lead to the following inhomogeneous wave

equations for the vector and the scalar potentials

$$\begin{aligned}\left(\nabla^2 - \frac{1}{c^2}\frac{\partial^2}{\partial t^2}\right)\mathbf{A} &= \nabla\left(\frac{1}{c^2}\frac{\partial\phi}{\partial t} + \nabla\cdot\mathbf{A}\right) - \mu_0\mathbf{j},\\ -\nabla^2\phi - \frac{\partial}{\partial t}(\nabla\cdot\mathbf{A}) &= \rho/\epsilon_0,\end{aligned} \tag{1.2}$$

where $\rho(\mathbf{r},t)$ and $\mathbf{j}(\mathbf{r},t)$ are charge density and current density, respectively, and μ_0 and ϵ_0 are the magnetic permeability and dielectric constant of vacuum. Using the gauge degree of freedom, we can impose additional constraints to decouple the two equations in (1.2).

1. **Lorenz Gauge :** The Lorenz gauge is defined as

$$\nabla\cdot\mathbf{A} + \frac{1}{c}\frac{\partial\phi}{\partial t} = 0, \tag{1.3}$$

which is invariant under Lorentz transformation and yields immediately two independent wave equations for $\phi(\mathbf{r},t)$ and $\mathbf{A}(\mathbf{r},t)$ as,

$$\begin{aligned}\left(\nabla^2 - \frac{1}{c^2}\frac{\partial^2}{\partial t^2}\right)\phi &= -\rho/\epsilon_0,\\ \left(\nabla^2 - \frac{1}{c^2}\frac{\partial^2}{\partial t^2}\right)\mathbf{A} &= -\mu_0\mathbf{j}.\end{aligned} \tag{1.4}$$

In terms of retarded sources, the known solutions for current and charge densities that are dependent on space and time are given by

$$\begin{aligned}\phi(\mathbf{r},t) &= \frac{1}{4\pi\epsilon_0}\int d^3r'\frac{\rho\left(\mathbf{r}', t - |\mathbf{r}-\mathbf{r}'|/c\right)}{|\mathbf{r}-\mathbf{r}'|},\\ \mathbf{A}(\mathbf{r},t) &= \frac{\mu_0}{4\pi}\int d^3r'\frac{\mathbf{j}\left(\mathbf{r}', t - |\mathbf{r}-\mathbf{r}'|/c\right)}{|\mathbf{r}-\mathbf{r}'|}.\end{aligned} \tag{1.5}$$

Except for being Lorentz invariant, the other significant benefit of using this particular gauge is that it includes the correct retardation of sources. This is important for obtaining accurate phase factors when analyzing correlation measurements of electric fields at different space-time points. Inserting equations in (1.5) to electric field equation in (1.1) gives

$$\begin{aligned}\mathbf{E}(\mathbf{r},t) = &-\frac{\mu_0}{4\pi}\int d^3r'\frac{1}{|\mathbf{r}-\mathbf{r}'|}\frac{\partial\mathbf{j}\left(\mathbf{r}', t - |\mathbf{r}-\mathbf{r}'|/c\right)}{\partial t}\\ &+\frac{1}{4\pi\epsilon_0}\int d^3r'\frac{\mathbf{r}-\mathbf{r}'}{|\mathbf{r}-\mathbf{r}'|^3}\rho\left(\mathbf{r}', t - |\mathbf{r}-\mathbf{r}'|/c\right)\\ &+\frac{1}{4\pi\epsilon_0}\int d^3r'\frac{\mathbf{r}-\mathbf{r}'}{|\mathbf{r}-\mathbf{r}'|^2}\frac{\partial\rho\left(\mathbf{r}', t - |\mathbf{r}-\mathbf{r}'|/c\right)}{\partial t}.\end{aligned} \tag{1.6}$$

The second term describes the contribution of time-independent sources, which gives rise to the static Coulomb field. Since it scales as $1/\left|\mathbf{r}-\mathbf{r}'\right|^2$, whereas the other two terms scale as $1/\left|\mathbf{r}-\mathbf{r}'\right|$, it has a negligible effect compared to the other two terms in the far field regime. If the current density is linked through to a (macroscopic) charge density ρ by the following $\mathbf{j}=\rho\mathbf{v}$, we can compare the first and last term. We find that the last term is more considerable than the first one by a factor of $\sim v/c$ where $v=|\mathbf{v}|$ and $\epsilon_0\mu_0=1/c^2$.

We consider the situation of $\rho(\mathbf{r},t)=0$, which describes the absence of any macroscopic charge density. This condition is mainly due to the global charge neutrality of Earth's surface. The standard quantum optics is formulated in this situation as it considers the absence of free charges, thus motivating the quantization in the Coulomb gauge. Under this scenario, photons exhibit two linearly independent polarization directions perpendicular to their propagation direction. They give the correct physical picture far from any charges, where the propagating waves are well approximated by plane waves. Classical electromagnetic waves have two perpendicular polarizations as $\nabla\cdot E=0$, resulting in an asymptotically converging free field solution. Thus, we have only two degrees of freedom from the initial four (three components of $\mathbf{A}$ and ϕ). Any vector field can be decomposed into longitudinal and transverse components. Accordingly, we can write $\mathbf{j}=\mathbf{j}^l+\mathbf{j}^t$, where $\nabla\cdot\mathbf{j}^t=0$, $\nabla\times\mathbf{j}^l=\mathbf{0}$. Using the continuity equation given by $\nabla\cdot\mathbf{j}+\frac{\partial\rho}{\partial t}=0$, for $\rho=0$, we can write $\nabla\cdot\mathbf{j}=0$. The longitudinal current density is a source-free and curl-free quantity spatially constant when $\rho=0$. Additionally, we can simplify further by using the boundary condition of vanishing current for $r\to\infty$ to find that $\mathbf{j}^l=0$. Thus, the transverse polarizations depend only on the locally transverse components of the current density vector. Then we have

$$\mathbf{E}(\mathbf{r},t)=-\frac{\mu_0}{4\pi}\int d^3r'\frac{1}{\left|\mathbf{r}-\mathbf{r}'\right|}\frac{\partial\mathbf{j}^t\left(\mathbf{r}',t-\left|\mathbf{r}-\mathbf{r}'\right|/c\right)}{\partial t}, \tag{1.7}$$

and states that only the transverse component of the current density drives the electromagnetic field. If $\rho=0$ is exact in all space-time, there is no need for assumptions in being the far-field regime in Eq. (1.6). Before proceeding with the classical correlation of the electric field, I will briefly explain that Eq. (1.7) is also obtained in the Coulomb gauge, which is used in the quantum analysis.

2. Coulomb Gauge : The Coulomb gauge sets the divergence of the vector potential to zero $\nabla\cdot\mathbf{A}=0$ in some preferred reference frame. It is pretty helpful for quantizing vector potential in "semiclassical" calculations since the $\mathbf{A}$ is quantized, but the Coulomb interaction is not quantized. Then the Eq. (1.2) follows immediately to $-\nabla^2\phi=\rho/\epsilon_0$ which implies that the scalar potential is given by the

instantaneous, non-retarded charge density. Since we set $\rho(\mathbf{r},t)=0$ for everywhere in space and time, we will have $\phi=0$. Then we immediately recover the wave equation for vector potential given in Eq. (1.5). The same arguments about the absence of the current longitudinal component as a source apply. Then we conclude with the same equation for the electric field in (1.7), which we will now exploit for calculating classical correlations between two different space-time points.

1.2.2 Classical Correlations of Electromagnetic Fields

The visibility (correlation) function of the electric fields related to the current density distributions are given in Refs. [7, 8, 6]. In a reference frame fixed to detectors as we can define it as

$$C_{ij}(\mathbf{r}_1,\mathbf{r}_2,t_1,t_2)\equiv\langle E_i(\mathbf{r}_1,t_1)E_j^*(\mathbf{r}_2,t_2)\rangle, \tag{1.8}$$

where $E_i=\mathbf{E}\cdot\hat{e}_i$ is the electric field component in the direction specified by the unit vector $\hat{e}_i$. With the electric fields measured by two antennae at two different space-time points $(\mathbf{r}_1,t_1)$ and $(\mathbf{r}_2,t_2)$ one can form the product $E_i\left(\mathbf{r}_1,t_1\right)E_j\left(\mathbf{r}_2,t_2\right)$ and can take the average in space and time. We first introduce the Fourier transform (FT) of an arbitrary time-dependent quantity $f(t)$, as $f(t)=\frac{1}{\sqrt{2\pi}}\int_{-\infty}^{\infty}d\omega e^{i\omega t}\tilde{f}(\omega)$ For real $f(t)$ one has $f(-\omega)=f^*(\omega)$. Eq. (1.7) yields

$$\tilde{\mathbf{E}}(\mathbf{r},\omega)=-\frac{\mu_0}{4\pi}\int\frac{d^3r'}{|\mathbf{r}-\mathbf{r}'|}i\omega\tilde{\mathbf{j}}^t\left(\mathbf{r}',\omega\right)e^{-i\omega(|\mathbf{r}-\mathbf{r}'|)/c}. \tag{1.9}$$

The back-transformation reads as $\mathbf{E}(\mathbf{r},t)=\frac{1}{\sqrt{2\pi}}\int_{-\infty}^{\infty}\tilde{\mathbf{E}}(\mathbf{r},\omega)e^{i\omega t}$. This is the full time-dependent field in a space-time point given with infinite precision, including all frequency components from $-\infty$ to ∞, before any filtering. The antenna will not respond much to frequencies beyond its fundamental resonance frequency. Formally this corresponds to introducing an effective filter function $w(\omega)$ in the inverse Fourier transform for $E_i(\mathbf{r},t)$ as

$$E_i(\mathbf{r},t)=\frac{1}{\sqrt{2\pi}}\int_{-\infty}^{\infty}d\omega w(\omega)\tilde{E}_i(\mathbf{r},\omega), \tag{1.10}$$

where the filter function $w(\omega)$ is in general complex. For a narrow bandwidth B and the central frequency ω_0 filter function can be defined as

$$w(\omega)=\begin{cases}1 & \text{for } \omega_0-B/2\leqslant\omega\leqslant\omega_0+B/2\\ 0 & \text{elsewhere}\end{cases}. \tag{1.11}$$

where $B \ll \omega_0$. The antenna will respond differently to different frequencies, with varying phase shifts. A simple dipole antenna is essentially a harmonic oscillator with its characteristic phase shift and attenuation of response beyond the resonance frequency. By inserting Eq. (1.9) into Eq. (1.10), we can find the effectively measured electric field as

$$\mathbf{E}(\mathbf{r},t) = -\frac{\mu_0}{4\pi}\frac{1}{\sqrt{2\pi}}\int_{-\infty}^{\infty} d\omega w(\omega)\int \frac{d^3r'}{|\mathbf{r}-\mathbf{r}'|} i\omega\tilde{\mathbf{j}}^t\left(\mathbf{r}',\omega\right) e^{-i\omega(|\mathbf{r}-\mathbf{r}'|/c-t)}. \tag{1.12}$$

The electric field in Eq. (1.12) is written for a deterministic current density distribution. In reality, these current densities fluctuate. Before we move forward, we describe the properties of these current density distributions. We assume that it is a complex symmetric Gaussian process with current densities uncorrelated in positions, directions, and frequencies [7, 26, 38],

$$\begin{aligned}
&\left\langle \tilde{j}_l\left(\mathbf{r},\omega\right)\tilde{j}_m^*\left(\mathbf{r}',\omega'\right)\right\rangle = \frac{l_c^3}{\tau_c}\delta_{lm}\delta(\omega-\omega')\delta(\mathbf{r}-\mathbf{r}')\left\langle|\tilde{j}_l(\mathbf{r},\omega)|^2\right\rangle,\\
&\left\langle \tilde{j}_l\left(\mathbf{r},\omega\right)\tilde{j}_m\left(\mathbf{r}',\omega'\right)\right\rangle = 0, \quad \left\langle \tilde{j}_l^*\left(\mathbf{r},\omega\right)\tilde{j}_m^*\left(\mathbf{r}',\omega'\right)\right\rangle = 0\,.
\end{aligned} \tag{1.13}$$

The length scale l_c and time scale τ_c are introduced for dimensional grounds, and the polarizations are indexed by l, m, taking values x, y, z. For the classical white noise currents, Eq. (1.13) is a standard model and appears in many places in the literature [40, 27, 11]. Using the correlation of current density distributions and the definition of the filter function, the visibility function of the electric fields at two different space-time points becomes

$$\begin{aligned}
C_{ij}(\mathbf{r}_1,\mathbf{r}_2,t_1,t_2) = \frac{\mu_0^2 l_c^3 B\omega_0^2\delta_{ij}}{32\pi^3\tau_c}\int d^3r\left\langle|\tilde{j}_{t,i}(\mathbf{r},\omega_0)|^2\right\rangle \frac{e^{-i\omega_0(-\Delta t+(|\mathbf{r}_1-\mathbf{r}|-|\mathbf{r}_2-\mathbf{r}|)/c)}}{|\mathbf{r}_1-\mathbf{r}|\,|\mathbf{r}_2-\mathbf{r}|}\\
\times \operatorname{sinc}\left[\frac{B}{2}\left(-\Delta t+\frac{|\mathbf{r}_1-\mathbf{r}|-|\mathbf{r}_2-\mathbf{r}|}{c}\right)\right],
\end{aligned} \tag{1.14}$$

where $\Delta t = t_1 - t_2$ and for spatial correlation its taken as zero $\Delta t = 0$. The integral over Earth's surface is parametrized by $\mathbf{r} = (x, y, R)$ with respect to the coordinate system of the detection plane. Further, we write $|\mathbf{r}_j - \mathbf{r}_1| - |\mathbf{r}_2 - \mathbf{r}| \approx \Delta\mathbf{r}_{12}\cdot\mathbf{r}/|\mathbf{r}|$ for $|\Delta\mathbf{r}_{12}| \ll R$ in the far field regime, where the vector $\Delta\mathbf{r}_{12} = \mathbf{r}_1 - \mathbf{r}_2$ connects two different receiver modes. Then we approximate $|\mathbf{r}_i - \mathbf{r}| \approx R/\cos\tilde{\theta}(x,y)$ with $\tilde{\theta}(x,y)$ the polar angle the angle between the z-axis and the vector (x, y, R). In the microwave regime, one can relate the average amplitude of current density to brightness temperature $T_{\mathrm{B}}(x,y)$ by $\langle|\tilde{j}_{t,l}\left(\mathbf{r},\omega\right)|^2\rangle = K_1 T_{\mathrm{B}}(x,y)\cos\tilde{\theta}(x,y)\delta(z-R)$ with a constant defined as $K_1 = 32\tau_c k_B/(3l_c^3\mu_0 c)$ [7] (See also an appendix of [25]). Further, we define the effective temperature as $T_{\mathrm{eff}}(x,y) \equiv T_{\mathrm{B}}(x,y)\cos^3\tilde{\theta}(x,y)$

and a new constant as $\tilde{K} = k_B \mu_0 B \omega_0^2/(3\pi^3 c)$ and we for a very narrow bandwith B, we can approximate sinc(...) ~ 1. Then visibility function considering these assumptions becomes

$$C_{ij}(\mathbf{r}_1, \mathbf{r}_2) = \frac{\tilde{K}\delta_{ij}}{R^2} \int dxdy\, T_{\text{eff}}(x,y) e^{2\pi i\left(v_x^{12}x + v_y^{12}y\right)}, \tag{1.15}$$

where $v_y^{12} = \Delta x_{12}/(\lambda R)$, $v_x^{12} = \Delta y_{12}/(\lambda R)$ and we used $\omega_0/c = 2\pi/\lambda$. The equation (1.15) is known as the Van Cittert-Zernike theorem, which describes the Fourier transform the relationship between the spatial intensity distribution (or in this case, the temperature distribution) of these incoherent radiation sources and the associated visibility function. Resolution is limited to the paradigmatic resolution limit $d = \lambda R/\Delta x_{12}$ found by Abbe and Rayleigh based on the interference of classical waves, where Δx_{12} is the maximum spatial separation between two antennas. In the following section, I will briefly introduce the quantum definition of the problem.

1.3 Quantum Analysis of Electromagnetic Field

1.3.1 Quantized Electromagnetic Field

The electromagnetic field is quantized by expanding the energy of the free electromagnetic field in modes, and the mode functions form an orthonormal functional basis for the solution of Maxwell equations under appropriate boundary conditions in a finite quantization volume. For the quantized electric field in free space, we consider the quantization volume as infinity, and the discrete modes are replaced by the continuous ones in this limit. We can write the operator for the quantized vector potential $\hat{\mathbf{A}}(\mathbf{r}, t)$ in Coulomb gauge in continuous form as [5, 30]

$$\begin{aligned}\hat{\mathbf{A}}(\mathbf{r},t) = \int d^3k \left(\frac{\hbar}{16\pi^3\varepsilon_0 c|\mathbf{k}|}\right)^{1/2} \\ \times \sum_{\sigma=1,2} \boldsymbol{\varepsilon}(\mathbf{k},\sigma)\hat{a}(\mathbf{k},\sigma)\exp(-ic|\mathbf{k}|t + i\mathbf{k}\cdot\mathbf{r}) + h.c.,\end{aligned} \tag{1.16}$$

where, $\hat{a}(\mathbf{k},\sigma)$ are the continuous mode operators with $\left[\hat{a}\left(\mathbf{k},\sigma\right), \hat{a}^\dagger\left(\mathbf{k},\sigma\right)\right] = \delta(\mathbf{k} - \mathbf{k}')\delta_{\sigma\sigma'}$, and $\boldsymbol{\varepsilon}(\mathbf{k},\sigma)$ are the directions of the polarizations with index $\sigma \in 1, 2$, which are always perpendicular to wave vector $\mathbf{k}$. Mode functions are plane waves and parametrized by $\mathbf{k}$ and σ. As in the classical case, we consider the classical current density distributions as sources of electromagnetic radiation. For this reason, the

interaction Hamiltonian for the classical current distribution of the sources $\mathbf{j}(\mathbf{r},t)$ with electromagnetic waves in free space is given by the following [17, 7, 30, 39]

$$H_I(t) = -\int d^3r\, \mathbf{j}(\mathbf{r},t)\cdot\hat{\mathbf{A}}(\mathbf{r},t). \tag{1.17}$$

In the interaction picture, using the Schrödinger equation, the state of the electromagnetic field at time t can be obtained from the one at t_0 as [39, 17, 30, 29]

$$|\psi(t)\rangle = U\left(t,t_0\right)|\psi\left(t_0\right)\rangle\,, \tag{1.18}$$

where the unitary propagator $U\left(t,t_0\right)$ is given by

$$U\left(t,t_0\right) = \exp\left(\frac{i}{\hbar}\int_{t_0}^{t} dt' \int d^3r\, \mathbf{j}\left(\mathbf{r},t'\right)\cdot\hat{\mathbf{A}}\left(\mathbf{r},t'\right) + i\varphi\left(t,t_0\right)\right). \tag{1.19}$$

The phase $\varphi\left(t,t_0\right)$ is a real number resulting from the classical interaction between currents and equal-time matrix elements. Since our model is semiclassical, the current density changes with the vector potential, and we can write the time evolution as a displacement operator as

$$D(\{\alpha(\mathbf{k},\sigma)\}) = \exp\left[\sum_{\sigma}\int d^3k\,\left[\alpha(\mathbf{k},\sigma)\hat{a}^{\dagger}(\mathbf{k},\sigma) - \alpha^{*}(\mathbf{k},\sigma)\hat{a}(\mathbf{k},\sigma)\right]\right]. \tag{1.20}$$

We assume that for $t_0 \to -\infty$ we have the vacuum state $|\{0\}\rangle$ for all modes. For a deterministic current density, $|\psi(t)\rangle$ is a tensor product of coherent states,

$$|\psi(t)\rangle = |\{\alpha(\mathbf{k},\sigma)\}\rangle = D(\{\alpha(\mathbf{k},\sigma)\})|\{0\}\rangle, \tag{1.21}$$

using Fourier transform of the current densities as in the classical case and taking the integral over t', $\alpha(\mathbf{k},\sigma)$ can be found as

$$\begin{aligned}\alpha(\mathbf{k},\sigma) =& -\left(\frac{1}{32\pi^4\varepsilon_0 c\hbar|\mathbf{k}|}\right)^{1/2}\\ &\times\int d^3r\int_{-\infty}^{\infty} d\tilde{\omega}\tilde{\mathbf{j}}\left(\mathbf{r},\tilde{\omega}\right)\cdot\boldsymbol{\varepsilon}(\mathbf{k},\sigma)\exp(-i\mathbf{k}\cdot\mathbf{r})\\ &\times\frac{\exp(i(\tilde{\omega}+c|\mathbf{k}|)t)}{i\epsilon - c|\mathbf{k}| - \tilde{\omega}}.\end{aligned} \tag{1.22}$$

where a shift in the denominator '$i\epsilon$' is introduced, and it is necessary for the integral to converge at $t = -\infty$. So far, we have the modes of free space. To understand the electric field received by the interferometer, we need an input-output process between the modes of the free space and the interferometer modes. In the

following section, I will define the scattering process to the received modes of the interferometer.

1.3.2 Mode Matching: Scattering to Interferometer Modes

An interferometer receives the electromagnetic field through an array of antennas at positions $\mathbf{r}_i$ in a detection plane parallel to the source plane and separated from it by a distance R. Each antenna's output mode is connected to input modes that receive electromagnetic field radiation. Receiver "i" consist of antenna "i" combined with its output waveguide. After filtering, the output of each antenna is considered to be single-mode with discrete annihilation operator $\hat{b}_i$. The modes received by the antennas can be called "spatial field modes." Since each mode, $\hat{b}_i$ is specific to a location on the detection plane. Single modes with discrete annihilation operator $\hat{a}_i$ are reflected from the pre-processing stage. On the antenna side, we describe incoming plane waves in the interferometer by $\hat{a}(\mathbf{k}, \sigma)$ and scattered outgoing plane waves by $\hat{b}(\mathbf{k}, \sigma)$. One can use the scattering matrix formalism to see the connection between incoming and outgoing modes.

Moreover, the $\hat{b}_i$ modes are separated by considerably large distances comparable to the central wavelength of λ. And, the collection area of each antenna A_D is assumed to be $A_D \sim \lambda^2$. These constraints make the modes for different receivers orthogonal and simplify the form of the scattering matrix. A scattering matrix connects incoming and outgoing modes, and one can write it as [47, 48]

$$\mathcal{S} = \begin{bmatrix} \mathcal{S}^{(\text{scat})} & \mathcal{S}^{(\text{trans})} \\ \mathcal{S}^{(\text{rec})} & \mathcal{S}^{(\text{refl})} \end{bmatrix}. \tag{1.23}$$

Here the scattering matrix acts on the vector $[\{\hat{a}(\mathbf{k}, \sigma)\}_{\{\mathbf{k},\sigma\}}, \{\hat{a}_i\}_{\{i\}}]^T$, where $\{a(\mathbf{k}, \sigma)\}_{\{\mathbf{k},\sigma\}}$ is the vector of continuous plane wave operators with continuous $\mathbf{k}$ and two polarizations. $\{\hat{a}_i\}_{\{i\}}$ is the vector of modes with $i \in \{1, .., n\}$ for an n-mode interferometer. The first block, $\mathcal{S}^{(\text{scat})}$, describes the scattering of incoming plane waves to outgoing plane waves from the interferometer. The off-diagonal block $\mathcal{S}^{(\text{rec})}$ describes the coupling of the incoming plane waves $\hat{a}(\mathbf{k}, \sigma)$ into the receiver modes $\hat{b}_i$, and $\mathcal{S}^{(\text{trans})}$ describes scattering of reflected receiver modes $\hat{a}_i$ into outgoing plane waves $\hat{b}(\mathbf{k}, \sigma)$. The matrix $\mathcal{S}^{(\text{refl})}$ represents the scattering (reflection) between the receivers and will be neglected by assuming there is no reflection from these modes, $\mathcal{S}^{(\text{refl})} \sim 0$. One can also verify that if the receivers have only incoming and outgoing modes, the receiving and transmitting pattern of the receivers will be the same $\mathcal{S}^{(\text{trans})}(\mathbf{k}, \sigma; j) = \mathcal{S}^{(\text{rec})}(j; \mathbf{k}, \sigma)$ and we can denote them as simply $\mathcal{S}_j(\mathbf{k}, \sigma)$. We can replace the field operators $\hat{a}(\mathbf{k}, \sigma)$ in Eq. (1.21)

by the following relation for n different receiver modes

$$\hat{a}(\mathbf{k},\sigma) = \sum_{j}^{n} \mathcal{S}_j^*(\mathbf{k},\sigma)\hat{b}_j + \sum_{\sigma'} \int d^3\mathbf{k}' \mathcal{S}^{*(\text{scat})}(\mathbf{k}',\sigma',\mathbf{k},\sigma)\hat{b}(\mathbf{k}',\sigma'). \tag{1.24}$$

Then using Eq. (1.24), we can write the coherent state in Eq. (1.21) as

$$|\psi(t)\rangle = D(\{\beta_i\})D(\{\beta(\mathbf{k},\sigma)\})\,|\{0\}\rangle\,, \tag{1.25}$$

where $D(\{\beta(\mathbf{k},\sigma)\})$ can be defined similarly to Eq. (1.20) and $\beta(\mathbf{k},\sigma)$ is the eigenvalue of the scattered plane waves modes with annihilation operator $\hat{b}(\mathbf{k},\sigma)$. The interferometer does not have any access to outgoing plane modes $\hat{b}(\mathbf{k},\sigma)$ as well, and $\hat{b}_i$ commutes with $\hat{b}(\mathbf{k},\sigma)$. Thus, we can safely trace them out. The displacement operator for the spatial modes of the interferometer can be written in the form

$$D(\{\beta_i\}) = \bigotimes_{i}^{n} \exp\left[\beta_i \hat{b}_i^\dagger - \beta_i^* \hat{b}_i\right]. \tag{1.26}$$

In the end, we have a coherent state for spatial modes of the interferometer, and for the field amplitudes β_i, we can write in the simplified form as

$$\beta_i = -\left(\frac{3c\mu_0}{16\pi\hbar\omega_0^3 B}\right)^{1/2} \int_{-\infty}^{\infty} d\omega w(-\omega)\omega \int d^3r \tilde{\mathbf{j}}_t(\mathbf{r},\omega)\cdot\hat{u}\frac{e^{-i\omega(\bar{t}-|\mathbf{r}-\mathbf{r}_i|/c)}}{|\mathbf{r}-\mathbf{r}_i|}. \tag{1.27}$$

Since the mean value of the current density distribution is zero, we only need the covariance matrix elements of the received modes to describe Gaussian states, which I will introduce in the following section. Thus, we must calculate $\langle b_i^\dagger b_j\rangle$. The integral over ω can be taken using the filter function of bandwidth B as discussed in the classical correlation of the electromagnetic fields. Integrals can be further simplified using current density correlations (See first publication for the details). Then we find

$$\begin{aligned}\langle b_i^\dagger b_j\rangle = K\int d^3r\, \frac{\langle|\tilde{j}_{t,l}(\mathbf{r},\omega)|^2\rangle\, e^{i\omega_0(|\mathbf{r}-\mathbf{r}_j|-|\mathbf{r}-\mathbf{r}_i|)/c}}{|\mathbf{r}-\mathbf{r}_i||\mathbf{r}-\mathbf{r}_j|} \\ \times \operatorname{sinc}\left[\frac{B}{2c}(|\mathbf{r}-\mathbf{r}_j|-|\mathbf{r}-\mathbf{r}_i|)\right],\end{aligned} \tag{1.28}$$

where, $K = 3c\mu_0 l_c^3/(16\pi\hbar\omega_0\tau_c)$ and $\operatorname{sinc}[x] \equiv \sin x/x$. As in the classical case, average current density amplitudes can be related to the temperature distribution of the surface. Then we can simplify the $\langle b_i^\dagger b_j\rangle$ further using far-field approximation as we discussed in our first paper [25].

1.3.3 Gaussian States

Let us consider n received modes of the interferometer in the detection plane with annihilation operators $\hat{b}_i$ satisfying the commutation relations $\left[\hat{b}_i, \hat{b}_j^\dagger\right] = \delta_{ij}$, all other commutators being zero. If we arrange all operators into a vector form such as $\mathbf{b} = \left[b_1, b_1^\dagger, b_2, b_2^\dagger, \ldots b_n, b_n^\dagger\right]$. The Gaussian state is defined as a state with Gaussian characteristic function which can be completely described by the mean displacement γ^α and covariance matrix $\Sigma^{\alpha\beta}$ as [9, 1, 16, 32, 35, 44]

$$\begin{aligned} \gamma^\alpha &= \mathrm{Tr}\left[\rho \mathbf{b}^\alpha\right] \\ \Sigma^{\alpha\beta} &= \frac{1}{2}\mathrm{Tr}\left[\rho\left(\tilde{\mathbf{b}}^\alpha \tilde{\mathbf{b}}^\beta + \tilde{\mathbf{b}}^\beta \tilde{\mathbf{b}}^\alpha\right)\right], \end{aligned} \tag{1.29}$$

in terms of the centered operator $\tilde{\mathbf{b}}^\alpha = \mathbf{b}^\alpha - \gamma^\alpha$. We use this notation while using the quantum Cramér bound in our first and second publications. However, for simplicity, while we are using classical Cramér Rao bound from the measurement, we use Sudarshan-Glauber representation. We show that the state of the incoming modes of the n-mode interferometer from these radiated sources can be modeled as circularly symmetric Gaussian states with a partial coherence, which encodes the information of position and amplitudes distribution of the sources. Then after the scattering process [47, 48] from the interferometer, the partially coherent state received in the n modes is represented by

$$\rho = \int \mathrm{d}^{2n}\beta \Phi(\{\beta_i\}) |\{\beta_i\}\rangle\langle\{\beta_i\}|, \tag{1.30}$$

where $|\{\beta_i\}\rangle$ is a multi-mode coherent state for spatial antenna modes, $\{\beta_i\} = \beta_1, \beta_2, \ldots \beta_n$, and

$$\Phi(\{\beta_i\}) = \frac{1}{\pi^n \det \Gamma} e^{-\bar{\beta}^\dagger \Gamma^{-1} \bar{\beta}}. \tag{1.31}$$

with $\bar{\beta}^T = (\beta_1, \beta_2 \ldots \beta_n)$ is the Sudarshan-Glauber representation, and $\mathrm{d}^{2n}\beta \equiv \mathrm{d}\Re\beta_1 \mathrm{d}\Im\beta_1 \ldots \mathrm{d}\Re\beta_n \mathrm{d}\Im\beta_n$. The matrix Γ is the coherence matrix for n antenna modes, and its elements are defined as $\Gamma_{ij} = \langle \hat{b}_i^\dagger \hat{b}_j \rangle$.

1.4 Parameter Estimation Theory

One of the most fundamental purposes of physics is the estimation of physical quantities from experimental data obtained from measurements. By using the tools of the estimation theory, the goal is to achieve fundamental precision of any given parameter or a set of parameters [20, 22, 19]. The theory of probability is used to properly formalize parameter estimation theory by considering the random processes.

In this section, I will first introduce the random variables, parameter space, and estimators. Then, I will define the classical Cramér-Rao bound and associated classical Fisher information matrix for multiparameter estimation. Further, I will discuss the parameter estimation in the quantum limit. Quantum metrology attempts to make high-resolution and high-precision measurements using Quantum Theory. It gives the most fundamental bound known as the quantum Cramér Rao Bound related to the quantum Fisher information matrix. One can check Ref. [13] for more details about the parameter estimation theory.

1.4.1 Random variables - Parameter Space - Estimators

From a mathematical point of view, a random variable X is a formalization of a quantity that depends on random events. When the value is observed, we call it *realization* or *observation* of X. We represent the probability that X accepts the value x_i as $p(x_i)$ or $p(X = x_i)$, then the random variable X is distributed according to this probability density function $p(x_i)$. If possible process outcomes are countable, we call it *discreate* random variable. Otherwise, we call it *continuous* random variable and the normalization conditions for the probabilities given by

$$\sum_i p(x_i) = 1, \quad \int dx p(x) = 1 \tag{1.32}$$

respectively. Suppose we have a random variable X and $\{p_\theta\}$ family of probability distributions depends on parameter $\theta \in \Theta$, where Θ is called *parameter space*. X is distributed according to a probability density function p_θ and θ is not a random variable. Thus, it is essential to assume that the parameter θ is deterministic for unbiased parameter estimation and θ has a fixed value. The parameter space Θ is a subset of $\mathbf{R}$ if we have a single parameter (scalar parameter). It is a subset of $\mathbf{R}^n$ if we have many parameters (a vector of parameters). The results of the measurement are realized as a statistical sample $\boldsymbol{x} = (x_1, \ldots, x_n)$ from a probability density function $p_\theta(\boldsymbol{x})$, which also depends on the parameter θ that we want to estimate. We represent the averages for the probability distribution as $\mathbb{E}_\theta$. Further, we call *estimator* for the method by which we intend to estimate the parameter from the collected data. It is defined as a function of the data in the form $\hat{\theta} \equiv \hat{\theta}(\boldsymbol{x})$. We consider an estimator as good estimator if the expected value of it gives the actual value of the parameter, such as

$$\mathbb{E}_\theta[\hat{\theta}(\boldsymbol{x})] \equiv \int_{\mathbb{R}^n} \hat{\theta}(\boldsymbol{x}) p_\theta(\boldsymbol{x}) \mathrm{d}^n \boldsymbol{x} = \theta. \tag{1.33}$$

If this condition is satisfied, the estimator can be considered an unbiased estimator and guarantees that it is not affected by at least some systematic errors. A better criterion for determining the quality of an estimator is to minimize the mean square error (MSE), which is defined as

$$\mathrm{MSE}[\hat{\theta}] = \mathbb{E}_\theta\left[(\hat{\theta}-\theta)^2\right] \equiv \int_{\mathbb{R}^n} (\hat{\theta}(\boldsymbol{x})-\theta)^2 p_\theta(\boldsymbol{x})\mathrm{d}^n\boldsymbol{x}, \tag{1.34}$$

which calculates the mean squared error of the estimator from the actual value. When we expand it, we get two different terms as

$$\begin{aligned}\mathrm{MSE}[\hat{\theta}] &= \mathbb{E}_\theta\left[\left(\hat{\theta}-\mathbb{E}_\theta[\hat{\theta}]+\mathbb{E}_\theta[\hat{\theta}]-\theta\right)^2\right] \\ &= \mathbb{E}_\theta\left[\left(\hat{\theta}-\mathbb{E}_\theta[\hat{\theta}]\right)^2\right] + \left(\mathbb{E}_\theta[\hat{\theta}]-\theta\right)^2 \\ &= \mathrm{Var}_\theta[\hat{\theta}] + b(\theta)^2,\end{aligned} \tag{1.35}$$

where we define the bias of the estimator as $b(\theta) = \mathbb{E}_\theta[\hat{\theta}] - \theta$ and the variance of the estimator can be defined as

$$\mathrm{Var}_\theta[\hat{\theta}] = \int_{\mathbb{R}^n} \hat{\theta}(\boldsymbol{x})^2 p_\theta(\boldsymbol{x})\mathrm{d}^n\boldsymbol{x} - \left(\int_{\mathbb{R}^n} \hat{\theta}(\boldsymbol{x}) p_\theta(\boldsymbol{x})\mathrm{d}^n\boldsymbol{x}\right)^2. \tag{1.36}$$

If $b(\theta) = 0$, the estimator is unbiased, and the estimator's variance is equivalent to the mean squared error. In this case, the error or uncertainty in the estimation of the parameter θ is $\delta\theta$ becomes

$$\sqrt{\mathrm{Var}_\theta[\hat{\theta}]} = \delta\theta. \tag{1.37}$$

Theoretically, we want to find the best estimator that minimizes $\delta\theta$. However, as some explicit examples show, an unbiased estimator that minimizes the variance for all θ might not even exist [20]. Therefore, finding the minimum variance unbiased estimator can be complicated in practice. At this point, finding a lower bound on the variance of an unbiased estimator is quite important. Several examples of estimators are given in the literature, such as a constant, moment, maximum likelihood estimator (MLE), etc. Among them, we will consider MLE, which also plays an important role in interpreting the Cramér-Rao theorem.

Maximum likelihood estimator : The likelihood function l of a random variable X is defined as

$$l(\theta; x) := p_\theta(x), \tag{1.38}$$

where the likelihood is equal to the probability distribution, the new notation is utilized due to the meaning of θ and X. In estimation theory, X describes the experiment and is a random quantity whose realizations vary from experiment to experiment, but θ is a fixed parameter. Once we write $p_\theta(X = x)$, we consider the probability. Then the notation $l(\theta; x)$ stresses the dependency on θ. Since we already observed x and considered it fixed, we like to understand how likely it was that the parameter had the value θ. The probability corresponds to a statement before the experiment, while the likelihood corresponds to a statement once the experiment was realized and we observed the value x. Since the logarithm is a monotonously increasing function, the log of the likelihood function is maximized by the same parameter. For this reason, it is also useful to define the loglikelihood L as

$$L(\theta; x) := \ln(l(\theta; x)), \tag{1.39}$$

which is the logarithm of the likelihood function. Generally, we are using an n-sample $\{X^{(n)}\}$ in the estimation procedure with a specific realization of it $\{x_i\}$. In this case, the maximum likelihood estimator becomes

$$\hat{\theta}_{\text{mle}} = \text{argmax}_{\theta \in \Theta} L\left(\theta; \{x_i\}\right). \tag{1.40}$$

where the joint probability distribution of the n-sample can be obtain for the likelihood as $l\left(\theta, \{x_i\}\right) = \prod_i l\left(\theta; x_i\right)$. Since the logarithm transforms the product into a sum will give us the loglikelihood function as

$$L\left(\theta, \{x_i\}\right) = \sum_i \ln\left(p_\theta\left(X_i = x_i\right)\right). \tag{1.41}$$

The MLE has an invariance property, which means that if one has the MLE $\hat{\theta}_{\text{mle}}$ for a parameter θ, then the MLE for a parameter $f = f(\theta)$, where f is a bijective function, is given by

$$\hat{f}_{\text{mle}} = f\left(\hat{\theta}_{\text{mle}}\right). \tag{1.42}$$

1.4.2 Classical Cramér Rao Bound and Fisher Information

In the previous section, we showed that the MSE equals the variance for unbiased estimators. The best estimator leads to a vanishing bias; we are looking for the estimator that minimizes the variance (MVU estimator). The difficulty is that MVU estimators do not always exist. Because it generally does not minimize variance for different values of the same parameter. Then, a different approach would be to look for an estimator that reduces the variance locally. The problem is that

the calculation of this variance is a difficult task. Instead, we will derive a lower bound for the variance and then study how tight it is. A famous lower bound for the variance is given by the famous Cramér-Rao theorem, named after Harald Cramér and Calyampudi Radhakrishna Rao, which provides a lower bound for the covariance for any unbiased estimator [14, 12, 37].

Theorem 1.1 - Cramér-Rao Bound. *Let regularity condition holds for a probability distribution* $\{p_\theta(X)\}$ *with a random variable* X *and a parameter* $\theta \in \Theta$ *as*

$$\mathbb{E}_\theta \left[\frac{\partial \ln \left(p_\theta(x) \right)}{\partial \theta} \right] = 0, \quad \forall \theta. \tag{1.43}$$

Then the variance $\mathrm{Var}\left[\hat{\theta}_{\mathrm{est}}\right]$ *of any locally unbiased estimator satisfy*

$$\mathrm{Var}\left[\hat{\theta}_{\mathrm{est}}\right] \geq \frac{1}{F\left(p_\theta; \theta\right)}, \tag{1.44}$$

where $F\left(p_\theta; \theta\right)$ *is called Fisher information associated with the probability density function* $p_\theta(x)$ *and defined as*

$$F\left(p_\theta; \theta\right) := \mathbb{E}_\theta \left[\left(\frac{\partial \ln \left(p_\theta(x) \right)}{\partial \theta} \right)^2 \right]. \tag{1.45}$$

If an estimator saturates the Cramér-Rao bound, it is called an efficient estimator.

Proof of the Cramér-Rao theorem : The proof of Cramér Rao's theorem is based on the Cauchy-Schwarz inequality. Here, I will start with the proof of a parameter function $f(\theta)$ instead of the parameter θ directly. Then the estimator can be written as $\hat{f}_{\mathrm{est}}$. Since $\theta \in \Theta$ then we need that $\hat{f}_{\mathrm{est}}$ takes its values in $f(\Theta)$. We can start with the regularity condition, which holds in the theorem. The left-hand side of the regularity condition becomes

$$\mathbb{E}_\theta \left[\frac{\partial \ln \left(p_\theta(x) \right)}{\partial \theta} \right] = \int \mathrm{d}x \frac{\partial p_\theta(x)}{\partial \theta}. \tag{1.46}$$

Changing the integral with the derivative will give

$$\mathbb{E}_\theta \left[\frac{\partial \ln \left(p_\theta(x) \right)}{\partial \theta} \right] = \frac{\partial}{\partial \theta} \int \mathrm{d}x p_\theta(x). \tag{1.47}$$

By the definition of the normalization, we have $\int \mathrm{d}x p_\theta(x) = 1$. Then the derivative of 1 gives directly zero, and we end up with regularity condition as

$$\mathbb{E}_\theta \left[\frac{\partial \ln \left(p_\theta(x) \right)}{\partial \theta} \right] = 0. \tag{1.48}$$

Thus, changing the derivative and the limits is sufficient for the regularity condition to be satisfied. We can say that this is true for most joint probability distributions. However, one exception we can immediately say is when the parameter appears in the limit of the integral such as estimating the upper bound of a uniform distribution. Now let us continue the unbiasedness of the estimator by taking the derivative concerning θ for both sides of the unbiasedness condition $\int \mathrm{d}x p_\theta(x)\hat{f}_{\text{est}}(x) = f(\theta)$. Since only the average value of the estimator depends on the θ from the probability distribution p_θ, not the estimator itself, then interchanging the integral and derivative, we will have

$$\frac{\partial f(\theta)}{\partial \theta} = \frac{\partial}{\partial \theta}\int \mathrm{d}x p_\theta(x)\hat{f}_{\text{est}} = \int \mathrm{d}x p_\theta(x)\frac{\partial \ln\left(p_\theta(x)\right)}{\partial \theta}\hat{f}_{\text{est}}. \tag{1.49}$$

We can think of it this way: the process used to estimate the value of θ should not depend on θ. If we multiply both sides of the regularity condition by $f(\theta)$, and using the fact that $f(\theta)$ is independent of x, we get

$$\int \mathrm{d}x p_\theta(x)\frac{\partial \ln\left(p_\theta(x)\right)}{\partial \theta}f(\theta) = 0. \tag{1.50}$$

Then we can obtain the following equation by subtracting Eq. (1.50) from Eq. (1.49) as

$$\frac{\partial f(\theta)}{\partial \theta} = \int \mathrm{d}x p_\theta(x)\frac{\partial \ln\left(p_\theta(x)\right)}{\partial \theta}\left(\hat{f}_{\text{est}} - f(\theta)\right). \tag{1.51}$$

To apply the Cauchy-Schwarz inequality, let us first introduce a scalar product for any joint probability distribution $p_\theta(x)$ and for two real functions $a(x)$ and $b(x)$ as

$$\langle a(x), b(x)\rangle_{p_\theta} := \int \mathrm{d}x a(x)b(x)p_\theta(x). \tag{1.52}$$

Then the Eq. (1.51) in this notation becomes

$$\frac{\partial f(\theta)}{\partial \theta} = \left\langle \frac{\partial \ln\left(p_\theta(x)\right)}{\partial \theta}, \hat{f}_{\text{est}} - f(\theta)\right\rangle_{p_\theta}. \tag{1.53}$$

Using the Cauchy-Schwarz inequality, we will have the following for the right-hand side of Eq. (1.53) as

$$\left\langle \frac{\partial \ln\left(p_\theta(x)\right)}{\partial \theta}, \hat{f}_{\text{est}} - f(\theta)\right\rangle^2_{p_\theta} \leq \left\langle \frac{\partial \ln\left(p_\theta(x)\right)}{\partial \theta}, \frac{\partial \ln\left(p_\theta(x)\right)}{\partial \theta}\right\rangle_{p_\theta} \left\langle \hat{f}_{\text{est}} - f(\theta), \hat{f}_{\text{est}} - f(\theta)\right\rangle_{p_\theta}. \tag{1.54}$$

Then we can rewrite the inequality in the following form

$$\int \mathrm{d}x p_\theta(x) \left(\hat{f}_{\text{est}} - f(\theta)\right)^2 \geq \frac{\left(\frac{\partial f(\theta)}{\partial \theta}\right)^2}{\int \mathrm{d}x p_\theta(x) \left(\frac{\partial \ln(p_\theta(x))}{\partial \theta}\right)^2}. \tag{1.55}$$

By taking $f(\theta) = \theta$, using the definition the varience $\int \mathrm{d}x p_\theta(x) \left(\hat{f}_{\text{est}} - f(\theta)\right)^2 = \text{Var}\left[\hat{g}_{\text{est}}\right]$ and defining the Fisher information as

$$F\left(p_\theta; \theta\right) = \left\langle \frac{\partial \ln\left(p_\theta(x)\right)}{\partial \theta}, \frac{\partial \ln\left(p_\theta(x)\right)}{\partial \theta} \right\rangle_{p_\theta}. \tag{1.56}$$

We prove the Cramér-Rao theorem as

$$\text{Var}\left[\hat{\theta}_{\text{est}}\right] \geq \frac{1}{F\left(p_\theta; \theta\right)}. \tag{1.57}$$

The loglikelihood derivative, sometimes called the score function, becomes sensitive to slight variations of θ as the probability changes, that is, in the case of the higher derivative score function. Therefore, the Fisher information matrix (FI), which is the norm of the score, takes a significant value and lowers the variance.

Multiparameter Estimation : In multiparameter estimation, the goal is to estimate a vector of parameters, $\boldsymbol{\theta} \equiv \{\theta_1, \theta_2 ... \theta_m\}$. The constraints and formalism requirements for multiparameter estimation are the same as for scalar parameter estimation. However, the Cramér-Rao bound corresponds to an inequality for the covariance matrix.

$$\text{Cov}\left(\hat{\boldsymbol{\theta}}_{\text{est}}\right) - \mathcal{F}\left(\boldsymbol{\theta}\right)^{-1} \geq 0. \tag{1.58}$$

The elements of the Fisher information matrix $\boldsymbol{\mathcal{F}}\left(\boldsymbol{\theta}\right)$ is given by

$$\mathcal{F}_{ij}\left(\boldsymbol{\theta}\right) := \mathbb{E}_\theta \left[\frac{\partial \ln\left(p_{\boldsymbol{\theta}}\right)}{\partial \theta_i} \frac{\partial \ln\left(p_{\boldsymbol{\theta}}\right)}{\partial \theta_j}\right]. \tag{1.59}$$

Reparametrization : If reparametrization is needed, i.e., if we need to estimate a vector of parameters $\boldsymbol{f(\theta)}$, which is a function of original parameters $\boldsymbol{\theta}$ then the inverse of the new Fisher information matrix for the parameter change is given by

$$\mathcal{F}\left(\boldsymbol{f}\right)^{-1} = \mathbf{J}\left[\boldsymbol{f}, \{\theta_i\}\right] \cdot \mathcal{F}\left(\boldsymbol{\theta}\right)^{-1} \cdot \mathbf{J}\left[\boldsymbol{f}, \{\theta_i\}\right]^t, \tag{1.60}$$

where $\mathbf{J}\left[\boldsymbol{f}, \{\theta_i\}\right]$ is the Jacobian of the transformation with elements $J_{ij}\left[\boldsymbol{f}, \{\theta_i\}\right] := \partial f_i(\boldsymbol{\theta})/\partial \theta_j$. If an estimator $\hat{\theta}_{\text{est}}$ is efficient to estimate the original parameter θ, then $f(\hat{\theta}_{\text{est}})$ it does not mean that will be efficient to estimate the new parameters

of $f(\theta)$. We can interpret the Fisher information matrix $\mathcal{F}(\boldsymbol{f})$ as a metric in the manifold from a geometric perspective [3]. This metric can be calculated from the joint probability distribution as in Eq. (1.59). For the coordinate changes $\{\theta_i\}$ at any point on the manifold, the Fisher information matrix may not be invertible, or there may be fewer variables in the new coordinate system; that is why we used the transformation for the inverse of the Fisher information matrix. When the Fisher information matrix is diagonal, the estimation of the θ_i parameter will not be affected by the lack of information on the other parameters. In this case, the multiparameter estimation is determined to be the same as the multiple scalar single parameter estimation. For the following section, we will refer to the Fisher information matrix from the classical estimation theory as the classical Fisher information matrix (CFIM) to distinguish it from the quantum Fisher information matrix (QFIM).

1.4.3 Quantum Cramér Rao Bound and Quantum Fisher Information

In this section, I will introduce the quantum Cramér-Rao bound with the quantum Fisher information matrix $\mathscr{F}(\boldsymbol{\theta})$ for multiparameter estimation. We aim to derive the upper bound for the CFIM we get from the measurement. In quantum mechanics, we mostly have the positive operator value measure (POVM), i.e., a set of operators $\{\Pi_k\}$ satisfying

$$\Pi_k \geqslant 0 \quad \forall k, \quad \sum_k \Pi_k = \mathbb{I}, \tag{1.61}$$

in the discrete case. Then the probability distribution of the measurement is given by the Born rule as

$$p_k(\boldsymbol{\theta}) = \mathrm{Tr}\left(\rho_{\boldsymbol{\theta}} \Pi_k\right), \tag{1.62}$$

where $\rho_{\boldsymbol{\theta}}$ is the density matrix of the quantum state encoding the parameter vector $\boldsymbol{\theta}$, on which the measurement is performed. As we see, we can choose any set POVMs to perform a measurement. However, our metrological goal is to find the ultimate bound on precision achievable for the parameter vector φ. Thus, we need to find the correct set of POVM elements that saturates this ultimate bound. Before moving forward, we can start with the quantum version of the Cramér Rao theorem for multiparameter estimation.

Theorem 1.2 - Quantum Cramér Rao Theorem : *Let us consider the family of quantum states $\rho_{\boldsymbol{\theta}}$ depending on a vector of parameter $\{\theta_i\} \in \Theta$. The*

covariance matrix $\mathrm{Cov}(\hat{\boldsymbol{\theta}}_{\mathrm{est}})$ *of any locally unbiased estimator* $\hat{\boldsymbol{\theta}}_{\mathrm{est}}$ *is lower bounded by the inverse of the quantum Fisher information matrix*

$$\mathrm{Cov}(\hat{\boldsymbol{\theta}}_{\mathrm{est}}) \geq \mathscr{F}(\boldsymbol{\theta})^{-1}, \tag{1.63}$$

and the elements of the quantum Fisher information matrix are defined as

$$\mathscr{F}_{ij}(\boldsymbol{\theta}) = \frac{1}{2}\,\mathrm{Tr}(\rho_{\boldsymbol{\theta}}\{\mathscr{L}_{\mathrm{i}}, \mathscr{L}_{\mathrm{j}}\}), \tag{1.64}$$

where $\{\cdot,\cdot\}$ *is the anti-commutator, and* $\mathscr{L}_i$ *is the symmetric logarithmic derivative (SLD) related to parameter* i*, which is defined as* $\frac{1}{2}\left(\mathscr{L}_i\rho_{\boldsymbol{\theta}} + \rho_{\boldsymbol{\theta}}\mathscr{L}_i\right) := \partial_i\rho_{\boldsymbol{\theta}}$*.*

Proof of the Quantum Cramér Rao theorem : We can start writing the CFIM elements F_{ij}^k from a measurement corresponds to a regular POVM element given by Π_k as [45]

$$F_{ij}^k = \frac{\partial_i \,\mathrm{Tr}\left(\rho_{\boldsymbol{\theta}}\Pi_k\right)\partial_j \,\mathrm{Tr}\left(\rho_{\boldsymbol{\theta}}\Pi_k\right)}{\mathrm{Tr}\left(\rho_{\boldsymbol{\theta}}\Pi_k\right)}, \tag{1.65}$$

where CFIM elements can be written for complete POVM using additivity of the Fisher information matrix $\mathcal{F}_{ij} = \sum_k F_{ij}^k$. Using the cyclic property of trace, such as

$$\mathrm{Tr}\left(\mathscr{L}_i\rho_{\boldsymbol{\theta}}\Pi_k\right) = \mathrm{Tr}\left(\rho_{\boldsymbol{\theta}}\Pi_k\mathscr{L}_i\right) = \left[\mathrm{Tr}\left(\rho_{\boldsymbol{\theta}}\mathscr{L}_i\Pi_k\right)\right]^*, \tag{1.66}$$

and the definition of the SLD, we can expand one of the terms in the nominator as

$$\begin{aligned}\partial_i \,\mathrm{Tr}\left(\rho_{\boldsymbol{\theta}}\Pi_k\right) = \mathrm{Tr}\left(\partial_i\rho_{\boldsymbol{\theta}}\Pi_k\right) &= \frac{1}{2}\left[\mathrm{Tr}\left(\mathscr{L}_i\rho_{\boldsymbol{\theta}}\Pi_k\right) + \mathrm{Tr}\left(\rho_{\boldsymbol{\theta}}\mathscr{L}_i\Pi_k\right)\right] \\ &= \mathrm{Re}\left[\mathrm{Tr}\left(\rho_{\boldsymbol{\theta}}\Pi_k\mathscr{L}_i\right)\right].\end{aligned} \tag{1.67}$$

For a real and nonzero vector $\boldsymbol{u}$, an upper bound can be found by using the following inequalities:

$$\begin{aligned}\sum_{ij} u_i F_{ij}^k u_j =& \frac{\left[\mathrm{Re}\,\mathrm{Tr}\left(\rho_{\boldsymbol{\theta}}\Pi_k\sum_i u_i\mathscr{L}_i\right)\right]^2}{\mathrm{Tr}\left(\rho_{\boldsymbol{\theta}}\Pi_k\right)} \\ \leqslant& \frac{\left|\mathrm{Tr}\left(\rho_{\boldsymbol{\theta}}\Pi_k\sum_i u_i\mathscr{L}_i\right)\right|^2}{\mathrm{Tr}\left(\rho_{\boldsymbol{\theta}}\Pi_k\right)} && \rightarrow \text{First inequality} \\ \leqslant& \sum_{ij} u_i u_j \,\mathrm{Tr}\left(\rho_{\boldsymbol{\theta}}\mathscr{L}_i\Pi_k\mathscr{L}_j\right) && \rightarrow \text{Second inequality} \\ =& \frac{1}{2}\sum_{ij} u_i u_j \left[\mathrm{Tr}\left(\rho_{\boldsymbol{\theta}}\mathscr{L}_i\Pi_k\mathscr{L}_j\right) + \mathrm{Tr}\left(\rho_{\boldsymbol{\theta}}\mathscr{L}_j\Pi_k\mathscr{L}_i\right)\right] \\ =& \sum_{ij} u_i u_j \,\mathrm{Re}\left[\mathrm{Tr}\left(\rho_{\boldsymbol{\theta}}\mathscr{L}_i\Pi_k\mathscr{L}_j\right)\right],\end{aligned} \tag{1.68}$$

where in the last step we used the fact $u_i u_j$ is symmetric in indices i, j. First inequlity can be saturated if $\mathrm{Tr}\left(\rho_{\boldsymbol{\theta}} \Pi_k \sum_i u_i \mathscr{L}_i\right)$ is real for any parameter $\{\theta_i\}$. For the second inequality, we used the Cauchy Swartz inequality defined as $\left|\mathrm{Tr}\left(A^\dagger B\right)\right|^2 \leqslant \mathrm{Tr}\left(A^\dagger A\right) \mathrm{Tr}\left(B^\dagger B\right)$, with $A \equiv \sqrt{\Pi_k}\sqrt{\rho_{\boldsymbol{\theta}}}$ and $B \equiv \sum_i \sqrt{\Pi_k} u_i \mathscr{L}_i \sqrt{\rho_{\boldsymbol{\theta}}}$. The saturation of the second inequality requires that $\sqrt{\Pi_k}\sqrt{\rho_{\boldsymbol{\theta}}}$ must be proportional to $\sqrt{\Pi_k}\sum_i u_i \mathscr{L}_i \sqrt{\rho_{\boldsymbol{\theta}}}$ for any arbitrary, nonzero, and real vector $\boldsymbol{u}$. Summing over k both sides of the inequality, we will have the inequality in the form

$$\sum_{ij} u_i \mathcal{F}_{ij}^k u_j \leq \frac{1}{2} \sum_{ij} u_i u_j \,\mathrm{Tr}\left(\rho_{\boldsymbol{\theta}} \{\mathscr{L}_i, \mathscr{L}_j\}\right) = \sum_{ij} u_i \mathscr{F}_{ij} u_j, \tag{1.69}$$

where in the last term, $\mathscr{F}_{ij}$ is defined as the QFIM as in the theorem, which is independent of any parameter-independent measurement and the ultimate bound for the CFIM. Since the covariance matrix $\mathrm{Cov}(\hat{\boldsymbol{\theta}}_{\mathrm{est}})$ of an estimator is lower bounded by the CFIM then we conclude with the proof of the quantum Cramér Rao theorem for regular POVMs as

$$\mathrm{Cov}(\hat{\boldsymbol{\theta}}_{\mathrm{est}}) \geq \mathcal{F}(\boldsymbol{\theta})^{-1} \geq \mathscr{F}(\boldsymbol{\theta})^{-1}. \tag{1.70}$$

Now I will give a summary of the properties of quantum Fisher information :

Theorem 1.3 - Monocity of the quantum Fisher information : *Let $\mathcal{H}$ be a Hilbert space of a family of density matrices $\{\rho_\theta\}$ with $\rho_\theta \in \mathcal{S}(\mathcal{H})$. The quantum channel $\mathcal{E}$ is independent of the parameter θ acting on $\mathcal{S}(\mathcal{H})$ as well, then we have*

$$\mathscr{F}\left(\mathcal{E}\left(\rho_\theta\right); \theta\right) \leq \mathscr{F}\left(\rho_\theta; \theta\right). \tag{1.71}$$

For the parameter independent unitary quantum channels $\mathcal{U}$ quantum Fisher information is conserved under evolution as

$$\mathscr{F}\left(\mathcal{U}\left(\rho_\theta\right); \theta\right) = \mathscr{F}\left(U \rho_\theta U^\dagger; \theta\right) = \mathscr{F}\left(\rho_\theta; \theta\right). \tag{1.72}$$

The monotonicity of the quantum Fisher information is discussed in Ref. [34] and more recently, its proof given by the book on geometry of quantum states in Ref [4].

Theorem 1.4 - Additivity of the quantum Fisher information : *If $\mathcal{H}_1$ and $\mathcal{H}_2$ are the two Hilbert spaces $\mathcal{S}$ of two families of density matrices $\{\rho_{1,\theta}\}$ and $\{\rho_{2,\theta}\}$, respectively ($\rho_{1,\theta} \in \mathcal{S}\left(\mathcal{H}_1\right)$ and $\rho_{2,\theta} \in \mathcal{S}\left(\mathcal{H}_2\right)$). Then we have*

$$\mathscr{F}\left(\rho_{1,\theta} \otimes \rho_{2,\theta}; \theta\right) = \mathscr{F}\left(\rho_{1,\theta}; \theta\right) + \mathscr{F}\left(\rho_{2,\theta}; \theta\right). \tag{1.73}$$

Ref. [24] gives complete proof for the additivity property of the quantum Fisher

information. Moreover, this property also holds for the classical Fisher information. Using this theorem for a quantum state ρ_θ of N copies $\rho_\theta^{\otimes N}$, the quantum Fisher information scales as $\mathscr{F}_N \propto N\mathscr{F}$, where $\mathscr{F}_N$ is the total quantum Fisher information.

Theorem 1.5 - Convexity of the quantum Fisher information : *Let two families of quantum states* $\{\rho_\theta\}$ *and* $\{\sigma_\theta\}$ *parametrized by* θ*, where* ρ_θ*,* σ_θ *are elements of* $\mathcal{S}(\mathcal{H})$*. For* $0 \leq \lambda \leq 1$ *we have*

$$\mathscr{F}\left(\lambda\rho_\theta + (1-\lambda)\sigma_\theta; \theta\right) \leq \lambda\mathscr{F}\left(\rho_\theta; \theta\right) + (1-\lambda)\mathscr{F}\left(\sigma_\theta; \theta\right). \tag{1.74}$$

The proof of convexity of the quantum Fisher information can be found in [15].

In the next chapter, I will briefly discuss our results for the single and multiparameter metrology considering imaging problems of the array interferometers.

Chapter 2

Results

2.1 Single parameter estimation for the Gaussian states

The SLD and the elements of the QFI matrix are given in Ref. [16] for any Gaussian state. The SLD can be written as

$$\mathscr{L}_i = \frac{1}{2}\mathfrak{M}^{-1}_{\alpha\beta,\gamma\delta}\left(\partial_i \Sigma^{\gamma\delta}\right)\left(\mathbf{b}^{\alpha}\mathbf{b}^{\beta} - \Sigma^{\alpha\beta}\right), \tag{2.1}$$

where $\mathfrak{M}^{-1}_{\alpha\beta,\gamma\delta}$ is the fourth order tensor form of the inverse of the matrix $\mathfrak{M} \equiv \Sigma \otimes \Sigma + \frac{1}{4}\Omega \otimes \Omega$, with $\Omega = \bigoplus_{k=1}^{n} i\sigma_y$, and the summation convention is used for the repeating indices. In our case, the mean displacement of the Gaussian state is zero. Then the elements of the QFI matrix in [16] become

$$\mathscr{F}_{ij} = \frac{1}{2}\mathfrak{M}^{-1}_{\alpha\beta,\gamma\delta}\partial_j \Sigma^{\alpha\beta}\partial_i \Sigma^{\gamma\delta}, \tag{2.2}$$

Using the properties of the Gaussian state (circularly symmetric and with zero means), we can write the SLD for n mode interferometers as [25]

$$\mathscr{L}_i = \sum_{j}^{n} g_i^j \hat{b}_j^\dagger \hat{b}_j + \sum_{j<k}^{n} (g_i^{jk}\hat{b}_j^\dagger \hat{b}_k + (g_i^{jk})^* \hat{b}_k^\dagger \hat{b}_j) + \mathrm{C}, \tag{2.3}$$

where C is a constant term that can be dropped for diagonalization purposes. In the single parameter case, the optimal POVM is the set of projectors onto eigenstates of $\mathscr{L}_i$. It allows one to saturate the QCRB in the limit of infinitely many measurements using maximum likelihood estimation [20, 10, 33]. To find the POVMs from the SLD, we construct a Hermitian matrix $\mathbf{M}_i$ whose diagonal elements are real-valued functions which are defined as $g_i^j \equiv \mathfrak{M}^{-1}_{\alpha\beta,\gamma\delta}\left(\partial_i \Sigma^{\gamma\delta}\right)$ with

$\alpha = 2j$ and $\beta = 2j-1$. The off-diagonal elements are complex-valued functions and defined as $g_i^{jk} = \mathfrak{M}^{-1}_{\alpha\beta,\gamma\delta}\left(\partial_i \Sigma^{\gamma\delta}\right)$ with $\alpha = 2j$ and $\beta = 2k-1$ and $k > j$. By introducing a new set for the field operators such that, $\bar{\mathbf{b}}^\dagger \equiv \left[\hat{b}_1^\dagger, \hat{b}_2^\dagger, ..., \hat{b}_n^\dagger\right]$ and $\bar{\mathbf{b}} \equiv \left[\hat{b}_1, \hat{b}_2, ..., \hat{b}_n\right]^T$, we write the SLD in the following form

$$\mathscr{L}_i = \bar{\mathbf{b}}^\dagger \mathbf{M}_i \bar{\mathbf{b}}. \tag{2.4}$$

As $\mathbf{M}_i$ is a Hermitian matrix it can be unitarily diagonalized by $\mathbf{M}_i = \mathbf{V}_i^\dagger \mathbf{D}_i \mathbf{V}_i$ with $\mathbf{V}_i^\dagger \mathbf{V}_i = \mathbb{I}$. A new set of operators can be defined as $\bar{\mathbf{d}}_i^\dagger = \bar{\mathbf{b}}^\dagger \mathbf{V}_i^\dagger$ where $\bar{\mathbf{d}}_i^\dagger = \left[\hat{d}_{i1}^\dagger, \hat{d}_{i2}^\dagger, ..., \hat{d}_{in}^\dagger\right]$. The optimal POVM for the single parameter case ($i = 1$, which we drop in the following) can be found as a set of projectors in the Fock basis $\{|m_1, m_2, ..., m_n\rangle \langle m_1, m_2, ..., m_n|\}_{\{m_1, m_2 ... m_n\}}$ of the $\hat{d}_l$ with $\hat{d}_l^\dagger \hat{d}_l |m_1, m_2, ..., m_n\rangle = m_l |m_1, m_2, ..., m_n\rangle$, where $l \in \{1, ..., n\}$. The $\hat{d}_l$ will be called "detection modes."

In our first paper, using the tools of quantum metrology introduced in the previous chapter, we investigated the single parameter estimation of the sources' different parameters using different interferometer modes. In the following, I will briefly summarize our results for estimating the parameters: source temperature, source size, source separation, and centroid of two-point sources.

The resolution of the Uniform Circular Source : For the simple example of $T(x, y)$, we consider a circular source on the source plane parametrized with radius "a," temperature "T," and the central location as "(x_0, y_0)". Since the source size directly affects the mean photon number, we first look at the estimation of "a" with a single-mode antenna. We calculated the quantum Fisher information, which can be saturated by photon number resolving measurement for a single mode. We compared this with the Heterodyne measurement (its POVM can be taken as a projector in a coherent state basis, as discussed in the appendix of the first paper). In the limit $a \to 0$, we observe that quantum Fisher information tends to a constant, while classical Fisher information for Heterodyne detection vanishes (See Fig. 2a of first paper). We obtain similar results for two-mode (Fig. 3a) and more than two-mode interferometers (Fig. 6). When we increase the number of modes, we see that additional information arises due to the correlation of different modes and increases the quantum Fisher information. Here, we also checked the dependency on the maximum baseline of the interferometer, as we see from Figs. (3b) (3c), for different temperatures and different source sizes, quantum Fisher information has a maximum at some point; later, it oscillates around a constant value. The other parameter we are interested in is the source's temperature. We notice that photon number resolving is superior to the Heterodyne detection for estimating T. For large sources, they converge at some point due to the increasing number of photons

in a single mode. More than single-mode interferometers, if we know the centroid of the source, the modes can be connected by the unitary from SLD to saturate the quantum bound for these single parameters with a photon number resolving detection.

Spatial Resolution of Two Point Sources : Resolution of the two-point sources is a very popular problem in the literature; as discussed in the introduction section, using the SPADE technique, one can resolve the two-point sources for a lens system such as optical telescopes, microscopes, etc. Here, We are considering this problem for the interferometers. We consider a two-point source parametrized with source separation "s," centroid "t" and the source temperatures "T_1" and "T_2." We aim to estimate "s" and "t" separately. Since these parameters are written in the two-mode phase difference, we at least need to consider two-mode interferometers. First, we showed that the quantum Fisher information increases for estimating "s" and "t" when we increase the temperatures (See Fig. (4a) and (4d) respectively). Then, we checked the quantum Fisher information for the unbalanced temperature configurations and obtained that we can resolve "s" and "t" better than the balanced case (Fig (4b) and (4e)). Further, we consider Heterodyne detection to compare our results for resolving "s" and "t." For estimating the source separation, we obtained that quantum Fisher information becomes constant when the separation vanishes. In addition, classical Fisher information for Heterodyne detection vanishes. To achieve the quantum limit, we need to combine the incoming modes of the interferometer with a beam splitter and a phase shifter with a correct phase delay requires the knowledge of the centroid only. Then by non-local measurement of these modes using photon number resolving detection, we can break Rayleigh's curse of resolution for two-point sources. Thus we can resolve them for any separation. On the other hand, with Heterodyne detection, which can be understood as local measurement, we always have the resolution limit. Later, we increase the number of modes to understand how the quantum Fisher information scales. If we keep the nearest separation of the modes fixed on the detection plane, we see that quantum Fisher information increases sub-exponentially (See Fig. (5b) (5e)). If we keep the total baseline fixed, quantum Fisher information increases linearly by the number of modes (Fig. (5c) (5f)).

In the end, we conclude that with the correct pre-processing of the received modes of the interferometer, we can achieve super-resolution for the selected parameters by saturating the quantum limit.

2.2 Multiparameter Estimation for Gaussian States

Contrary to the single parameter case, the multiparameter QCRB can generally not be saturated. By introducing a weight matrix $\boldsymbol{w}$, one can define the scalar inequalities from the matrix-valued QCRB as $\mathrm{Tr}(\boldsymbol{w}\,\mathrm{Cov}(\tilde{\boldsymbol{\theta}})) \geqslant \mathrm{Tr}(\boldsymbol{w}\mathscr{F}(\boldsymbol{\theta})^{-1}) \equiv C^S(\boldsymbol{\theta}, \boldsymbol{w})$. The weight matrix is a positive definite matrix to satisfy the scalar Cramér-Rao bound. For simplicity, we will consider $\boldsymbol{w} = \mathbb{I}$ to optimize the average variances of all parameters. One can also consider a diagonal matrix with different weights. This will result in directly decreasing the variances of preferred estimators. Further, choosing a weight matrix with off-diagonal elements includes covariances of the estimators. Holevo realized the problem of saturability of QCRB and proposed a tighter and more fundamental bound [23] $C^H(\boldsymbol{\theta}, \boldsymbol{w})$, which is upper bounded by $2C^S(\boldsymbol{\theta}, \boldsymbol{w})$ [41, 2]. If the SLD operators for different parameters commute on average $\mathrm{Tr}(\rho_{\boldsymbol{\theta}}[L_i, L_j]) = 0$, then the Holevo-CRB is equivalent to the QCRB. Moreover, the QCRB for multiparameter estimation can be saturated asymptotically with a collective measurement in the limit of an infinitely large number of copies $\rho_{\boldsymbol{\theta}}^{\otimes N}$ [36, 2].

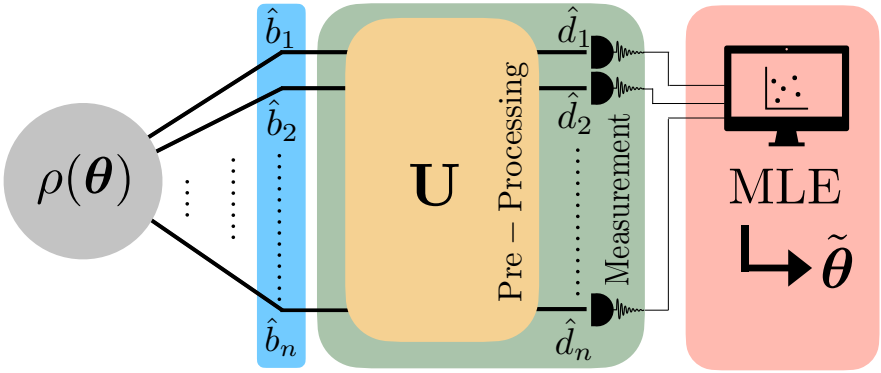

Figure 2.1: The Gaussian state $\rho(\boldsymbol{\theta})$ of the n-mode interferometer contains the spatial and the radiometric information from current density sources. The incoming modes $\hat{b}_i$ are combined with an optimized $\mathbf{U}$ to have detection modes $\hat{d}_i$ of the photon counting measurement. For experimental realization, one can decompose $\mathbf{U}$ into $SU(2)$ group elements similar to optical quantum computing, i.e., using beam splitters and phase shifters. After the measurements, one estimates the parameter set using an estimator function such as a maximum likelihood estimator (MLE).

Most Informative Bound for Multiparameter Metrology : The most informative bound minimizes the classical scalar Cramer Rao bound over all the possible POVMs. In the single parameter case, from the diagonalization of the SLD, we see that one needs to combine the incoming modes with a unitary transformation to saturate the QCRB single parameter case. This transformation, even for a single

parameter, depends on the parameter itself. In the multiparameter case, any of these specific unitary transformations for a specific parameter usually gives a more significant mean square error for the remaining parameters. Using the clue from the SLD structure, we drop the index "i" from the unitary transformation of the modes and minimize the scalar bound of the classical Fisher information matrix for multiparameter estimation over all possible unitaries. Then, a new set of operators for the detection modes can be defined as $\bar{\mathbf{d}} = \mathbf{U}\bar{\mathbf{b}}$ where $\bar{\mathbf{d}}^T = \left[\hat{d}_1, \hat{d}_2, ..., \hat{d}_n\right]$, where $\mathbf{U}$ is the corresponding unitary transformation of the field modes (See 2.1). The average values of the elements of the new coherence matrix $\tilde{\Gamma}$ can be found by using $\hat{d}_i = \sum_l U_{il}\hat{b}_l$ as

$$\tilde{\Gamma}_{ij} = \langle d_i^\dagger d_j \rangle = \sum_{kl} U_{ik}^* U_{jl} \langle b_k^\dagger b_l \rangle. \tag{2.5}$$

Then we will have the probabilities after measurement $P(m_1, ..m_n|\theta_1, \theta_2, ..., \theta_l)$ as

$$\begin{aligned} P(\{m_k\}|\boldsymbol{\theta}) &= \int \mathrm{d}^{2n}\delta\tilde{\Phi}(\{\delta_i\})|\langle\{m_k\}|\{\delta_i\}\rangle|^2, \\ &= \int \mathrm{d}^{2n}\delta\tilde{\Phi}(\{\delta_i\}) \prod_i e^{-|\delta_i|^2} \frac{|\delta_i|^{2m_i}}{m_i!}. \end{aligned} \tag{2.6}$$

where $|\{\delta_i\}\rangle$ is a coherent state of the detection modes and $\tilde{\Phi}(\{\delta_i\})$ is the Sudarshan-Glauber function for the state of the detection modes. Due to the linear transformation from $\bar{\mathbf{b}}$ to $\bar{\mathbf{d}}$, it is still a Gaussian. The most informative bound [2] in this case is the bound minimized over all possible unitary matrices

$$\mathrm{Tr}\left[\boldsymbol{w}\,\mathrm{Cov}(\tilde{\boldsymbol{\theta}})\right] \geq \min_{\mathbf{U}} \left[\mathrm{Tr}\left[\boldsymbol{w}\mathcal{F}^{-1}(\boldsymbol{\theta})\right]\right]. \tag{2.7}$$

Estimating the source temperatures of many pixels on the source plane : In our first paper, we only consider the single parameter estimation. However, our ultimate aim is to estimate $T(x, y)$ completely. Our second paper only focused on multiparameter estimation and multiparameter quantum Cramer Rao bound. We consider having many pixels on the source plane, each parametrized by T_i. The goal is to estimate the parameter vector $\boldsymbol{\theta} = (T_1, T_2, ...T_p)$, where p is the total pixel number. Here, we checked the compatibility condition for our set of parameters. Numerically, we find that for n mode interferometer, SLDs of different parameters commute on average for the quantum state of the interferometer. Thus, Holevo-CRB is equivalent to QCRB. Further, we assume that we know the position of each pixel precisely on the source plane; all pixels are next to each other, and their sizes are ten times smaller than the resolution limit of the classical detection strategies. As a starting point, we consider two-pixel and two-mode interferometers. We analyze the corresponding unitary for the non-local measurement considering

only the phase delay. When we vary the phase in the unitary to combine these two modes, we can saturate the scalar quantum Cramer Rao bound for the correct phase (See Fig. (2) in the second paper). For the next step, we increase the number of pixels and the number of modes so as not to leave any redundant parameters. The parameterization of the unitary when $n > 2$ is a difficult task. Therefore, we used an optimization algorithm to minimize the cost function from the most informative bound. By considering the photon loss, which is parametrized by μ, we analyzed the 1D pixel sources (See Fig. (3) and Fig. (4)). In the last step, we

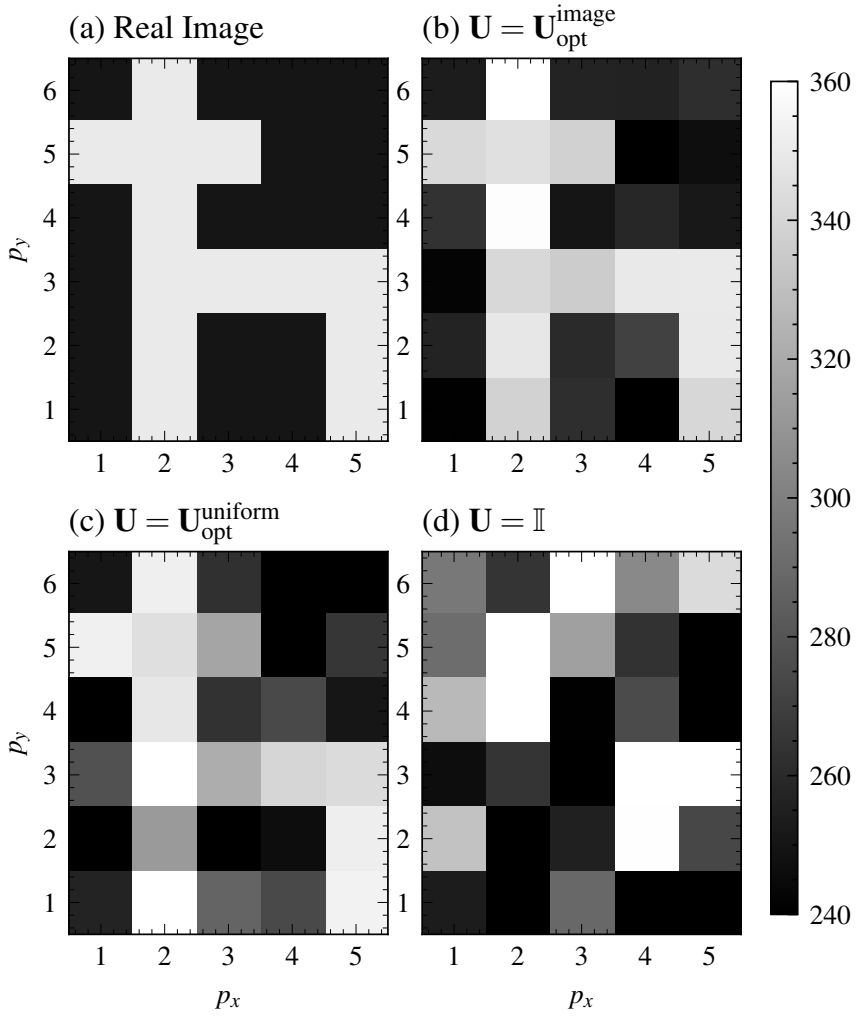

Figure 2.2: (a) The image on the source plane with 30 pixels will be estimated using a maximum likelihood estimator. (b) The reconstructed image after single photon detection in detection modes $\hat{d}_i$ obtained from using the optimized unitary $\mathbf{U}_{\text{opt}}^{\text{image}}$ specific to the temperature distribution. (c) The reconstructed image using a unitary optimized for uniform temperature distribution $\mathbf{U}_{\text{opt}}^{\text{uniform}}$. (d) The reconstructed image using a local measurement of single photons considering $\mathbf{U} = \mathbb{I}$. Pixel size $a = 3.0$ km, average temperature $\bar{T} \sim 293$ K, and sample size $N = 10^8$.

go beyond the 1D model by considering source pixels on a 2D surface. We obtain super-resolution for an optimized unitary $\mathbf{U}_{\text{opt}}^{\text{image}}$ specific to the actual image in Fig. (2.2a), as seen from the reconstructed image using MLE in Fig. (2.2b). However, revealing this optimized unitary requires knowledge of the image. That is why we found another unitary optimized for the uniform temperature distribution $\mathbf{U}_{\text{opt}}^{\text{uniform}}$ and used it to estimate the actual image. After reconstructing the image using MLE, we obtain again a sharp image that is sufficient to demonstrate the actual image (See Fig. (2.2c)). If we check the local measurement by considering $\mathbf{U} = \mathbb{I}$ (means direct detection), we see from Fig. (2.2d) that the reconstructed image is entirely washed out. Thus, we can not resolve it by direct detection due to the resolution limit of the local measurement of the modes.

Chapter 3

Conclusion and Outlook

In our first paper, we obtain the general partially coherent state received by an antenna array starting from a microscopic current density distribution in the source plane corresponding to a position-dependent brightness temperature $T_{\text{eff}}(x, y)$. We calculated the QFI and the QCRB for the minimum uncertainty for the parameters that can be estimated based on measurements of the multi-mode quantum state of the interferometer. We demonstrated how the optimal measurements allow one to estimate a single parameter estimation. We showed that the optimal measurements correspond to photon detection in specific detector modes obtained from the original receiver modes by mode mixing via beam splitters and phase shifters. From the dependence of that partially coherent quantum states on parameters that characterize the sources, we estimated the radius a and the brightness temperature T of a uniform circular source. Then, we estimated the source's centroid t and source separation s for two-point sources for single-mode and two-mode interferometers. We demonstrated a clear quantum advantage over the classical strategy corresponding to direct heterodyne measurements of the receiver modes. We benchmarked our results with the performance of the SMOS mission, which achieves about 35 km resolution with 69 antennas deployed on three four-meter long arms arranged in a Y-shape, operating at 21 cm wavelength and flying at the height of 758 km above Earth. For example, we showed that using the optimal measurements, a single arm of length 4 m with 20 antennas and a single measurement would allow a spatial resolution of about 1.5 km. I.e. with a satellite, a more than 20 times increase in resolution compared to SMOS could be achieved. By increasing the size of the array to 19 m, the 20 antennas should give rise to a spatial resolution down to 300 m. Assuming that the number of samples is given by the time the satellite flies over the object whose size one wants to estimate divided by the inverse bandwidth, even with a single receiver with a spatial resolution down

to a few meters. In principle, a radiometric resolution of a fraction of a Kelvin becomes possible.

In our second paper, we focused on the temperatures on the ground as parameters for passive remote sensing as a quantum multi-parameter estimation problem rather than geometrical information of sources currently, such as the separation, centroid, or phases of sources. An array interferometer with many antennas receives thermal electromagnetic radiation from the pixels in the source plane. Then the received interferometer modes are mixed according to an optimized unitary transformation, and in the corresponding optimized detection modes, the single-photon detectors detect the incoming photons. We optimized the cost function from a scalar classical Cramér-Rao bound obtained by the inverse Fisher information matrix for estimating the temperatures from the photon-counting results with a positive weight matrix leading to a "most-informative bound". For a uniform weight over all pixels, we show that one can approximatively saturate the scalar quantum Cramér-Rao bound based on the quantum Fisher information matrix for the same positive weight matrix. The optimized unitary depends on the actual temperature distribution in principle. However, we showed that the unitary obtained from a uniform temperature distribution gives still much better resolution than direct photon counting in the incoming modes. We showed that the found optimal mode of mixing, followed by single photon detection, leads to a spatial resolution of the reconstructed images that are at least about an order of magnitude better than Rayleigh's limit (about 3 km instead of 35 km for an antenna array comparable with the one of SMOS, even for substantial photon losses), given in the present case by the van Cittert-Zernike theorem. We used a conjugate gradient algorithm for the optimization over the unitaries. The optimal unitary can be decomposed into $SU(2)$ group elements using beam splitters and phase shifters and can be realized as linear optical quantum computing.

Experimentally, single-photon detection in the microwave regime is still difficult but has started to become available [28], and even number-resolved photon detection in the microwave regime has meanwhile been shown [43]. Considering the recent availability of single-photon detection in the micro-wave domain, our results show a path towards substantially enhanced resolution in passive remote sensing compared to classical interferometers that effectively implement heterodyne measurements. Further advancements might be possible for larger photon numbers or smaller losses if photon-number resolved measurements are available. Several challenges remain. Post-measurement beam synthesis standard in interferometric astronomy does not work here, as the detection modes already depend on the pixel in the image that one wants to focus on. However, the substantial quantum advantages explained

here theoretically in a relatively simple but real-world scenario give hope that quantum metrology can help to significantly improve the resolution of passive Earth observation schemes, with a corresponding positive effect on the data available for feeding climate models, weather forecasts, and forecasts of floodings.

Further discussions apart from this thesis might include the generalization of the quantum Cramér-Rao bound to sources illuminated with non-classical light sources. Here, the initial quantum state might also be optimized before imprinting the parameters of the scattered surface. Apart from this, one might also consider a non-local measurement using entangled photons to correlate information in the received modes of the interferometer and might give better resolution compared to local Heterodyne detection.

Bibliography

[1] Gerardo Adesso, Sammy Ragy, and Antony R. Lee. "Continuous Variable Quantum Information: Gaussian States and Beyond". In: *Open Systems & Information Dynamics* 21.01n02 (2014), p. 1440001. DOI: 10.1142/S1230161214400010.

[2] F. Albarelli et al. "A Perspective on Multiparameter Quantum Metrology: From Theoretical Tools to Applications in Quantum Imaging". In: *Physics Letters A* 384.12 (2020), p. 126311. DOI: 10.1016/j.physleta.2020.126311. URL: https://linkinghub.elsevier.com/retrieve/pii/S0375960120301109.

[3] Shun'ichi Amari et al. *Methods of Information Geometry*. Trans. by Daishi Harada. Nachdruck. Translations of Mathematical Monographs 191. Providence, Rhode Island: American Mathematical Society, 2007. ISBN: 978-0-8218-4302-4 978-0-8218-0531-2.

[4] Ingemar Bengtsson and Karol Zyczkowski. *Geometry of Quantum States: An Introduction to Quantum Entanglement*. First. Cambridge University Press, 2006. ISBN: 978-0-521-81451-5 978-0-521-89140-0 978-0-511-53504-8. DOI: 10.1017/CBO9780511535048. URL: https://www.cambridge.org/core/product/identifier/9780511535048/type/book.

[5] K. J. Blow et al. "Continuum Fields in Quantum Optics". In: *Phys. Rev. A* 42.7 (1990), pp. 4102–4114. DOI: 10.1103/PhysRevA.42.4102. URL: https://link.aps.org/doi/10.1103/PhysRevA.42.4102.

[6] Daniel Braun. "Physical Analysis of Spatial and Temporal Correlations For SMOS-NEXT". [Unpublished].

[7] Daniel Braun et al. "Fourier-Correlation Imaging". In: *J. Appl. Phys.* 123.7 (2018), p. 074502. DOI: 10.1063/1.5017680. URL: http://aip.scitation.org/doi/10.1063/1.5017680.

[8] Daniel Braun et al. “Generalization of the Van Cittert–Zernike Theorem: Observers Moving with Respect to Sources”. In: *Meas. Sci. Technol.* 27.1 (2016), p. 015002. DOI: 10.1088/0957-0233/27/1/015002. URL: https://iopscience.iop.org/article/10.1088/0957-0233/27/1/015002.

[9] Daniel Braun et al. “Precision Measurements with Photon-Subtracted or Photon-Added Gaussian States”. In: *Phys. Rev. A* 90.1 (2014), p. 013821. DOI: 10.1103/PhysRevA.90.013821. URL: https://link.aps.org/doi/10.1103/PhysRevA.90.013821.

[10] Samuel L. Braunstein and Carlton M. Caves. “Statistical Distance and the Geometry of Quantum States”. In: *Physical Review Letters* 72.22 (1994), pp. 3439–3443. DOI: 10.1103/PhysRevLett.72.3439. URL: https://link.aps.org/doi/10.1103/PhysRevLett.72.3439.

[11] Rémi Carminati and Jean-Jacques Greffet. “Near-Field Effects in Spatial Coherence of Thermal Sources”. In: *Physical Review Letters* 82.8 (1999), pp. 1660–1663. DOI: 10.1103/PhysRevLett.82.1660. URL: https://link.aps.org/doi/10.1103/PhysRevLett.82.1660.

[12] Harald Cramér. *Mathematical Methods of Statistics*. 19. print., 1. paperb. print. Princeton Landmarks in Mathematics and Physics. Princeton: Princeton Univ. Press, 1999. ISBN: 978-0-691-08004-8 978-0-691-00547-8.

[13] Julien Mathieu Elias Fraisse. “New Concepts in Quantum-Metrology: From Coherent Averaging to Hamiltonian Extensions”. PhD thesis. Universität Tübingen, 2018. DOI: 10.15496/PUBLIKATION-22271. URL: https://publikationen.uni-tuebingen.de/xmlui/handle/10900/80877.

[14] Maurice Frechet. “Sur l’extension de certaines evaluations statistiques au cas de petits echantillons”. In: *Revue de l’Institut International de Statistique / Review of the International Statistical Institute* 11.3/4 (1943), pp. 182–205. (Visited on 04/04/2023).

[15] Akio Fujiwara. “Quantum channel identification problem”. In: *Phys. Rev. A* 63 (4 Mar. 2001), p. 042304. DOI: 10.1103/PhysRevA.63.042304. URL: https://link.aps.org/doi/10.1103/PhysRevA.63.042304.

[16] Yang Gao and Hwang Lee. “Bounds on Quantum Multiple-Parameter Estimation with Gaussian State”. In: *Eur. Phys. J. D* 68.11 (2014), p. 347. DOI: 10.1140/epjd/e2014-50560-1. URL: http://link.springer.com/10.1140/epjd/e2014-50560-1.

[17] Roy J. Glauber. "Coherent and Incoherent States of the Radiation Field". In: *Phys. Rev.* 131.6 (1963), pp. 2766–2788. DOI: 10.1103/PhysRev.131.2766. URL: https://link.aps.org/doi/10.1103/PhysRev.131.2766.

[18] Stefan W. Hell and Jan Wichmann. "Breaking the Diffraction Resolution Limit by Stimulated Emission: Stimulated-Emission-Depletion Fluorescence Microscopy". In: *Opt. Lett.* 19.11 (1994), p. 780. DOI: 10.1364/OL.19.000780.

[19] Carl W. Helstrom. "Cramer-Rao Inequalities for Operator-Valued Measures in Quantum Mechanics". In: *Int. J. Theor. Phys.* 8.5 (1973), pp. 361–376. DOI: 10.1007/BF00687093. URL: http://link.springer.com/10.1007/BF00687093.

[20] Carl W. Helstrom. "Detection Theory and Quantum Mechanics". In: *Inform Comput* 10.3 (1967), pp. 254–291. DOI: 10.1016/S0019-9958(67)90302-6. URL: https://linkinghub.elsevier.com/retrieve/pii/S0019995867903026.

[21] Carl W. Helstrom. "Estimation of Object Parameters by a Quantum-Limited Optical System". In: *J. Opt. Soc. Am.* 60.2 (1970), p. 233. DOI: 10.1364/JOSA.60.000233. URL: https://www.osapublishing.org/abstract.cfm?URI=josa-60-2-233.

[22] Carl W. Helstrom. "Quantum Detection and Estimation Theory". In: *J. Stat. Phys.* 1.2 (1969), pp. 231–252. DOI: 10.1007/BF01007479. URL: http://link.springer.com/10.1007/BF01007479.

[23] A.S Holevo. "Statistical Decision Theory for Quantum Systems". In: *J Multivariate Anal* 3.4 (1973), pp. 337–394. DOI: 10.1016/0047-259X(73)90028-6.

[24] Zhengfeng Ji et al. "Parameter Estimation of Quantum Channels". In: *IEEE Transactions on Information Theory* 54.11 (2008), pp. 5172–5185. DOI: 10.1109/TIT.2008.929940. URL: http://ieeexplore.ieee.org/document/4655455/.

[25] Emre Köse, Gerardo Adesso, and Daniel Braun. "Quantum-enhanced passive remote sensing". In: *Phys. Rev. A* 106 (1 July 2022), p. 012601. DOI: 10.1103/PhysRevA.106.012601. URL: https://link.aps.org/doi/10.1103/PhysRevA.106.012601.

[26] R Kubo. "The Fluctuation-Dissipation Theorem". In: *Rep. Prog. Phys.* 29.1 (1966), pp. 255–284. DOI: 10.1088/0034-4885/29/1/306.

[27] L. D. Landau et al. *Statistical physics*. Pergamon international library of science, technology, engineering, and social studies v. 5, 9. Oxford ; New York: Pergamon Press, 1980.

[28] Raphaël Lescanne et al. "Irreversible Qubit-Photon Coupling for the Detection of Itinerant Microwave Photons". In: *Phys. Rev. X* 10 (2 May 2020), p. 021038. DOI: 10.1103/PhysRevX.10.021038. URL: https://link.aps.org/doi/10.1103/PhysRevX.10.021038.

[29] Rodney Loudon and Thomas von Foerster. "The Quantum Theory of Light". In: *Am. J. Phys.* 42.11 (1974), pp. 1041–1042. DOI: 10.1119/1.1987930. URL: http://aapt.scitation.org/doi/10.1119/1.1987930.

[30] Leonard Mandel, Emil Wolf, and Pierre Meystre. "Optical Coherence and Quantum Optics". In: *Am. J. Phys.* (1996). ISSN: 0002-9505. DOI: 10.1119/1.18450.

[31] K Matsumoto. "A New Approach to the Cramér-Rao-type Bound of the Pure-State Model". In: *Journal of Physics A: Mathematical and General* 35.13 (2002), pp. 3111–3123. DOI: 10.1088/0305-4470/35/13/307.

[32] S. Olivares. "Quantum Optics in the Phase Space: A Tutorial on Gaussian States". In: *Eur. Phys. J. Special Topics* 203.1 (2012), pp. 3–24. DOI: 10.1140/epjst/e2012-01532-4. URL: http://link.springer.com/10.1140/epjst/e2012-01532-4.

[33] Matteo G. A. Paris. "Quantum Estimation for Quantum Technology". In: *International Journal of Quantum Information* 07.supp01 (2009), pp. 125–137. DOI: 10.1142/S0219749909004839. URL: https://www.worldscientific.com/doi/abs/10.1142/S0219749909004839.

[34] Dénes Petz. "Monotone Metrics on Matrix Spaces". In: *Linear Algebra and its Applications* 244 (1996), pp. 81–96. DOI: 10.1016/0024-3795(94)00211-8. URL: https://linkinghub.elsevier.com/retrieve/pii/0024379594002118.

[35] Olivier Pinel et al. "Ultimate Sensitivity of Precision Measurements with Intense Gaussian Quantum Light: A Multimodal Approach". In: *Phys. Rev. A* 85.1 (2012), p. 010101. DOI: 10.1103/PhysRevA.85.010101. URL: https://link.aps.org/doi/10.1103/PhysRevA.85.010101.

[36] Sammy Ragy, Marcin Jarzyna, and Rafał Demkowicz-Dobrzański. "Compatibility in Multiparameter Quantum Metrology". In: *Phys. Rev. A* 94.5 (2016), p. 052108. DOI: 10.1103/PhysRevA.94.052108.

[37] C. Radhakrishna Rao and Somesh Das Gupta. *Selected Papers of C.R. Rao*. New York: Wiley, 1994. ISBN: 978-0-470-22091-7.

[38] Salvatore Savasta, Omar Di Stefano, and Raffaello Girlanda. "Light Quantization for Arbitrary Scattering Systems". In: *Phys. Rev. A* 65.4 (2002), p. 043801. DOI: 10.1103/PhysRevA.65.043801.

[39] Marlan O. Scully, M. Suhail Zubairy, and Ian A. Walmsley. "Quantum Optics". In: *Am. J. Phys.* (1999). ISSN: 0002-9505. DOI: 10.1119/1.19344.

[40] Eugene A Sharkov. *Passive Microwave Remote Sensing of the Earth: Physical Foundations*. Berlin; London: Springer, 2011.

[41] Mankei Tsang, Francesco Albarelli, and Animesh Datta. "Quantum Semiparametric Estimation". In: *Physical Review X* 10.3 (2020), p. 031023. DOI: 10.1103/PhysRevX.10.031023. URL: https://link.aps.org/doi/10.1103/PhysRevX.10.031023.

[42] Mankei Tsang, Ranjith Nair, and Xiao-Ming Lu. "Quantum Theory of Superresolution for Two Incoherent Optical Point Sources". In: *Phys. Rev. X* 6.3 (2016), p. 031033. DOI: 10.1103/PhysRevX.6.031033.

[43] Christopher S. Wang et al. "Efficient Multiphoton Sampling of Molecular Vibronic Spectra on a Superconducting Bosonic Processor". In: *Phys. Rev. X* 10 (2 June 2020), p. 021060. DOI: 10.1103/PhysRevX.10.021060. URL: https://link.aps.org/doi/10.1103/PhysRevX.10.021060.

[44] Christian Weedbrook et al. "Gaussian Quantum Information". In: *Rev. Mod. Phys.* 84.2 (2012), pp. 621–669. DOI: 10.1103/RevModPhys.84.621. URL: https://link.aps.org/doi/10.1103/RevModPhys.84.621.

[45] Jing Yang et al. "Optimal Measurements for Quantum Multiparameter Estimation with General States". In: *Physical Review A* 100.3 (2019), p. 032104. DOI: 10.1103/PhysRevA.100.032104. URL: https://link.aps.org/doi/10.1103/PhysRevA.100.032104.

[46] F. Zernike. "The Concept of Degree of Coherence and Its Application to Optical Problems". In: *Physica* 5.8 (1938), pp. 785–795. DOI: 10.1016/S0031-8914(38)80203-2. URL: https://linkinghub.elsevier.com/retrieve/pii/S0031891438802032.

[47] Jonas Zmuidzinas. "Cramér–Rao Sensitivity Limits for Astronomical Instruments: Implications for Interferometer Design". In: *J. Opt. Soc. Amer. A* 20.2 (2003), p. 218. DOI: 10.1364/JOSAA.20.000218. URL: https://www.osapublishing.org/abstract.cfm?URI=josaa-20-2-218.

[48] Jonas Zmuidzinas. “Thermal Noise and Correlations in Photon Detection”. In: *Appl. Opt.* 42.25 (2003), p. 4989. DOI: 10.1364/AO.42.004989. URL: https://www.osapublishing.org/abstract.cfm?URI=ao-42-25-4989.

Appendix: publications

First Publication

Quantum-enhanced passive remote sensing

Emre Köse [1,*] Gerardo Adesso [2,†] and Daniel Braun [1,‡]
[1]*Institut für Theoretische Physik, Eberhard Karls Universität Tübingen, 72076 Tübingen, Germany*
[2]*School of Mathematical Sciences, University of Nottingham, University Park, Nottingham NG7 2RD, United Kingdom*

(Received 23 December 2021; accepted 6 June 2022; published 6 July 2022)

We investigate theoretically the ultimate resolution that can be achieved with passive remote sensing in the microwave regime used, e.g., on board of satellites observing Earth, such as the soil moisture and ocean salinity (SMOS) mission. We give a fully quantum mechanical analysis of the problem, starting from thermal distributions of microscopic currents on the surface to be imaged that lead to a mixture of coherent states of the electromagnetic field which are then measured with an array of antennas. We derive the optimal detection modes and measurement schemes that allow one to saturate the quantum Cramér-Rao bound for the chosen parameters that determine the distribution of the microscopic currents. For parameters comparable to those of SMOS, a quantum enhancement of the spatial resolution by more than a factor of 20 should be possible with a single measurement and a single detector, and a resolution down to the order of 1 m and less than a $\frac{1}{10}$ K for the theoretically possible maximum number of measurements.

DOI: 10.1103/PhysRevA.106.012601

I. INTRODUCTION

Optical imaging has evolved dramatically since the discovery that Abbe's and Rayleigh's resolution limit comparable to the wavelength of the used light is not a fundamental bound. This was demonstrated experimentally with a series of works starting with stimulated emission depletion in 1994 by Hell [1], who showed that decorating molecules with fluorophores and quenching these selectively, imaging of a molecule with nanometer resolution could be achieved in the optical domain (see [2] for a review). This was followed in 2016 by theoretical work by Tsang and coworkers [3] who framed the problem of the ultimate resolution of two-point sources in terms of quantum parameter estimation, a very natural approach given that quantum parameter estimation theory was originally motivated by generalizing the classical Cramér-Rao bound that had long been used in radar detection to the optical domain [4–7]. Tsang and coworkers showed that even in the limit of vanishing spatial separation between the two sources a finite quantum Fisher information (QFI) for that parameter remains, whereas the classical Fisher information degrades in agreement with Rayleigh's bound [8]. A large body of theoretical work followed that incorporated important concepts such as the point spread function for analyzing optical lens systems, and mode engineering such as SPADE for optimal detection modes [8–25], reminiscent of the engineering of a "detector mode" for single-parameter estimation of light sources [26]. Experimental work in recent years validated this new approach to imaging [27–30]. Optical interferometers were investigated in [21,31–33]. The resolution for general parameter estimation for weak thermal sources was studied in [34]. Recently, the spatial resolution of two point sources for two-mode interferometers was examined for the far-field regime [35].

In this work, we investigate the ultimate limits of passive remote sensing in the microwave regime with a satellite of the surface of Earth. There, the state of the art is the use of antenna arrays for synthesizing interferometrically a large antenna with corresponding enhanced resolution. For example, the SMOS (soil moisture and ocean salinity) interferometer achieves a resolution of about 35 km, flying at the height of about 758 km and using a Y-shaped array of 69 antenna [36–39]. Each antenna measures in a narrow frequency band 1420–1427 MHz with a central wavelength around $\lambda \sim 21$ cm and in real time the electric fields corresponding to the thermal noise emitted by Earth according to the local brightness temperatures on its surface. The signals are filtered and interfered numerically, implementing thus purely classical interference, which implies a resolution governed by the van Cittert–Zernike theorem [40–42]. Recently, it was shown theoretically that larger baselines can be synthesized by using the motion of the satellite but at the price of the radiometric (i.e., temperature) resolution [43]. The question naturally arises to what extent the resolution can be improved by using methods of quantum metrology. As in the optical domain the answer can be found by analyzing the quantum Cramér-Rao bound and then trying to find the optimal measurements that can achieve it. We solve this problem, in general, for an arbitrary antenna array defined by the positions of individual antenna, in the sense of finding, at least numerically, the optimal modes for measuring the electric fields. We go beyond the situation of localized point sources that has become a favorite simplification in the field and describe the sources as randomly fluctuating microscopic current distributions which in turn generate the electromagnetic field noise, ultimately measured by the

*saban-emre.koese@uni-tuebingen.de
†gerardo.adesso@nottingham.ac.uk
‡daniel.braun@uni-tuebingen.de

satellite. This is closer to the literature on passive remote sensing in the microwave regime and allows a direct comparison with the van Cittert–Zernike theorem. We also make use of the scattering matrix formalism introduced in this context in [44]. The thermal fluctuations of the microscopic currents lead to Gaussian states of the microwave field [26,45–47], and our analysis makes therefore heavy use of the quantum Cramér-Rao bound (QCRB) for Gaussian states [48–53]. We assume that only the current densities at the surface of Earth contribute. In reality, the emission seen by the SMOS is from a surface layer on Earth that has a finite thickness, but is thin enough to make a two-dimensional (2D) approximation. Also, the receivers see the emission from the cosmic microwave background. We neglect it as its temperature is two orders of magnitude lower than the one of Earth [43]. Additional technical noises are neglected and indeed beyond the scope of this paper. Additional technical noises in the context of imaging were considered in Refs. [54–56].

The rest of the paper is organized as follows. In Sec. II, we describe the state for the n-mode interferometer for general sources on the source plane using the scattering matrix formalism. Later, we present the general formula of the positive-operator-valued measure (POVM) for the QFI based on the state of the n-mode interferometer. In Sec. III, first, we discuss the QFI for the parameters, source size, and temperature of a single uniform circular source for both a single antenna and two antennas. Second, we discuss the spatial resolution, source separation, and centroid on the source plane, of two strong point sources with the same and different temperatures for a two-mode interferometer. Third, we examine an array of antennas to increase the spatial resolution of a uniform circular source and two-point sources. We conclude in Sec. IV.

II. THEORY

A. Continuous vector potential and interaction with classical current sources

The operators for the quantized vector potential $\mathbf{A}(\mathbf{r},t)$ can be written in continuous form. The operator for the vector potential in the Coulomb gauge reads as [57,58]

$$\hat{\mathbf{A}}(\mathbf{r},t)=\int d^3k\left(\frac{\hbar}{16\pi^3\varepsilon_0 c|\mathbf{k}|}\right)^{1/2}\times\sum_{\sigma=1,2}\boldsymbol{\varepsilon}(\mathbf{k},\sigma)\hat{a}(\mathbf{k},\sigma)\exp(-ic|\mathbf{k}|t+i\mathbf{k}\cdot\mathbf{r})+\text{H.c.},\tag{1}$$

where, $\hat{a}(\mathbf{k},\sigma)$ are the continuous mode operators with $[\hat{a}(\mathbf{k},\sigma),\hat{a}^\dagger(\mathbf{k},\sigma)]=\delta(\mathbf{k}-\mathbf{k}')\delta_{\sigma\sigma'}$, and $\boldsymbol{\varepsilon}(\mathbf{k},\sigma)$ are the directions of the polarizations with index $\sigma\in 1,2$, which are always perpendicular to wave vector $\mathbf{k}$. Mode functions are plane waves and parametrized by $\mathbf{k}$ and σ. The interaction Hamiltonian for the classical current distribution of the sources $\mathbf{j}(\mathbf{r},t)$ with electromagnetic waves in free space is given by [43,58–60]

$$H_I(t)=-\int d^3r\,\mathbf{j}(\mathbf{r},t)\cdot\hat{\mathbf{A}}(\mathbf{r},t).\tag{2}$$

In the interaction picture, using the Schrödinger equation the state of the electromagnetic field at time t can be obtained from the one at t_0 as [58–61]

$$|\psi(t)\rangle=U(t,t_0)|\psi(t_0)\rangle,\tag{3}$$

where the $U(t,t_0)$ is given by

$$U(t,t_0)=\exp\left(\frac{i}{\hbar}\int_{t_0}^{t}dt'\int d^3r\,\mathbf{j}(\mathbf{r},t')\cdot\hat{\mathbf{A}}(\mathbf{r},t')+i\varphi(t,t_0)\right).\tag{4}$$

The phase $\varphi(t,t_0)$ is a real number, which arises from the classical interaction between the currents. It is independent of the state on which the propagator acts, and cancels in the calculation of equal-time matrix elements. Since the current density commutes with the vector potential, one can write the time evolution in the form of a displacement operator, which is given by

$$D(\{\alpha(\mathbf{k},\sigma)\})=\exp\left[\sum_\sigma\int d^3k\,[\alpha(\mathbf{k},\sigma)\hat{a}^\dagger(\mathbf{k},\sigma)-\alpha^*(\mathbf{k},\sigma)\hat{a}(\mathbf{k},\sigma)]\right],\tag{5}$$

where $\alpha(\mathbf{k},\sigma)$ can be found as

$$\alpha(\mathbf{k},\sigma)=\frac{i}{\hbar}\left(\frac{\hbar}{16\pi^3\varepsilon_0 c|\mathbf{k}|}\right)^{1/2}\int_{t_0}^{t}dt'\int d^3r\,\mathbf{j}(\mathbf{r},t')\cdot\boldsymbol{\varepsilon}(\mathbf{k},\sigma)\times\exp(ic|\mathbf{k}|t'-i\mathbf{k}\cdot\mathbf{r}).\tag{6}$$

The $\alpha(\mathbf{k},\sigma)$ also depends on t and t_0. We assume that for $t_0\to-\infty$ we have the vacuum state $|\{0\}\rangle$ for all modes. For a deterministic current density, $|\psi(t)\rangle$ is a tensor product of coherent states,

$$|\psi(t)\rangle=|\{\alpha(\mathbf{k},\sigma)\}\rangle=D[\{\alpha(\mathbf{k},\sigma)\}]|\{0\}\rangle.\tag{7}$$

One can introduce the Fourier transform (FT) of the current densities and take the t' integral immediately [43]. We introduce the Fourier decomposition of current density as

$$\mathbf{j}(\mathbf{r},t')=\frac{1}{\sqrt{2\pi}}\int_{-\infty}^{\infty}d\tilde{\omega}\,\tilde{\mathbf{j}}(\mathbf{r},\tilde{\omega})\exp(i\tilde{\omega}t').\tag{8}$$

Then we can write $\alpha(\mathbf{k},\sigma)$ in the form

$$\alpha(\mathbf{k},\sigma)=\frac{i}{\hbar}\left(\frac{\hbar}{32\pi^4\varepsilon_0 c|\mathbf{k}|}\right)^{1/2}\times\int_{-\infty}^{t}dt'\int d^3r\int_{-\infty}^{\infty}d\tilde{\omega}\,\tilde{\mathbf{j}}(\mathbf{r}',\tilde{\omega})\cdot\boldsymbol{\varepsilon}(\mathbf{k},\sigma)\times\exp(ic|\mathbf{k}|t'-i\mathbf{k}\cdot\mathbf{r})\exp(i\tilde{\omega}t').\tag{9}$$

Taking the integral over t' gives

$$\alpha(\mathbf{k},\sigma)=-\left(\frac{1}{32\pi^4\varepsilon_0 c\hbar|\mathbf{k}|}\right)^{1/2}\times\int d^3r\int_{-\infty}^{\infty}d\tilde{\omega}\,\tilde{\mathbf{j}}(\mathbf{r},\tilde{\omega})\cdot\boldsymbol{\varepsilon}(\mathbf{k},\sigma)\exp(-i\mathbf{k}\cdot\mathbf{r})\times\frac{\exp[i(\tilde{\omega}+c|\mathbf{k}|)t]}{i\epsilon-c|\mathbf{k}|-\tilde{\omega}}.\tag{10}$$

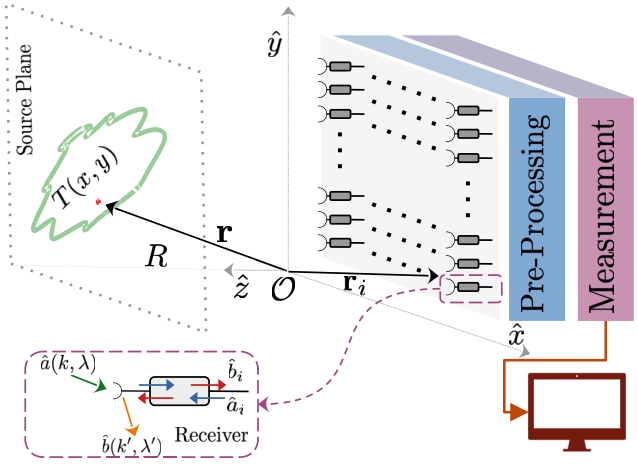

FIG. 1. An interferometer, with n antennas, separated by a distance R from the source plane. The $T_{\text{eff}}(x,y)$ is the position-dependent effective temperature in the source plane that one wants to measure. The field $\hat{a}(\mathbf{k},\sigma)$ propagating from the source enters the receiver on the interferometer and is partly reflected back into the modes $\hat{b}(\mathbf{k},\sigma)$. Single $\hat{b}_i$ exit the receiver and are combined in a preprocessing step, while other single modes $\hat{a}_i$ are scattered back from the preprocessing step. The preprocessing of modes allows a nonlocal measurement by combining the modes $\hat{b}_i$ with beam splitters and phase shifters. We denote the origin of the coordinate system on the detection plane as $\mathcal{O}$. All the components of the vectors are donated in the coordinate system $\mathcal{R} = (\mathcal{O}, \hat{e}_x, \hat{e}_y, \hat{e}_z)$.

We introduced a shift in the denominator "$i\epsilon$" that is necessary for the integral to converge at $t = -\infty$.

B. State received by the antennas

The electromagnetic field is received by an interferometer that has an array of antennas, localized at positions $\mathbf{r}_i$ in a plane. The detection plane of antennas is parallel to the source plane and separated from it by a distance R (see Fig. 1). Each antenna is connected at its output to a waveguide that channels the received electromagnetic field radiation towards the measurement instruments. Receiver "i" consists of antenna "i" combined with its output waveguide. Its output, possibly after filtering, is assumed to be single mode with discrete annihilation operator $\hat{b}_i$. We call the modes received by the antennas "spatial field modes" since each mode $\hat{b}_i$ is specific to a location on the detection plane. Single modes with discrete annihilation operator $\hat{a}_i$ are reflected from the preprocessing stage. On the antenna side, we represent incoming plane waves in the interferometer by $\hat{a}(\mathbf{k},\sigma)$ and scattered outgoing plane waves by $\hat{b}(\mathbf{k},\sigma)$ (see Fig. 1). One can use the scattering matrix formalism to find the relation between incoming and outgoing modes.

Furthermore, the modes $\hat{b}_i$ are separated by distances substantially larger than the central wavelength λ. And the collection area of each antenna A_D is assumed to be $A_D \sim \lambda^2$, where λ is central wavelength. These constraints make the modes for different receivers orthogonal and simplifies the form of the scattering matrix. A scattering matrix connects incoming and outgoing modes, and one can write it as [62,63]

$$\mathcal{S} = \begin{bmatrix} \mathcal{S}^{(\text{scat})} & \mathcal{S}^{(\text{trans})} \\ \mathcal{S}^{(\text{rec})} & \mathcal{S}^{(\text{refl})} \end{bmatrix}. \tag{11}$$

This matrix acts on the vector $[\{\hat{a}(\mathbf{k},\sigma)\}_{\{\mathbf{k},\sigma\}}, \{\hat{a}_i\}_{\{i\}}]^T$, where $\{a(\mathbf{k},\sigma)\}_{\{\mathbf{k},\sigma\}}$ is the vector of continuous plane-wave operators with continuous $\mathbf{k}$ and two polarizations. $\{\hat{a}_i\}_{\{i\}}$ is the vector of modes with $i \in \{1,\ldots,n\}$ for an n-mode interferometer. The first block, $\mathcal{S}^{(\text{scat})}$, describes the scattering of incoming plane waves to outgoing plane waves from the interferometer. A receiver can receive or transmit the signal. The off-diagonal block $\mathcal{S}^{(\text{rec})}$ describes the coupling of the incoming plane waves $\hat{a}(\mathbf{k},\sigma)$ into the receiver modes $\hat{b}_i$, and $\mathcal{S}^{(\text{trans})}$ describes scattering of reflected receiver modes $\hat{a}_i$ into outgoing plane waves $\hat{b}(\mathbf{k},\sigma)$. The matrix $\mathcal{S}^{(\text{refl})}$ represents the scattering (reflection) between the receivers, and will be neglected, $\mathcal{S}^{(\text{refl})} \sim 0$. One can also verify that if the receivers have only incoming and outgoing modes, the receiving and transmitting pattern of the receivers will be the same $\mathcal{S}^{(\text{trans})}(\mathbf{k},\sigma;j) = \mathcal{S}^{(\text{rec})}(j;\mathbf{k},\sigma)$ and we can denote them as simply $\mathcal{S}_j(\mathbf{k},\sigma)$. Formally, the input-output relations read as

$$\hat{b}(\mathbf{k},\sigma) = \sum_{\sigma'} \int d^3\mathbf{k}' \mathcal{S}^{(\text{scat})}(\mathbf{k},\mathbf{k}',\sigma,\sigma')\hat{a}(\mathbf{k}',\sigma') + \sum_j \mathcal{S}_j(\mathbf{k},\sigma)\hat{a}_j \tag{12}$$

and

$$\hat{b}_i = \sum_{\sigma} \int d^3\mathbf{k}\, \mathcal{S}_i(\mathbf{k},\sigma)\hat{a}(\mathbf{k},\sigma). \tag{13}$$

For a lossless system we assume that $S^\dagger S = I$. Then we write $\mathcal{S}^{(\text{scat})}(\mathbf{k},\mathbf{k}',\sigma,\sigma') = (\mathcal{S}^{(\text{scat})})^T(\mathbf{k}',\mathbf{k},\sigma',\sigma)$. The field operators $\hat{a}(\mathbf{k},\sigma)$ from the state that we have for Eq. (7) can be replaced by the following relation for n different receiver modes:

$$\hat{a}(\mathbf{k},\sigma) = \sum_j^n \mathcal{S}_j^*(\mathbf{k},\sigma)\hat{b}_j + \sum_{\sigma'} \int d^3\mathbf{k}' \mathcal{S}^{*(\text{scat})}(\mathbf{k}',\sigma',\mathbf{k},\sigma)\hat{b}(\mathbf{k}',\sigma'). \tag{14}$$

The interferometer does not have any access to modes $\hat{b}(\mathbf{k},\sigma)$. Assuming that all antennas are identical in terms of their receiver pattern, except for their position $\mathbf{r}_i$ on the detection plane, each scattering function may be written as [62,63]

$$\mathcal{S}_i(\mathbf{k},\sigma) = e^{i(\mathbf{k}\cdot\mathbf{r}_i - \omega t_i)}\mathcal{S}(\mathbf{k},\sigma), \tag{15}$$

where t_i is the time at which we consider the state of the ith antenna. Since we are only interested in spatial modes, we assume that relative time differences between any pair of antennas is zero. Then we write $t_i \equiv \bar{t}$, with $\bar{t}$ the time when the signal from $(\mathbf{r},t)$ arrives at central antenna. And $\mathcal{S}(\mathbf{k},\sigma)$ is the function describes scattering to the central receiver. According to (14), t is the last time the current densities to be sensed imprint their information the coherent state labels $\alpha(\boldsymbol{k},\sigma)$. Further, the commutation relation of different receiver modes

can be written as

$$[\hat{b}_i, \hat{b}_j^\dagger] = \sum_\sigma \int d^3\mathbf{k}\, \mathcal{S}_i(\mathbf{k},\sigma)\mathcal{S}_j^*(\mathbf{k},\sigma) \approx \delta_{ij}, \tag{16}$$

where we have used the canonic commutation relation of $\hat{a}(\mathbf{k},\sigma)$ and we assumed that $|\mathcal{S}(\mathbf{k},\sigma)|$ varies slowly compared to the oscillations of the exponential factor $\exp[i\mathbf{k}\cdot(\mathbf{r}_i-\mathbf{r}_j)]$ for $i \neq j$. Since $\hat{b}_i$ commutes with $\hat{b}(\mathbf{k},\sigma)$, using Eq. (14) we can write the coherent state in Eq. (7) as

$$|\psi(t)\rangle = D(\{\beta_i\})D[\{\beta(\mathbf{k},\sigma)\}]|\{0\}\rangle, \tag{17}$$

where $D[\{\beta(\mathbf{k},\sigma)\}]$ can be defined similarly to Eq. (5) and $\beta(\mathbf{k},\sigma)$ is the eigenvalue of the scattered plane-wave modes with annihilation operator $\hat{b}(\mathbf{k},\sigma)$. Since the interferometer does not have any access to these modes, we can safely trace them out. The displacement operator for the spatial modes of the interferometer can be written in the form

$$D(\{\beta_i\}) = \bigotimes_i^n \exp[\beta_i\hat{b}_i^\dagger - \beta_i^*\hat{b}_i]. \tag{18}$$

Then we have a coherent state for spatial modes of the interferometer,

$$\rho' = |\{\beta_i\}\rangle\langle\{\beta_i\}|, \tag{19}$$

where

$$\beta_i = \sum_\sigma \int d^3k\, \mathcal{S}_i(\mathbf{k},\sigma)\alpha(\mathbf{k},\sigma). \tag{20}$$

$\mathcal{S}_i(\mathbf{k},\sigma)$ depends on the type of receivers. Let us assume that each receiver is characterized by a filter function $w(\omega)$ with central frequency ω_0 and bandwidth $B \ll \omega_0$:

$$w(\omega) = \begin{cases} 1 & \text{for } \omega_0 - B/2 \leqslant \omega \leqslant \omega_0 + B/2, \\ 0 & \text{elsewhere.} \end{cases} \tag{21}$$

For simplicity we assume $\mathcal{S}(\mathbf{k},\sigma) \propto \sqrt{\omega}w(\omega)\boldsymbol{\varepsilon}(\mathbf{k},\sigma)\cdot\hat{u}$, and normalized according to Eq. (16) as

$$\mathcal{S}(\mathbf{k},\sigma) = \left(\frac{3c^3\omega}{8\pi\omega_0^3 B}\right)^{1/2} w(\omega)\boldsymbol{\varepsilon}(\mathbf{k},\sigma)\cdot\hat{u}, \tag{22}$$

where $\omega = c|\mathbf{k}|$ and $\hat{u}$ is the unit polarization direction of the corresponding receiver mode. Since we are using a filter function and $\mathcal{S}(\mathbf{k},\sigma)$ is normalized, choosing $\sqrt{\omega}$ or with a different power will not change the result in Eq. (28). Yet, in Eq. (25) we have the term $\sim\omega\tilde{\mathbf{j}}_t(\mathbf{r},\omega)$ by this choice and it is consistent with the van Cittert–Zernike theorem given in Ref. [42]. Then we have

$$\begin{aligned}\beta_i =& -\left(\frac{3c^3}{2^8\hbar\varepsilon_0\pi^5\omega_0^3 B}\right)^{1/2}\int d^3r \int_{-\infty}^{\infty} d\tilde{\omega} \\ &\times \sum_\sigma \int d^3k\, w(\omega)\tilde{\mathbf{j}}(\mathbf{r},\tilde{\omega})\cdot\boldsymbol{\varepsilon}(\mathbf{k},\sigma)\boldsymbol{\varepsilon}(\mathbf{k},\sigma)\cdot\hat{u} \\ &\times \frac{e^{i(\tilde{\omega}t+\omega t-\omega\bar{t})}e^{-i\mathbf{k}\cdot(\mathbf{r}-\mathbf{r}_i)}}{i\epsilon - c|\mathbf{k}| - \tilde{\omega}}.\end{aligned} \tag{23}$$

To take the integral over d^3k we align the k_z axis with the vector $(\mathbf{r}-\mathbf{r}_i)$. In spherical coordinates in k space we have $d^3k = \omega^2/c^3 d\omega\, d\Omega$, where $\omega = |\mathbf{k}|c$ and $\mathbf{k} = (\omega/c)\hat{\mathbf{n}}(\Omega)$ with $\hat{\mathbf{n}}(\Omega) = (\sin\theta\cos\phi, \sin\theta\sin\phi, \cos\theta)$. The frequencies will be filtered out by the filter function $w(\omega)$ and later only the integral over the surface from a distance R will be considered in the far-field regime ($R\omega_0/c \gg 1$). Then in this step, we can drop the terms of order $1/f^2$ and $1/f^3$ with $f \equiv \omega|\mathbf{r}-\mathbf{r}_i|/c$. Taking the integral over Ω, summing over two polarizations, considering that our problem is limited to far field we have

$$\begin{aligned}\beta_i =& i\left(\frac{3c\mu_0}{64\hbar\pi^3\omega_0^3 B}\right)^{1/2}\int d^3r \int_{-\infty}^{\infty} d\tilde{\omega}\int_0^\infty d\omega\, w(\omega)\omega \\ &\times \tilde{\mathbf{j}}_t(\mathbf{r},\tilde{\omega})\cdot\hat{u}\frac{e^{i\omega|\mathbf{r}-\mathbf{r}_i|/c} - e^{-i\omega|\mathbf{r}-\mathbf{r}_i|/c}}{|\mathbf{r}-\mathbf{r}_i|}\frac{e^{i(\tilde{\omega}t+\omega t-\omega\bar{t})}}{i\epsilon-\omega-\tilde{\omega}},\end{aligned} \tag{24}$$

where $\tilde{\mathbf{j}}_t(\mathbf{r},\tilde{\omega})$ is the locally transverse component of the current density defined as $\tilde{\mathbf{j}}_t = \tilde{\mathbf{j}} - (\tilde{\mathbf{j}}\cdot\hat{e}_\mathbf{r})\hat{e}_\mathbf{r}$ with unit vector $\hat{e}_\mathbf{r} = (\mathbf{r}-\mathbf{r}_i)/|\mathbf{r}-\mathbf{r}_i|$. For $R \gg |\mathbf{r}_i|$, we have $\hat{e}_\mathbf{r} \approx \mathbf{r}/|\mathbf{r}|$, with corrections modifying only slightly the prefactors, not the phases. One can extend the lower bound of the integration range of the ω integral to $-\infty$ using the definition of $w(\omega)$, and evaluate the ω integral with the help of the law of residues. Since $\bar{t} > t - |\mathbf{r}-\mathbf{r}_i|/c$, the pole at $\omega = -\tilde{\omega} + i\epsilon$ contributes to the term $\exp(i\omega|\mathbf{r}-\mathbf{r}_i|/c)$. For $\exp(-i\omega|\mathbf{r}-\mathbf{r}_i|/c)$ the contour must be closed in the lower half-plane and there is no pole to contribute. In the end one should send $\epsilon \to 0$. Then β_i simplifies to

$$\begin{aligned}\beta_i =& -\left(\frac{3c\mu_0}{16\pi\hbar\omega_0^3 B}\right)^{1/2}\int_{-\infty}^{\infty} d\omega\, w(-\omega)\omega\int d^3r \\ &\times \tilde{\mathbf{j}}_t(\mathbf{r},\omega)\cdot\hat{u}\frac{e^{-i\omega(\bar{t}-|\mathbf{r}-\mathbf{r}_i|/c)}}{|\mathbf{r}-\mathbf{r}_i|},\end{aligned} \tag{25}$$

where we drop the "$\sim$" from $\tilde{\omega}$. The state in Eq. (7) is written for a deterministic current density distribution. In reality, these current densities fluctuate. Before we move forward, we describe the properties of this current density distribution. We assume that it is a complex symmetric Gaussian process with current densities uncorrelated in positions, directions, and frequencies [43,64,65],

$$\begin{aligned}&\langle\tilde{j}_l(\mathbf{r},\omega)\tilde{j}_m^*(\mathbf{r}',\omega')\rangle = \frac{l_c^3}{\tau_c}\delta_{lm}\delta(\omega-\omega')\delta(\mathbf{r}-\mathbf{r}')\langle|\tilde{j}_l(\mathbf{r},\omega)|^2\rangle, \\ &\langle\tilde{j}_l(\mathbf{r},\omega)\tilde{j}_m(\mathbf{r}',\omega')\rangle = 0, \quad \langle\tilde{j}_l^*(\mathbf{r},\omega)\tilde{j}_m^*(\mathbf{r}',\omega')\rangle = 0.\end{aligned} \tag{26}$$

The length scale l_c and timescale τ_c are introduced for dimensional grounds and the polarizations are indexed by l, m taking values x, y, z. For the classical white-noise currents Eq. (26) is a standard model, and appears in many places in the literature [66–68]. One can also derive Planck's law for the energy density of an electromagnetic field in thermal equilibrium from it (see Appendix of Ref. [43]). We choose the unit polarization vector of the receiver $\hat{u}$ as one of the basis vectors of the coordinate system $\mathcal{R}$ parallel to the detection plane, in either x or y direction. Then, we write $\langle\tilde{\mathbf{j}}_t(\mathbf{r},\omega)\cdot\hat{u}\tilde{\mathbf{j}}_t^*(\mathbf{r},\omega)\cdot\hat{u}\rangle = \langle|\tilde{j}_{t,l}(\mathbf{r},\omega)|^2\rangle$. Using Eq. (19) and introducing the distribution of the current density $P(\tilde{j}(r,\omega))$, the state for the interferometer ρ_{int} with n receivers can be

written as

$$\rho_{\rm int} = \int d^2\tilde{j}\, P(\tilde{j}(\mathbf{r},\omega))|\{\beta_i\}\rangle\langle\{\beta_i\}|. \tag{27}$$

The integral is over the complex $\tilde{j}$ plane. Since it is a circularly symmetric Gaussian process, $P(\tilde{j}(\mathbf{r},\omega))$ is assumed through its moments given in Eq. (26). Gaussian states are completely characterized by their mean displacement $\Gamma_i = \mathrm{Tr}[\rho \mathbf{b}_i]$ and covariance matrix with elements $\Sigma_{ij} = \frac{1}{2}\mathrm{Tr}[\rho(\tilde{\mathbf{b}}_i\tilde{\mathbf{b}}_j + \tilde{\mathbf{b}}_j\tilde{\mathbf{b}}_i)]$, where $\mathbf{b} = [b_1, b_1^\dagger, b_2, b_2^\dagger, \ldots, b_n, b_n^\dagger]$ and $\tilde{\mathbf{b}}_i = \mathbf{b}_i - \Gamma_i$ [26,69–73]. The mean displacement for our state is zero $\Gamma_i = 0$ considering Eq. (26). To find the elements of the covariance matrix, we need to calculate $\langle b_i^\dagger b_j\rangle$. The integral over ω can be taken using the filter function of bandwidth B. With this we find

$$\langle b_i^\dagger b_j\rangle = K\int d^3r\, \frac{\langle|\tilde{j}_{t,l}(\mathbf{r},\omega)|^2\rangle\, e^{i\omega_0(|\mathbf{r}-\mathbf{r}_j|-|\mathbf{r}-\mathbf{r}_i|)/c}}{|\mathbf{r}-\mathbf{r}_i||\mathbf{r}-\mathbf{r}_j|} \times \mathrm{sinc}\Big[\frac{B}{2c}(|\mathbf{r}-\mathbf{r}_j| - |\mathbf{r}-\mathbf{r}_i|)\Big], \tag{28}$$

where $K = 3c\mu_0 l_c^3/(16\pi\hbar\omega_0\tau_c)$ and $\mathrm{sinc}[x] \equiv \sin x/x$. For a very narrow bandwidth $\mathrm{sinc}[\ldots] \approx 1$. Then, Eq. (28) for $i = j$ becomes

$$\bar{n} = K\int d^3r\, \frac{\langle|\tilde{j}_{t,l}(\mathbf{r},\omega)|^2\rangle}{|\mathbf{r}-\mathbf{r}_i|^2}, \tag{29}$$

where we defined $\bar{n} \equiv \langle b_i^\dagger b_i\rangle$ without any index since the mean photon number is the same for all interferometer modes in the far-field approximation, and for $i \neq j$ it becomes

$$\xi_{ij} = K\int d^3r\, \frac{\langle|\tilde{j}_{t,l}(\mathbf{r},\omega)|^2\rangle\, e^{i\omega_0(|\mathbf{r}-\mathbf{r}_j|-|\mathbf{r}-\mathbf{r}_i|)/c}}{|\mathbf{r}-\mathbf{r}_i||\mathbf{r}-\mathbf{r}_j|} \tag{30}$$

with $\xi_{ij} \equiv \langle b_i^\dagger b_j\rangle$. The integral over Earth's surface is parametrized by $\mathbf{r} = (x, y, R)$ with respect to the coordinate system of the detection plane. Further, we write $|\mathbf{r}-\mathbf{r}_j| - |\mathbf{r}-\mathbf{r}_i| \approx \Delta\mathbf{r}_{ij}\cdot\mathbf{r}/|\mathbf{r}|$ for $|\Delta\mathbf{r}_{ij}| \ll R$, where $\Delta\mathbf{r}_{ij} = \mathbf{r}_j - \mathbf{r}_i$ connects two different receiver modes. In the denominator, we approximate $|\mathbf{r}-\mathbf{r}_i| \approx R/\cos\tilde{\theta}(x,y)$ with $\tilde{\theta}(x,y)$ the polar angle the angle between the z axis and the vector (x, y, R). One can relate the average amplitude of current density to brightness temperature $T_{\rm B}(x,y)$ by $\langle|\tilde{j}_{t,l}(\mathbf{r},\omega)|^2\rangle = K_1 T_{\rm B}(x,y)\cos\tilde{\theta}(x,y)\delta(z-R)$ with a constant defined as $K_1 = 32\tau_c k_B/(3l_c^3\mu_0 c)$ (see Appendix A). We define the effective temperature as $T_{\rm eff}(x,y) \equiv T_{\rm B}(x,y)\cos^3\tilde{\theta}(x,y)$ and a new constant $\kappa = K_1 K \equiv 2k_B/(\pi\hbar\omega_0)$ where κ has the dimension of inverse temperature with SI units "1/K." Then we can simplify Eq. (29) for $i = j$ as

$$\bar{n} = \frac{\kappa}{R^2}\int dx\, dy\, T_{\rm eff}(x,y), \tag{31}$$

and for $i \neq j$ as

$$\xi_{ij} = \frac{\kappa}{R^2}\int dx\, dy\, T_{\rm eff}(x,y) e^{2\pi i(v_x^{ij}x + v_y^{ij}y)}, \tag{32}$$

where

$$v_y^{ij} = \frac{\Delta x_{ij}}{\lambda R}, \qquad v_x^{ij} = \frac{\Delta y_{ij}}{\lambda R}. \tag{33}$$

We used $\omega_0/c = 2\pi/\lambda$. These two equations suffice to determine the covariance matrix elements of the Gaussian states for the general interferometer with an array of antennas. All spatial field modes received by the interferometer undergo a preprocessing before measurement. This processing can be understood as a linear combination of all spatial modes in such a way to achieve the optimal POVM for the best estimation of the parameter we are interested in (see Sec. II C). We use the values of the SMOS for the rest of the paper which leads to $\kappa \sim 9.4$ 1/K.

C. Quantum Cramér-Rao bound

A lower bound of an unbiased estimator of a deterministic parameter is given by the Cramér-Rao bound (CRB), which states that the variance of any such estimator is equal or greater than the inverse of the Fisher information. The quantum analog of the CRB is the quantum Cramér-Rao bound (QCRB), given by the inverse of the QFI. The significance of the QCRB lies in the fact that in the case of a single parameter to be estimated the bound can in principle be saturated in the limit of infinitely many measurements when choosing the optimal quantum measurement and maximum-likelihood estimation. Let us consider a quantum state $\rho_{\boldsymbol{\mu}}$ that depends on a vector of l parameters, $\boldsymbol{\mu} = (\mu_1, \mu_2, \ldots, \mu_l)^T$. One can generalize the single-parameter QCRB [4,5] to the multiparameter QCRB [74] given for a single measurement by

$$\mathrm{Cov}(\tilde{\boldsymbol{\mu}}) \geqslant \mathscr{F}(\boldsymbol{\mu})^{-1}, \quad \mathscr{F}_{ij}(\boldsymbol{\mu}) = \tfrac{1}{2}\,\mathrm{tr}\,(\rho_{\boldsymbol{\mu}}\{\mathscr{L}_i, \mathscr{L}_j\}), \tag{34}$$

where $\mathrm{Cov}(\tilde{\boldsymbol{\mu}})$ is a covariance matrix for the locally unbiased estimator $\tilde{\boldsymbol{\mu}}(x)$ [48,53], the $\{\cdot,\cdot\}$ means the anticommutator, and $\mathscr{L}_i$ is the symmetric logarithmic derivative (SLD) related to parameter i, which is defined similarly to the single-parameter case $\frac{1}{2}(\mathscr{L}_i\rho_{\boldsymbol{\mu}} + \rho_{\boldsymbol{\mu}}\mathscr{L}_i) = \partial_i\rho_{\boldsymbol{\mu}}$. For any given positive weight matrix $\boldsymbol{W}$, the estimation cost is bounded by $\mathrm{Tr}[\boldsymbol{W}\,\mathrm{Cov}(\tilde{\boldsymbol{\mu}})] \geqslant \mathrm{Tr}[\boldsymbol{W}\mathscr{F}(\boldsymbol{\mu})^{-1}] \equiv C^S(\boldsymbol{\mu},\boldsymbol{W})$. Contrary to the single-parameter case, the multiparameter QCRB can in general not be saturated. This problem was realized by Holevo [52]. He proposed a tighter and more fundamental bound $C^H(\boldsymbol{\mu},\boldsymbol{W})$, which is upper bounded by $2C^S(\boldsymbol{\mu},\boldsymbol{W})$ [75,76]. In case of the asymptotically classical models, where SLD operators for different parameters commute on average $\mathrm{Tr}(\rho_{\boldsymbol{\mu}}[L_i, L_j]) = 0$, the Holevo CRB is equivalent to the QCRB and it can be saturated asymptotically with a collective measurement on an asymptotically large number of copies $\rho_{\boldsymbol{\mu}}^{\otimes\mathcal{N}}$ [53,76].

The SLD and the elements of QFI matrix are given in Ref. [71] for any Gaussian state. The SLD can be written as

$$\mathscr{L}_i = \tfrac{1}{2}\mathfrak{M}^{-1}_{\alpha\beta,\gamma\delta}(\partial_i\Sigma^{\gamma\delta})(\mathbf{b}_\alpha\mathbf{b}_\beta - \Sigma^{\alpha\beta}), \tag{35}$$

where the summation convention is used. In our case, the mean displacement of Gaussian state is zero. Thus, we can simplify further the elements of the QFI matrix in [71] to

$$\mathscr{F}_{ij} = \tfrac{1}{2}\mathfrak{M}^{-1}_{\alpha\beta,\gamma\delta}\partial_j\Sigma^{\alpha\beta}\partial_i\Sigma^{\gamma\delta}, \tag{36}$$

where

$$\mathfrak{M} \equiv \Sigma\otimes\Sigma + \tfrac{1}{4}\Omega\otimes\Omega, \tag{37}$$

and $\Omega = \bigoplus_{k=1}^{n} i\sigma_y$. Using the properties of the Gaussian state (circularly symmetric and with zero mean) we can write the SLD for n-mode interferometers as

$$\mathscr{L}_i = \sum_{j}^{n} g_i^j \hat{b}_j^\dagger \hat{b}_j + \sum_{j<k}^{n} \left(g_i^{jk} \hat{b}_j^\dagger \hat{b}_k + \left(g_i^{jk}\right)^* \hat{b}_k^\dagger \hat{b}_j\right) + \mathrm{C}, \quad (38)$$

where C is a constant term. In the single-parameter case, the optimal POVM is the set of projectors onto eigenstates of $\mathscr{L}_i$. It allows one to saturate the QCRB in the limit of infinitely many measurements and maximum-likelihood estimation [4,77,78]. For the diagonalization of the SLD, the constant C is not important and we can drop it from the beginning. We construct a Hermitian matrix $\mathbf{M}_i$

$$\mathbf{M}_i = \begin{bmatrix} g_i^1 & g_i^{12} & \cdots & g_i^{1n} \\ (g_i^{12})^* & g_i^2 & \cdots & g_i^{2n} \\ \cdots & \cdots & \cdots & \cdots \\ (g_i^{1n})^* & (g_i^{2n})^* & \cdots & g_i^n \end{bmatrix}, \quad (39)$$

where the diagonal elements are real-valued functions which can be defined as $g_i^j = \mathfrak{M}^{-1}_{\alpha\beta,\gamma\delta}(\partial_i \Sigma^{\gamma\delta})$ with $\alpha = 2j$ and $\beta = 2j-1$. The off-diagonal elements are complex-valued functions which are defined as $g_i^{jk} = \mathfrak{M}^{-1}_{\alpha\beta,\gamma\delta}(\partial_i \Sigma^{\gamma\delta})$ with $\alpha = 2j$ and $\beta = 2k-1$ and $k > j$. Further, we can define a new set of operators $\bar{\mathbf{b}}^\dagger \equiv [\hat{b}_1^\dagger, \hat{b}_2^\dagger, \ldots, \hat{b}_n^\dagger]$ and $\bar{\mathbf{b}} \equiv [\hat{b}_1, \hat{b}_2, \ldots, \hat{b}_n]^T$. Then the SLD becomes

$$\mathscr{L}_i = \bar{\mathbf{b}}^\dagger \mathbf{M}_i \bar{\mathbf{b}}. \quad (40)$$

Since $\mathbf{M}_i$ is a Hermitian matrix, it can always be unitarily diagonalized by $\mathbf{M}_i = \mathbf{V}_i^\dagger \mathbf{D}_i \mathbf{V}_i$ with $\mathbf{V}_i^\dagger \mathbf{V}_i = I$. A new set of operators can be defined as $\bar{\mathbf{d}}_i^\dagger = \bar{\mathbf{b}}^\dagger \mathbf{V}_i^\dagger$ where $\bar{\mathbf{d}}_i^\dagger = [\hat{d}_{i1}^\dagger, \hat{d}_{i2}^\dagger, \ldots, \hat{d}_{in}^\dagger]$. The optimal POVM for the single-parameter case ($i = 1$, which we drop in the following) can be found as a set of projectors in the Fock basis $\{|m_1, m_2, \ldots, m_n\rangle \langle m_1, m_2, \ldots, m_n|\}_{\{m_1, m_2 \ldots m_n\}}$ of the $\hat{d}_l$ with $\hat{d}_l^\dagger \hat{d}_l |m_1, m_2, \ldots, m_n\rangle = m_l |m_1, m_2, \ldots, m_n\rangle$, where $l \in \{1, \ldots, n\}$. The $\hat{d}_l$ will be called "detection modes." In the case of multiparameter estimation, one needs to check the compatibility conditions to saturate the SLD-CRB. Thus, we give the general commutation relation of SLD in Appendix B for an n-mode interferometer. We see that the SLDs for $n < 3$ commute on average, $\mathrm{Tr}\,[\rho_{\mathrm{int}}[\mathscr{L}_i, \mathscr{L}_j]] = 0$, for any parameter estimation.

III. RESULTS

A. Single receiver

In this section, we consider the case of the simplest estimation of the parameters of the sources with a single receiver with mode $\hat{b}$. Then the covariance matrix for the state can be written as

$$\Sigma = \begin{bmatrix} 0 & \chi \\ \chi & 0 \end{bmatrix}. \quad (41)$$

The QFI matrix elements for single mode can be found as

$$\mathscr{F}_{ij} = \frac{4\partial_i \chi \, \partial_j \chi}{4\chi^2 - 1}, \quad (42)$$

and, up to the irrelavant constant, the SLD becomes

$$\mathscr{L}_i = \frac{4\partial_i \chi}{4\chi^2 - 1} \hat{b}^\dagger b. \quad (43)$$

Since the SLD is already diagonal in the basis of $\hat{b}^\dagger \hat{b}$, the detection mode can be considered as $\hat{b}$. We write the POVM obtained from the SLD as a set of projectors in the Fock basis $\{|m\rangle \langle m|\}_{\{m\}}$ which is the eigenbasis of $\hat{b}^\dagger \hat{b}$, $\hat{b}^\dagger \hat{b} |m\rangle \langle m| = m |m\rangle \langle m|$. To compare, we consider the POVM from heterodyne detection. The heterodyne detection uses a classical local oscillator to make a measurement locally on the basis of coherent states. For a single mode, its POVM elements can be written as $E(\nu) = |\nu\rangle \langle \nu| / \pi$ where $|\nu\rangle$ is coherent state and $\int d^2\nu \, E(\nu) = \mathbb{1}$. The probability that $E(\nu)$ triggers reads as

$$P(\nu|\mu_i) = \frac{1}{\pi(1+\bar{n})} \exp\left[-\frac{|\nu|^2}{(1+\bar{n})}\right], \quad (44)$$

with $\bar{n}$ given by Eq. (31). The classical Fisher information (CFI) for parameter μ_i can be written as

$$F_i = \int d^2\nu \frac{1}{P(\nu|\mu_i)} \left(\frac{\partial P(\nu|\mu_i)}{\partial \mu_i}\right)^2. \quad (45)$$

Resolution of a uniform circular source. Consider a source defined as a circular disk with radius a and with uniform temperature T located under the interferometer at a distance R [$\mathbf{r} = (0, 0, R)$]. We are interested in estimating a or T. While estimating one of them, we will assume that the other parameter is known to sufficiently large precision. The temperature distribution on the source plane becomes

$$T_{\mathrm{eff}}(x, y) = T \ \mathrm{circ}(x, y), \quad (46)$$

where the symbol circ$(\cdot)$ stands for the circular function, defined as

$$\mathrm{circ}(x, y) \triangleq \begin{cases} 1, & \sqrt{x^2 + y^2} \leqslant a \\ 0, & \sqrt{x^2 + y^2} > a. \end{cases} \quad (47)$$

We assume $a \ll R$. Then only small angles are involved and one can set $\cos^3 \Theta(x, y) \approx 1$. This corresponds to one of the approximations characteristic of the far-field regime [79]. Using Eq. (31), we have $\bar{n} = \pi a^2 \kappa T / R^2$ and $\chi = 1/2 + \bar{n}$. The QFI for estimating a becomes

$$\mathscr{F}_a = \frac{4\pi T \kappa}{R^2 + a^2 \pi T \kappa}. \quad (48)$$

Then we can write the SLD for estimating the a ignoring the constant term as

$$\mathscr{L}_a = \frac{2R^2}{aR^2 + a^3 \pi T \kappa} \hat{b}^\dagger \hat{b}. \quad (49)$$

The CFI of the heterodyne detection becomes

$$F_a = \frac{4a^2 \pi^2 T^2 \kappa^2}{(R^2 + a^2 \pi T \kappa)^2}. \quad (50)$$

In Fig. 2, we compare the QFI with the CFI of heterodyne detection. As one can see, for small source sizes, the Fisher information from heterodyne measurement vanishes. However, the QFI tends to a constant. For instance, in the limit $a \to 0$, for $T = 300$ K we have QFI for estimating a as $\mathscr{F}_a \sim 6.16 \times 10^{-2}$ 1/km^2, which gives a smallest standard

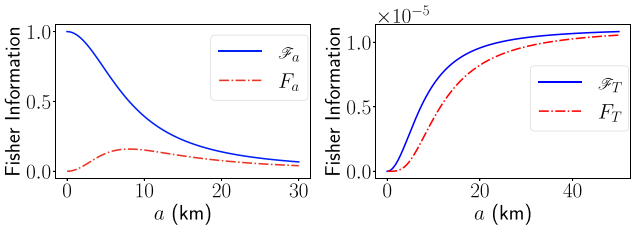

FIG. 2. (a) The QFI (solid blue line) and the CFI (dotted-dashed red line) from the heterodyne measurement to estimate the source size as a function of a. Both results are dimensionless and scaled with the $4\pi T\kappa/R^2$, considering $T = 300$ K. (b) The QFI (solid blue line) and the CFI (dotted-dashed red line) from the heterodyne measurement to estimate the temperature as a function of a. Both results are in units of $1/\mathrm{K}^2$, and we consider $T = 300$ K.

deviation of about 4 km. Thus, we can conclude that the photon-number measurement on the complete basis of Fock states in the detection mode $\hat{b}$ helps us to get better resolution than heterodyne measurement. If a becomes larger, we can see that the QFI and CFI get close to each other at some point. To estimate a, we assumed that we know exactly the temperature of the source. Further, we find the QFI for estimating the temperature as

$$\mathscr{F}_T = \frac{\pi a^2 \kappa}{R^2 T + a^2 \pi T^2 \kappa}, \tag{51}$$

with a SLD given by

$$\mathscr{L}_T = \frac{R^2}{TR^2 + a^2 \pi T^2 \kappa} \hat{b}^\dagger \hat{b}. \tag{52}$$

The optimal POVM is a set of projectors in the Fock basis $\{|m\rangle\langle m|\}_{\{m\}}$ for both estimating a and T. The CFI from heterodyne detection to estimate temperature becomes

$$F_T = \frac{\pi^2 a^4 \kappa^2}{(R^2 + a^2 \pi T \kappa)^2}. \tag{53}$$

In Fig. 2(b), we plot both QFI and CFI for heterodyne detection for temperature estimation. Both have very close functional behavior. They vanish for $a \to 0$ and they approach each other when we have a large source size.

The off-diagonal matrix element of the QFI matrix for multiparameter estimation reads as

$$\mathscr{F}_{aT} = \frac{2a\pi\kappa}{R^2 + a^2 \pi T \kappa}. \tag{54}$$

By sampling the same state $\mathcal{N}$ times, the standard deviation of the estimator decreases proportional to $1/\sqrt{\mathcal{N}}$. The SMOS satellite moves at a constant speed $v \simeq 7$ km/s and takes the time $\tau = L/v$ to fly over a distance L. For each sample there is a lower bound for the detection time given by $t_D \sim 1/B$ (see Appendix A). In practice, the effective detection time might be much larger, due to, e.g. dead times of the detectors, slow electronics, etc. In addition, zero temperature of the detector and modes b_i is implicitly assumed in our calculations, but would require cooling down to temperatures much smaller than $\hbar\omega_0$. If the actual detection time is t_D^{eff}, the sample size becomes $\mathcal{N} = \tau/t_D^{\mathrm{eff}}$. In this paper we intend to establish the ultimate theoretical bounds and hence assume that the minimal detection time $t_D = 1/B$ can be achieved, in which case the sample size becomes $\mathcal{N} \sim LB/v$. To estimate the source size one can assume that $L \sim a$, and the QCRB for estimating a becomes $\delta a \geqslant 1/\sqrt{\mathcal{N}\mathcal{F}_a}$. Since $\mathcal{N}$ depends also on a one can find the optimum bound in the sense of a minimal δa at $a = R/\sqrt{\pi\kappa T}$. For $T = 300$ K, we find $a \sim 7.9$ km and $\delta a \gtrsim 1.0$ m. The bound for estimating T, assuming all other parameters known, can be written as $\delta T \geqslant 1/\sqrt{\mathcal{N}\mathcal{F}_T}$. Using the same parameters as before and the same sample size, we have $\delta T \gtrsim 0.08$ K. Thus, increasing the sample size to the theoretically maximally possible value, the spatial resolution improves by a factor of order 35 000 compared to the resolution of SMOS, and the radiometric resolution by factor of order 500. One can also increase the resolution by increasing the number of antennas, which we present in the following sections.

B. Two-mode interferometer

The optimum measurement with a two-mode interferometer for temperature estimation of a black body was considered in Ref. [80] and experimentally demonstrated in Ref. [81]. Further, the spatial resolution of two equally bright point sources with a similar setup was recently studied in Ref. [35]. In the previous section, we only considered a single receiver with mode $\hat{b}$. It is obvious that we may get additional information from the cross correlations of an n-mode interferometer. An analytical calculation of the QFI matrix for n-mode interferometer generally becomes untractable for $n > 2$ and one has to rely on numerical calculation (see Sec. III C). In this section, we consider two receivers with modes $\hat{b}_1$ and $\hat{b}_2$ to analyze the estimation of a single uniform circular disk for its size a and temperature T and two uniform circular disks with different temperatures for their the spatial resolution (source separation s_i and centroid t_i with $i \in \{x, y\}$). We write $\mathbf{b}$ as $\mathbf{b}^\top = (\hat{b}_1, \hat{b}_1^\dagger, \hat{b}_2, \hat{b}_2^\dagger)$. Since, the mean displacement is $\Gamma_i = 0$, the covariance matrix Σ of the state ρ_{int} becomes

$$\Sigma = \begin{bmatrix} 0 & \chi & 0 & \xi \\ \chi & 0 & \xi^* & 0 \\ 0 & \xi^* & 0 & \chi \\ \xi & 0 & \chi & 0 \end{bmatrix}, \tag{55}$$

where $\chi = 1/2 + \bar{n}$ and $\xi = \langle \hat{b}_2^\dagger \hat{b}_1 \rangle$. We give the general result for the QFI elements in Appendix C. Further, one can write the matrix $\mathbf{M}_i$ as

$$\mathbf{M}_i = \begin{bmatrix} g_i^1 & |g_i^2| e^{i\delta_i} \\ |g_i^2| e^{-i\delta_i} & g_i^1 \end{bmatrix}, \tag{56}$$

where g_i^1, g_i^2 are given in Appendix C in terms of χ and ξ, and δ_i is the phase difference between two modes in the SLD. Using the eigenvectors of $\mathbf{M}_i$, we can write the unitary $\mathbf{V}_i$ as

$$\mathbf{V}_i = \frac{1}{\sqrt{2}} \begin{bmatrix} 1 & e^{i\delta_i} \\ 1 & -e^{i\delta_i} \end{bmatrix}. \tag{57}$$

We see that $\mathbf{V}_i$ does not depend on the magnitude of the elements of the matrix $\mathbf{M}_i$ for a two-mode interferometer. The detection modes can be found as $\hat{d}_1 = (\hat{b}_1 + \hat{b}_2 e^{i\delta_i})/\sqrt{2}$ and $\hat{d}_2 = (\hat{b}_1 - \hat{b}_2 e^{i\delta_i})/\sqrt{2}$. The preprocessing to combine these two modes can be done by a phase delay on one of the modes

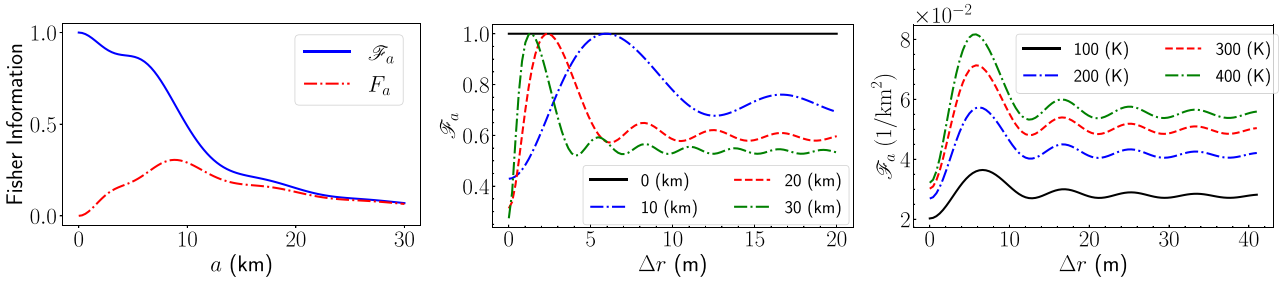

FIG. 3. (a) The QFI (solid blue) and the CFI (dotted-dashed red) from the heterodyne measurement to estimate the source size as a function of a. Both of the results are scaled with Eq. (59). In the limit $a \to 0$, for $T = 300$ K we have $\mathscr{F}_a \sim 0.117$ 1/km^2, which gives us a standard deviation around 2.92 km. (b) The QFI $\mathscr{F}_a$ for estimating the size of the circular disk as a function of Δr (spatial separation of two receivers) for different source sizes $a = (0, 10, 20, 30)$ km with $T = 300$ K. Data are scaled by the maximum values of the QFI, which are $\sim 0.117, \sim 0.070, \sim 0.030, \sim 0.015$ 1/km^2, respectively. (c) The QFI $\mathscr{F}_a$ for estimating the size of the circular disk as a function of separation of two antennas Δr, for different temperatures T.

and then combining these modes by a beam splitter before any measurement. Then the POVM for the optimum measurement can be written as a set of projectors again in Fock basis as $\{|m_1, m_2\rangle \langle m_1, m_2|\}_{\{m_1,m_2\}}$ which is the eigenbasis of $\hat{d}_l^\dagger \hat{d}_l$, $\hat{d}_l^\dagger \hat{d}_l |m_1, m_2\rangle = m_l |m_1, m_2\rangle$. We check the weak compatibility condition for the SLD operators for general ith and jth parameters of two-mode interferometer in Appendix B. We find that the SLD operators commute on average on ρ_{int}, $\text{Tr}[\rho_{\text{int}}[\mathscr{L}_i, \mathscr{L}_j]] = 0$ for the two-mode interferometer. In this case, $C^H(\boldsymbol{\mu}, \boldsymbol{W}) = C^S(\boldsymbol{\mu}, \boldsymbol{W})\ \forall\ \boldsymbol{W}$ and the SLD-CRB can be saturated asymptotically by a collective measurement on an asymptotically large set of copies $\rho_{\text{int}}^{\otimes \mathcal{N}}$ of ρ_{int}. To compare this POVM with the classical approach, we consider heterodyne detection (see Appendix D).

Resolution of uniform circular source. Let us assume that on the source plane, we have a circular disk of radius a with uniform temperature T located at $\mathbf{r} = (x_0, y_0, R)$. Then the temperature distribution over the surface on the source plane can be written as $T_{\text{eff}}(x, y) = T\ \text{circ}(x - x_0, y - y_0)$. We want to estimate again a and T. The QFI for estimating the source size is given by Eq. (E4) for a two-mode interferometer. The expression is quite complicated. However, we can analyze it numerically, or we can look at certain limits. Estimating the size of the circle $\mathscr{F}_a$ depends on Δr (the separation of the two antennas). Physically we assumed this separation to be greater than the central wavelength $\Delta r > \lambda$. Mathematically, one can take the limit $\Delta r \to 0$, in which case the additional information from the phase difference between two antennas vanishes. In this limit, the QFI for estimating the source size becomes

$$\mathscr{F}_a \xrightarrow{\Delta r \to 0} \frac{8\pi\kappa T}{R^2 + 2\pi a^2 \kappa T}. \tag{58}$$

If we have $2\pi a^2 \kappa T \gg R^2$, the QFI for estimating a is $\mathscr{F}_a \sim 4/a^2$; for high temperatures or large a, the error of estimating the size of the source linearly increases with its size. Figure 3(b) shows how the QFI changes when we decrease the source size. In the limit of $a \to 0$, the QFI for estimating the source size becomes

$$\mathscr{F}_a \xrightarrow{a \to 0} \frac{8\pi\kappa T}{R^2}. \tag{59}$$

Comparing with the single receiver the QFI is doubled for two-mode interferometers in the limit $a \to 0$. We can still have nonvanishing QFI for $a \to 0$, as we can see from the black line in Fig. 3(b), which is the limit as in Eq. (59). The black line ($\sim$0 km source size) is scaled with ~ 0.117 1/km^2, which corresponds to a standard deviation of $\sim$2.92 km for the interferometer with two modes. We give the CFI for heterodyne detection in Eq. (E14). For small source size, we can ignore the higher-order terms in a, and we can simplify it as

$$F_a \approx \frac{16\pi^2 \kappa^2 T^2 a^2}{R^4}. \tag{60}$$

As we can see, for $a \to 0$, the CFI for heterodyne detection tends to zero. Thus, the resolution of the source size with heterodyne detection becomes arbitrarily bad in that limit [see Fig. 3(a)]. However, for large source sizes, we can see from Fig. 3(a) that CFI and QFI become equivalent. Therefore, constructing a POVM from the SLD can beat Rayleigh's resolution curse, even for estimating the source size. To construct the POVM for estimating the source size we give the elements of matrix $\mathbf{M}$ in Eqs. (E9) and (E10). The phase delay is found as $\delta_a = x_0 v_x + y_0 v_y$, with v_i defined as $v_x = \Delta r \cos\varphi/(\lambda R)$, $v_y = \Delta r \sin\varphi/(\lambda R)$. Thus, once we have the information of the location of the source centroid, we can combine these two interferometer modes by using a phase delay to get the POVM that saturates the QCRB. We plot the QFI as a function of Δr in Fig. 3(c) for different temperatures. We can see that when the effective temperature of the circular source increases, the QFI also increases. Moreover, when we increase Δr, the QFI for estimating a increases up to a maximum around $\Delta r \sim 6$ m. The reason for this is additional information coming from the phase differences in the two antennas. The QFI in Eq. (59) is doubled compared to QFI for single receiver in Eq. (48) in the limit $a \to 0$.

In the limit $\Delta r \to 0$, the QFI for estimating T becomes

$$\mathscr{F}_T \to \frac{2\pi a^2 \kappa}{T(2\pi a^2 \kappa T + R^2)}. \tag{61}$$

Since we assume we are in a microwave regime $k_B T \gg \hbar\omega_0$, we can not take the limit $T \to 0$. Instead, we can verify that the QFI for estimating the temperature depends on the source

size for a finite temperature. Now, for $T = 300$ K and 30 km source size we have the QFI around 2×10^{-5} $1/\mathrm{K}^2$ which gives a very high standard deviation around 221 K. We show in the next section that the QFI also increases if we increase the number of spatial modes. For instance, for 20 antennas, we have QFI around 1.5×10^{-4} $1/\mathrm{K}^2$, and the standard deviation is 79 K for a single measurement.

In the limit $\Delta r \to 0$, the CFI from heterodyne detection becomes

$$F_T \to \frac{4\pi^2 a^4 \kappa^2 (\pi a^2 \kappa T + R^2)(3\pi a^2 \kappa T + R^2)}{(2\pi a^2 \kappa T + R^2)^4}. \tag{62}$$

To compare with the QFI we assume the brightness temperature $T = 300$ K and source size $a = 30$ km. This gives a CFI around 8×10^{-6} $1/\mathrm{K}^2$ which give us a standard deviation around 350 K. Compared to the QFI information, the CFI is around 2.5 times smaller. Therefore, combining the spatial modes (receivers) and measuring photon number in the Fock basis of $\hat{d}_1, \hat{d}_2$, as expected, is more advantageous even for estimating the temperature.

So far, we only gave the diagonal elements of the QFI matrix, relevant for estimating each parameter individually, assuming all other parameters are known. The single independent off-diagonal element of the QFI matrix regarding a and T is given in Eq. (E7). In the limit $\Delta r \to 0$ it simplifies to

$$\mathscr{F}_{aT} = \frac{4\pi a \kappa}{2\pi a^2 \kappa T + R^2}. \tag{63}$$

Then one can construct the QFI matrix to find the QCRB for multiparameter estimation. Further, we can estimate the source location considering the two parameters x_0, y_0. The QFI matrix elements for estimating the source locations can be written as

$$\mathscr{F}_{i_0 j_0} = \frac{8\pi^2 \Delta r^2 \kappa T J_1^2 v_i v_j}{\pi \Delta r^2 (\pi a^2 \kappa T + R^2) - \kappa \lambda^2 R^2 T J_1^2}, \tag{64}$$

where $i, j \in \{x, y\}$. The QFI for estimating the source location depends on source size and source temperature. Since the elements $\mathscr{F}_{i_0 a}$ and $\mathscr{F}_{i_0 T}$ of the QFI matrix are zero, source size and location can be estimated simultaneously. And the necessary phase delay for POVM can be found as $\delta_{i_0} = \delta + \pi/2$ from Eq. (E13).

Spatial resolution of two-point sources. Recently, the spatial resolution of two equally bright strong point sources was studied in [35] by considering the sources aligned parallel to the two-mode interferometer.

In this section, we consider a similar model with two circular disk sources on the surface of the source plane at locations $\mathbf{r}_1 = (x_1, y_1, R)$ and $\mathbf{r_2} = (x_2, y_2, R)$ but with different effective temperatures T_1 and T_2, and same sizes a. We assume that in the far field $\{x_i, y_i\} \ll R$ and $a \ll R$. We analyze two cases: when the sources are aligned or not aligned with the two antennas. For two circular sources with equal size, the temperature distribution over the surface can be written as

$$T_{\mathrm{eff}}(x, y) = \sum_{i=\{1,2\}} T_i \mathrm{circ}(x - x_i, y - y_i). \tag{65}$$

Then we can define the four parameters that we want to estimate as source separation $(s_x = x_1 - x_2)$, $(s_y = y_1 - y_2)$ and centroid of the two sources $[t_x = (x_1 + x_2)/2]$, $[t_y = (y_1 + y_2)/2]$. In Appendix F, we express the QFI matrix elements for all four parameters. Since these equations are quite complicated, we check the important limits. Since we want to resolve the two-point sources even for very small separation, we check the limit $s_x, s_y \to 0$. Then we have QFI matrix elements for estimating the source separation as $\mathscr{F}_{s_i} \to 4\pi^2 v_i^2 \eta \kappa T$ and $\mathscr{F}_{s_x s_y} \to 4\pi^2 v_x v_y \eta \kappa T$, if $T_1 = T_2 = T$.

If we assume two sources aligned parallel to the two-mode interferometer [$y_1 = 0, y_2 = 0$ and $\varphi = 0 \to v = v_x = \Delta r/(R\lambda)$ and $s_x \to s, \quad t_x \to t$] we can simplify our problem to a single dimension. We show the dependence of the QFI matrix elements on average temperature $[T = (T_1 + T_2)/2]$ and temperature difference $\Delta T = T_1 - T_2$ assuming $T_1 \geqslant T_2$. In Fig. 4(a), we plot $\mathscr{F}_s$ with respect to source separation s for different average temperatures. As expected, when the temperature increases, the QFI for estimating the separation also increases. For $T = 300$ K and $\Delta r = 4$ m, we have a QFI around 0.027 $1/\mathrm{km}^2$ which corresponds to a standard deviation of 6 km for only two receivers for the separation estimation. In Fig. 4(b), we see that, as we increase the temperature difference between the two-point sources, the QFI becomes less oscillatory and at $\Delta T \to 2T$, the oscillatory behavior disappears. In the limit $\Delta T \to 2T$, or $s \to 0$ the QFI for estimating s becomes

$$\mathscr{F}_s \to 4\pi^2 v^2 \eta \kappa T, \tag{66}$$

which is the limit given by the solid black line in Fig. 4(b). We calculated the CFI from heterodyne detection to estimate the source separation in Eq. (F14). If the size of the sources is very small and in the limit $\eta \kappa T \ll 1$ the CFI for estimating the source separation simplifies to

$$F_{s_i} \xrightarrow{\eta \kappa T \ll 1} 8\pi^2 \eta^2 \kappa^2 T^2 v_i^2 \sin^2[\pi (s_x v_x + s_y v_y)]. \tag{67}$$

When the source separation goes to zero $(s_x, s_y \to 0)$, F_{s_i} tends to zero. We compare the QFI with CFI in Eq. (F14) from heterodyne detection in Fig. 4(c). As we can see, the CFI goes to zero for small source separation. Therefore, we can conclude that Rayleigh's curse limits heterodyne detection. The POVM from the SLD eliminates that limitation. We give the elements of the matrix $\mathbf{M}_s$, g_s^1, and g_s^2 in Appendix F. The phase difference for combining two spatial modes of the interferometer can be found as $\delta_s = 2\pi (t_x v_x + t_y v_y) - \pi$. Assuming the alignment of the spatial mode separation parallel to source separation, it becomes $\delta_s = 2\pi t v - \pi$.

The QFI matrix elements for estimating the centroid is given in Eq. (F6). We assume that the two sources aligned again parallel to two spatial modes of the interferometer [$y_1 = 0, \ y_2 = 0$ and $\varphi = 0 \to v = v_x = \Delta r/(R\lambda)$ and $s_x \to s, \quad t_x \to t$] and $\mathscr{F}_{t_x, t_x} \to \mathscr{F}_t$. In Fig. 4(d), we see that the $\mathscr{F}_t$ increases when we increase the temperature. For $T = 300$ K and $\Delta r = 4$ m, we have a QFI $\mathscr{F}_t \sim 0.11$ $1/\mathrm{km}^2$ which corresponds to a standard deviation of 3 km for estimating the centroid. When $sv \sim 0.5$, $\mathscr{F}_t$ goes to zero for equally bright sources. In Fig. 4(e) we see that it is not zero for $sv \sim 0.5$, if $\Delta T \neq 0$, and the oscillation of $\mathscr{F}_t$ decreases when we increase the temperature difference. In the limit $s \to 0$, $\mathscr{F}_t$ simplifies to

$$\mathscr{F}_t \to 32\pi^2 v^2 \eta \kappa T \tag{68}$$

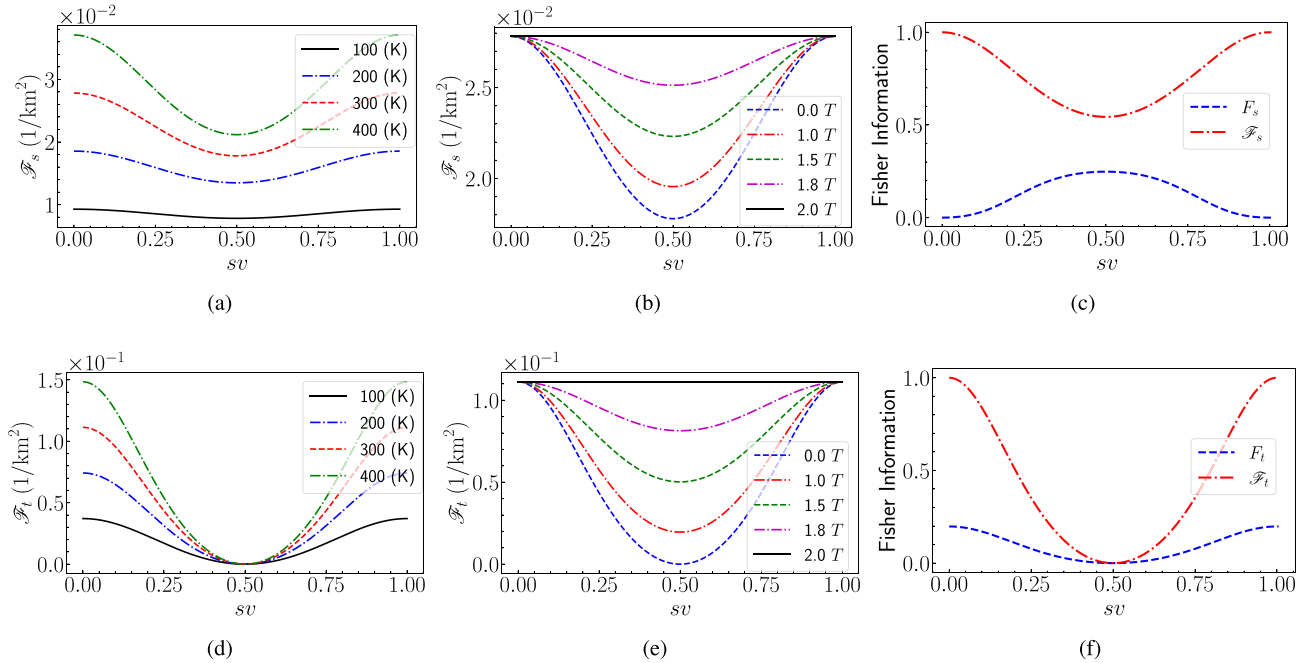

FIG. 4. (a) The QFI $\mathscr{F}_s$ of estimating the separation of two-point sources as a function of source separation s for different average temperatures with $\Delta T = 0$ and $\Delta r = 4$ m. (b) The QFI $\mathscr{F}_s$ with respect to s for various temperature differences ΔT for $T = 300$ K. (c) The QFI $\mathscr{F}_s$ (red dotted-dashed) and CFI for heterodyne detection (blue dashed) for estimating the separation of two-point sources with same temperatures T as a function of s. Both the QFI and the CFI scaled by $4\pi^2 v^2 \eta\kappa T$. (d) The QFI $\mathscr{F}_t$ respect to s for different average temperature T. (e) The QFI $\mathscr{F}_t$ respect to s for various temperature difference ΔT for $T = 300$ K. (f) The QFI $\mathscr{F}_t$ (red dotted-dashed) and CFI for heterodyne detection F_t (blue dashed) for estimating the centroid of two-point sources with same temperatures T as a function of s (both the QFI and the CFI scaled by $32\pi^2 v^2 \eta\kappa T$). For (a), (b), (d), and (e), v is fixed by taking the separation Δr of the two antennas 4 m and we have $\eta \sim 10^{-4}$. The curves are ordered by increasing value of the QFI from solid black to green dotted-dashed lines in (a) and (d), and from blue dashed to solid black lines in (b) and (d).

for $\Delta T = 0$. The CFI for heterodyne detection is given in Eq. (F13). For small sources we consider again the limit $\eta\kappa T \ll 1$, and we ignore the higher-order terms of $\eta\kappa T$. Then we have

$$F_{t_i} \xrightarrow{\eta\kappa T \ll 1} 32\pi^2\eta^2\kappa^2 T^2 v_i^2 \cos^2[\pi(s_x v_x + s_x v_y)]. \tag{69}$$

If the source separation goes to zero ($s_x, s_y \to 0$), we still have a finite F_{t_i}, unlike the CFI for source separation. In Fig. 4(f), we compare $\mathscr{F}_t$ with F_{t_i}. When the source separation goes to zero, both Fisher information goes to a constant, and both go to zero at $sv \to 0.5$. However, the QFI is five times larger than the CFI from heterodyne detection. Again the phase difference for the POVM from the SLD can be found as $\delta_t = 2\pi t v + \pi/2$.

Both QFIs, for source separation and centroid, are periodic functions with a period of $1/v$ in the case of two point sources (see Ref. [35]). The information on the position of the sources is only encoded in phases. The QFIs are maximum at $s = 0$ or at $s = 1/v = \lambda R/\Delta r$. The fact that $sv = \frac{1}{2}$ the QFI has a minimum (or even vanishes for the centroid estimation) has its origin in destructive interference. For this value of sv, the two waves from the centroid position to the two receivers have a phase difference of π that makes that the off-diagonal matrix element in the correlation matrix $\langle \hat{b}_i^\dagger \hat{b}_j \rangle$ vanish. Hence, the QFI has to drop from the finite value at $sv = 0$ to this minimum.

C. 1D *n*-mode interferometer arrays

The previous section considered a two-mode interferometer for analytical calculations and compared the QFI with its POVM and CFI for heterodyne detection. To compare our results with SMOS, we extend the two-mode interferometer to a 1D array of n single-mode receivers. We investigate numerically how the QFI changes when increasing the number n of interferometer modes. We assume the antenna array aligned with the x axis on the detection plane and denote the maximum baseline separation of the two most distant antennas by $\Delta r_{\max}$.

Resolution of two-point sources for n-mode interferometer array. We assume that both sources have the same sizes and temperatures ($\Delta T = 0$ and $T_1 = T_2 = T$) and that they are parallel to the antenna array. In Fig. 5(a), we see that when we increase the number of receivers, the behavior of $\mathcal{F}_s$ changes. It is still oscillatory as a function of sv with a period of 2π. However, for each oscillation, we have $n - 2$ additional maxima. Moreover, in Fig. 5(b), we see that $\mathcal{F}_s$ increases gradually when we increase the number of receivers and the maximum baseline increases as $\Delta r_{\max} = (n-1)\Delta r$. For $\Delta r = 1$ m and $T = 300$ K, the standard deviation for estimating the source separation is ∼23 km for the two-mode interferometer. For the 20-mode interferometer, we find a standard deviation of around 0.65 km. Further, if we keep the baseline fixed as 4 m, the QFI increases linearly with the number of receivers, as we

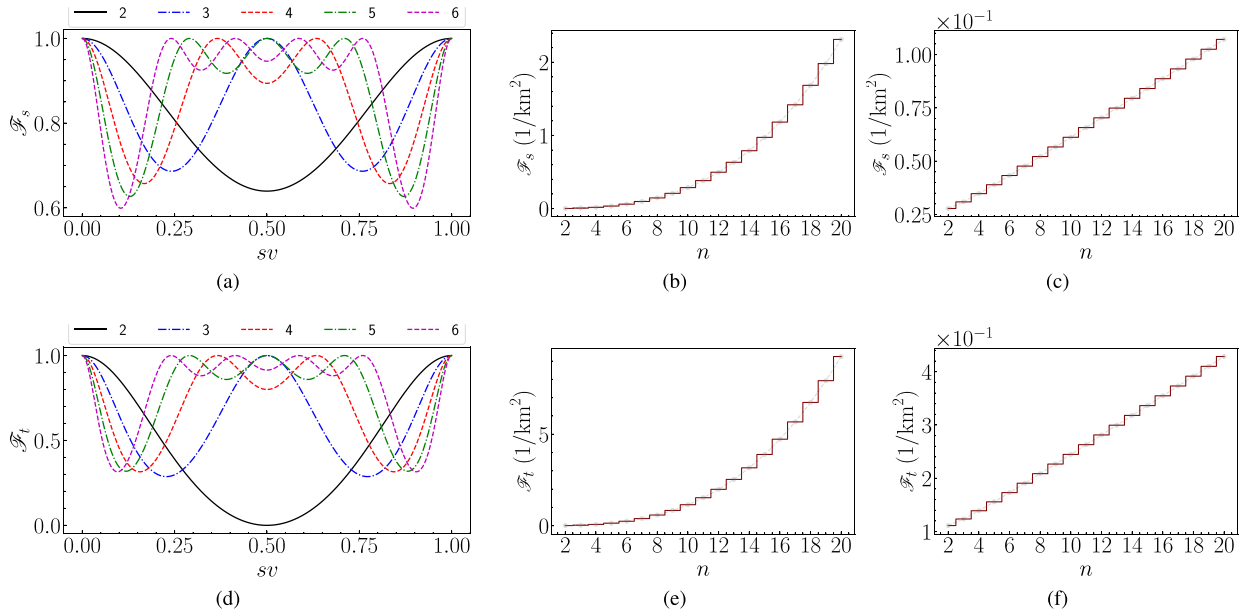

FIG. 5. (a) The QFI $\mathscr{F}_s$ as a function of s for 2,3,4,5,6 mode interferometers and each curve is scaled by its maximum values which are $\sim 1.7 \times 10^{-3}, \sim 6.9 \times 10^{-3}, \sim 17.3 \times 10^{-3}, \sim 34.7 \times 10^{-3}, \sim 60.8 \times 10^{-3}$ 1/km^2, respectively. (b) The QFI $\mathscr{F}_s$ with respect to a number of interferometer modes n. (c) The QFI $\mathscr{F}_s$ with respect to a number of interferometer modes n. (d) The QFI $\mathscr{F}_t$ as a function of s for 2,3,4,5,6 mode interferometers. Each curve is scaled by its maximum values which are $\sim 0.67 \times 10^{-2}, \sim 2.78 \times 10^{-2}, \sim 6.96 \times 10^{-2}, \sim 13.9 \times 10^{-2}, \sim 24.3 \times 10^{-2}$ 1/km^2, respectively. (e) The QFI $\mathscr{F}_t$ with respect to a number of interferometer modes n. [For all, the separation of two nearest antenna Δr is 1 m, and $\eta \sim 10^{-4}$. The maximum baseline is $\Delta r_{\max} = (n-1)\Delta r$.)] (f) The QFI $\mathscr{F}_t$ with respect to a number of interferometer modes n. For both (c) and (f), the maximum baseline is fixed by $\Delta r_{\max} = 4$ m, in this case, separation of two nearest antenna is $\Delta r = \Delta r_{\max}/(n-1)$, and $\eta \sim 10^{-4}$. The curves are ordered by increasing value of the modes (n) from two-mode interferometer (solid black) to six-mode interferometer (purple dotted-dashed) in (a) and (d).

can see in Fig. 5(c). In this case, for a two-mode interferometer, we have a standard deviation of around 6 km, and for a 20-mode interferometer, we have 3 km.

We also checked the centroid estimation for the n-mode interferometer. It leads to similar results as for source separation. From Fig. 5(d) we see that for $sv = 0.5$ the centroid uncertainty for the two-mode interferometer diverges ($\mathscr{F}_t \sim 0$ at $sv \sim 0.5$). This is no longer the case for the array of n receivers. In Fig. 5(e), we see that $\mathscr{F}_t$ also increases with the number of modes. For the two modes, the standard deviation for estimating the centroid was $\sim$12 km. For the 20 modes, we have a standard deviation of around 0.32 km considering $\Delta r = 1$ m and $\Delta r_{\max} = (n-1)\Delta r$ for average temperature $T = 300$ K. If we keep the baseline fixed, as we can see from the Fig. 5(f), $\mathscr{F}_t$ increases linearly by n. By fixing the $\Delta r_{\max} = 4$ m, we have a standard deviation of $\sim$3 km for the two-mode interferometer; for 20 modes we have a standard deviation of $\sim$1.5 km. Thus, instead of sampling the state in time, we can increase the number of receivers to increase the QFI, and both methods can be combined as well.

Spatial resolution of single circular source for n-mode interferometer array. To analyze the effect of n for source size estimation, we consider a single circular source as given in Eq. (46). In Fig. 6, we show how the QFI for estimating a changes with n. For $a \to 0$, $\mathscr{F}_a$ increases linearly with n. We have $\mathscr{F}_a \sim 6.16 \times 10^{-2}$ 1/km^2 for single receiver which corresponds to a standard deviation of 4 km and for higher n, we have approximately $\mathscr{F}_a \propto n$ for small values of a. If we have an array of 20 antennas, $\mathscr{F}_a \sim 1.23$ 1/km^2 which gives a standard deviation of 0.9 km for estimating a. When we increase the source size a, we see that there is extra information coming from the phase differences as given by the solid lines for $\Delta r_{\max} = 6$ m and dashed lines for $\Delta r_{\max} = 4$ m. One can also see that as expected the dotted lines, corresponding to the limit $\Delta r_{\max} \to 0$, get close to the solid black line, which corresponds to a single receiver, for large values of a.

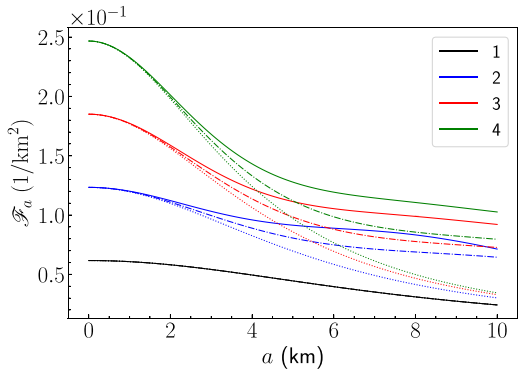

FIG. 6. The QFI $\mathscr{F}_a$ as a function of a for 1,2,3,4 mode interferometers, which are given by black (the lowest single) curve, blue, red, and green (the top) curves, respectively. The maximum baseline difference is given by $\Delta r_{\max} \to 0$ for dotted lines, $\Delta r_{\max} = 4$ m for dashed lines, and $\Delta r_{\max} = 6$ m for solid lines. The black solid line corresponds to single receiver and $T = 300$ K.

As a mathematical limit, we can take $\Delta r_{\max} \to 0$. Then the additional information from phase differences of a receiver pair will vanish [see Figs. 2(a) and 3(a)]. One can also compare the QFI in Eq. (48) for a single mode with the QFI in Eq. (59) for a two-mode receiver. In the limit $a \to 0$, we see that the QFI for estimating a is doubled. Yet, the FI for estimating a from heterodyne detection in Eqs. (50) and (60) always vanishes in this limit $a \to 0$. In Fig. 6, the QFI to estimate a linearly increases with n. But the FI from heterodyne detection is zero for the small source sizes in the limit $a \to 0$ even for $n \to \infty$. Thus, we see that resolution is limited for heterodyne detection for small source sizes. To get the quantum super-resolution for estimating the image, one needs to linearly combine the modes $\hat{b}_i$ of the n-mode interferometer. For that aim, one needs to calculate the elements of the matrix $\mathbf{M}_i$ numerically. Each normalized eigenvector of $\mathbf{M}_i$ maps to a set of operators $\bar{\mathbf{d}}$ by linear combination of the operators in $\bar{\mathbf{b}}$ with corresponding weights and phases. One can design a setup using these weights and phases in the eigenvectors to achieve the resolutions for a chosen parameter given in this section.

IV. CONCLUSION

In summary, we studied possible quantum advantages in passive microwave remote sensing. Starting from a microscopic current density distribution in the source plane corresponding to a position-dependent brightness temperature $T_{\text{eff}}(x, y)$, we derived the general partially coherent state received by an array of antennas. From the dependence of that partially coherent states on parameters that characterize the sources, such as the radius a and brightness temperature T of a uniform circular source, we obtained the QFI and hence the QCRB for the smallest possible uncertainty with which these parameters can be estimated based on measurements of the multimode state of the antennas. We showed how the optimal measurements allowing one to estimate a single parameter can be obtained for a general array interferometer with antennas placed at arbitrary positions. In general, the optimal measurements correspond to photon-detection in certain detector modes that can be obtained from the original receiver modes by mode mixing via beam splitters and phase shifters. For single-mode and two-mode interferometers, we gave explicit analytical results for the best possible resolution of one or two uniform circular sources, both in a and T and demonstrated a clear quantum advantage over the classical strategy corresponding to direct heterodyne measurements of the receiver modes. In the limit of small source sizes, we recover known results for the measurement of the centroid and separation of two-point sources. We benchmarked our results with the performance of the SMOS mission, which achieves about 35-km resolution with 69 antennas deployed on three 4-m long arms arranged in a Y shape, operating at 21 cm the wavelength, and flying at a height of 758 km above Earth. As an example, we showed that by using the optimal measurements, a single arm of length 4 m with 20 antennas and a single measurement would allow a spatial resolution of about 1.5 km. With a smaller satellite, a more than 20-fold increase of resolution compared to SMOS could be achieved. By increasing the size of the array to 19 m, the 20 antennas should give rise to a spatial resolution down to 300 m. Substantially better resolutions can be achieved if we allow more measurements. If we assume that the number of samples is given by the time the satellite flies over the object whose size one wants to estimate divided by the inverse bandwidth, even with a single receiver a spatial resolution down to a few meters and a radiometric resolution of a fraction of a Kelvin become possible in principle.

Our results generalize previous approaches to quantum-enhanced imaging based typically on weak sources (photon numbers on average smaller than 1 per mode) or point sources, and pave the way to quantum metrological sensitivity enhancements in real-world scenarios in passive microwave remote sensing. Several challenges remain. Experimentally, single-photon detection in the microwave regime is still difficult but starts to become available [82], and even number-resolved photon detection in the microwave regime has meanwhile been demonstrated [83]. It requires very low temperatures for operating superconducting qubits that would have to be maintained on a long timescale on the satellite. From the theoretical side, an extension to a many-parameter regime requiring adaption of the optimal measurements will be crucial for true imaging. Post-measurement beam synthesis that is common in interferometric astronomy does not work here, as already the detection modes depend on the pixel in the image that one wants to focus on. Nevertheless, the substantial quantum advantages demonstrated here theoretically in a relatively simple but real-world scenario give hope that quantum metrology can help to significantly improve the resolution of passive Earth observation schemes, with corresponding positive impact on the data available for feeding climate models, weather forecasts, and forecasts of floodings.

ACKNOWLEDGMENTS

D.B. and E.K. are grateful for support by the DFG, Project No. BR 5221/3-1. D.B. thanks Y. Kerr, B. Rougé, and the entire SMOS team in Toulouse for valuable insights into that mission.

APPENDIX A: BRIGHTNESS TEMPERATURE AND CURRENT DENSITY FLUCTUATIONS

The number of photons that pass through a certain antenna area A_D in a certain time t_D can be found from $\bar{n} = A_D t_D \Phi$, where Φ is the photon flux. For a given intensity I, the photon flux for frequency ω_0 can be found by $\Phi = I/(\hbar\omega_0)$. If the total energy density on the antenna is U_D, then the intensity can be written as $I = U_D c$. Then $\bar{n}$ becomes $\bar{n} = A_D t_D U_D c/(\hbar\omega_0)$. In the microwave regime $\hbar\omega \ll k_B T$, the energy density (energy per unit volume per frequency) from black-body radiation at

frequency ω with a temperature distribution $T(x,y)$ on the surface of radiation at the ith antenna position is given by [43]

$$u_D(\omega) = \frac{k_B}{2\pi^3 c^3}\int dx\,dy\,\omega^2\frac{T_B(x,y)\cos\tilde{\theta}(x,y)}{|\mathbf{r}-\mathbf{r}_i|^2}, \tag{A1}$$

where the brightness temperature is defined as $T_B(x,y)\equiv T(x,y)B(x,y;\omega,\tilde{\theta},\tilde{\varphi})$. Earth is rather a gray than a black body, therefore, the emissivity $B(x,y;\omega,\tilde{\theta},\tilde{\varphi})$ of the patch in the direction of the satellite given by polar and azimuthal angles is introduced. One can take the integral over ω using the filter function in Eq. (21) to find the total energy density (energy per volume) and it becomes

$$U_D = \frac{k_B\omega_0^2 B}{2\pi^3 c^3}\int dx\,dy\frac{T_B(x,y)\cos\tilde{\theta}(x,y)}{|\mathbf{r}-\mathbf{r}_i|^2}. \tag{A2}$$

Then the photon number on the receiver becomes

$$\bar{n} = \frac{2k_B}{\pi\hbar\omega_0}\left(\frac{A_D}{\lambda^2}\right)(t_D B)\int dx\,dy\frac{T_B(x,y)\cos\tilde{\theta}(x,y)}{|\mathbf{r}-\mathbf{r}_i|^2}. \tag{A3}$$

For simplicity of the receivers scattering function, we set $A_D\sim\lambda^2$ and $t_D\sim 1/B$. Comparing Eq. (A3) with (29), we define $\langle|\tilde{j}_{t,i}(\mathbf{r},\omega)|^2\rangle \equiv K_1 T_B(x,y)\cos\tilde{\theta}(x,y)\delta(z-R)$ with a constant $K_1 = 32\tau_c k_B/(3l_c^3\mu_0 c)$ which agrees with the result in Ref. [43].

APPENDIX B: COMMUTATION RELATIONS OF SLD'S FOR n-MODE INTERFEROMETER

The SLD for the ith parameter is given in Eq. (38) for the n-mode interferometer. To find the $[\mathscr{L}_i,\mathscr{L}_j]$ we write

$$\mathscr{A}_i = \sum_j^n g_i^j\hat{b}_j^\dagger\hat{b}_j, \quad \mathscr{B}_i = \sum_{j<k}^n\left[g_i^{jk}\hat{b}_j^\dagger\hat{b}_k + \left(g_i^{jk}\right)^*\hat{b}_k^\dagger\hat{b}_j\right]. \tag{B1}$$

Using $[\hat{b}_l,\hat{b}_k^\dagger]=\delta_{kl}$, one can write $\hat{b}_k^\dagger\hat{b}_l\hat{b}_m^\dagger\hat{b}_p = \hat{b}_m^\dagger\hat{b}_p\hat{b}_k^\dagger\hat{b}_l + \hat{b}_k^\dagger\hat{b}_p\delta_{lm} - \hat{b}_m^\dagger\hat{b}_l\delta_{kp}$. Then, we find the rest of the commutation relations as follows:

$$[\mathscr{A}_i,\mathscr{A}_j] = \sum_{kl}^n g_i^k g_j^l(\hat{b}_l^\dagger\hat{b}_k\delta_{kl} - \hat{b}_k^\dagger\hat{b}_l\delta_{kl}) = 0, \tag{B2}$$

$$[\mathscr{A}_i,\mathscr{B}_j] = \sum_{l<m}^n\left[\left(g_i^l - g_i^m\right)g_j^{lm}\hat{b}_l^\dagger\hat{b}_m + \left(g_i^m - g_i^l\right)\left(g_j^{lm}\right)^*\hat{b}_m^\dagger\hat{b}_l\right], \tag{B3}$$

$$[\mathscr{B}_i,\mathscr{A}_j] = -\sum_{l<m}^n\left[\left(g_j^l - g_j^m\right)g_i^{lm}\hat{b}_l^\dagger\hat{b}_m + \left(g_j^m - g_j^l\right)\left(g_i^{lm}\right)^*\hat{b}_m^\dagger\hat{b}_l\right], \tag{B4}$$

$$\begin{aligned}[\mathscr{B}_i,\mathscr{B}_j] = &\sum_{k<l<m}^n\left(g_i^{kl}g_j^{lm} - g_i^{lm}g_j^{kl}\right)b_k^\dagger b_m + \left[\left(g_i^{lm}\right)^*\left(g_j^{kl}\right)^* - \left(g_i^{kl}\right)^*\left(g_j^{lm}\right)^*\right]b_m^\dagger b_k \\ &+ \sum_{k<\min(l,p)}^n\left[\left(g_i^{kl}\right)^*g_j^{kp}\hat{b}_l^\dagger\hat{b}_p - g_i^{kl}\left(g_j^{kp}\right)^*\hat{b}_p^\dagger\hat{b}_l\right] + \sum_{\{k,m\}<l}^n\left[g_i^{kl}\left(g_j^{ml}\right)^*\hat{b}_k^\dagger\hat{b}_m - \left(g_i^{kl}\right)^*g_j^{ml}\hat{b}_m^\dagger\hat{b}_k\right],\end{aligned} \tag{B5}$$

where $\sum_{k<\min(l,p)}^n \equiv \sum_l^n\sum_p^n\sum_k^{\min(l,p)-1}$ and $\sum_{\{k,m\}<l}^n \equiv \sum_l^n\sum_m^{l-1}\sum_k^{l-1}$. For the two-mode interferometer ($n=2$), the diagonal elements of $\mathbf{M}_i$ are the same for any parameter estimation due to the central symmetry of two antenna. Then, we have $[\mathscr{A}_i,\mathscr{B}_j] = [\mathscr{B}_i,\mathscr{A}_j] = 0$, the first summation vanishes, and we have $[\mathscr{B}_i,\mathscr{B}_j] = [g_i^{12}(g_j^{12})^* - (g_i^{12})^*g_j^{12}](\hat{b}_1^\dagger b_1 - \hat{b}_2^\dagger\hat{b}_2)$. Since $\langle b_1^\dagger b_1\rangle = \langle b_2^\dagger b_2\rangle = \bar{n}$, we obtain $\mathrm{Tr}\,[\rho_{\mathrm{int}}[\mathscr{L}_i,\mathscr{L}_j]] = 0$.

APPENDIX C: GENERAL QFI AND THE ELEMENTS OF THE MATRIX M FOR A TWO-MODE INTERFEROMETER

In this Appendix, we give the general results for the elements of the QFI and the matrix $\mathbf{M}_i$ for a two-mode interferometer, assuming that all the elements of the covariance matrix depend on the parameter μ_i that we want to estimate. Using the covariance matrix for a two-mode interferometer one finds the QFI matrix elements as

$$\begin{aligned}\mathscr{F}_{ij} = \frac{8}{\mathscr{D}}\big\{&\partial_i\xi^*\partial_j\xi[(1-4\chi^2)^2 - 4(1+4\chi^2)|\xi|^2] + \partial_i\xi\partial_j\xi^*[(1-4\chi^2)^2 - 4(1+4\chi^2)|\xi|^2] \\ &+ 4\xi\partial_i\xi^*[\xi\partial_j\xi^*(1+4\chi^2-4|\xi|^2) + 2\chi\partial_j\chi(1-4\chi^2+4|\xi|^2)] + 4\xi^*\partial_i\xi[\xi\partial_j\xi^*(1+4\chi^2-4|\xi|^2) \\ &+ 2\chi\partial_j\chi(1-4\chi^2+4|\xi|^2)] + 2\partial_i\chi(-1+4\chi^2-4|\xi|^2)[-4\chi(\xi\partial_j\xi^* + \xi^*\partial_j\xi) + \partial_j\chi(-1+4\chi^2+4|\xi|^2)]\big\},\end{aligned} \tag{C1}$$

where the denominator is given by

$$\mathscr{D} = (-1 + 4\chi^2 - 4|\xi|^2)[16\chi^4 + (1 - 4|\xi|^2)^2 - 8\chi^2(1 + |\xi|^2)]. \tag{C2}$$

Using the SLD given in Eq. (38) we find the diagonal elements of the matrix $\mathbf{M}_i$ given in Eq. (56) as

$$g_i^1 = \frac{2(4\partial_i\chi|\xi|^2 + 4\partial_i\chi\chi^2 - 4\partial_i\xi\xi^*\chi - 4\partial_i\xi^*\xi\chi - \partial_i\chi)}{16\chi^4 - 8\chi^2(4|\xi|^2 + 1) + (1 - 4|\xi|^2)^2}, \tag{C3}$$

where the two diagonal elements are the same due to the symmetry with respect to the center of the two antennas, and

$$g_i^2 = \frac{2}{\mathscr{D}}\{-\partial_i\xi(16|\xi|^2\chi^2 + 4|\xi|^2 - 16\chi^4 + 8\chi^2 - 1) - \partial_i\xi^*[4\xi^2(4|\xi|^2 - 1) - 16\xi^2\chi^2] - \partial_i\chi[32\xi\chi^3 - 8\xi\chi(4|\xi|^2 + 1)]\}, \tag{C4}$$

where $\mathscr{D}$ is given in Eq. (C2).

APPENDIX D: POVM FOR HETERODYNE DETECTION

The POVM for heterodyne detection is given in Ref. [34], and the CFI analyzed for the weak thermal sources. Here we briefly introduce the POVM for heterodyne detection. Then, we compare our results for the QFI with the CFI for heterodyne detection. The POVM is given as

$$E(\nu_1, \nu_2) = \frac{1}{\pi^2}|\nu_1, \nu_2\rangle\langle\nu_1, \nu_2|, \tag{D1}$$

where $|\nu_1, \nu_2\rangle$ is a coherent state with normalization given by $\int d^2\nu_1 d^2\nu_2 E(\nu_1, \nu_2) = \mathbb{1}$. The covariance matrix for a two-mode interferometer is given in Eq. (55). Using the corresponding state for the two-mode interferometer we can find the observation probability for any parameter μ_i, in terms of the elements of the covariance matrix as

$$P(\nu_1, \nu_2|\mu_i) = \frac{1}{\pi^2[(1 + \bar{n})^2 - |\xi|^2]} \exp\left[\frac{(-|\nu_1|^2 - |\nu_2|^2)(1 + \bar{n}) + \xi\nu_1^*\nu_2 + \xi^*\nu_2^*\nu_1}{(1 + \bar{n})^2 - |\xi|^2}\right]. \tag{D2}$$

The Fisher information for the parameter μ_i can be found as

$$\begin{aligned} F_i &= \int d^2\nu_1 d^2\nu_2 \frac{1}{P(\nu_1, \nu_2|\mu_i)}\left(\frac{\partial P(\nu_1, \nu_2|\mu_i)}{\partial\mu_i}\right)^2 \\ &= \int d^2\nu_1 d^2\nu_2 P(\nu_1, \nu_2|\mu_i) f(\nu_1, \nu_2) \\ &= \langle f(\nu_1, \nu_2)\rangle, \end{aligned} \tag{D3}$$

where $f(\nu_1, \nu_2)$ is a polynomial function of second- and fourth-order correlations of ν_1 and ν_2, defined as

$$f(\nu_1, \nu_2) \equiv \{\partial_{\mu_i} \ln[P(\nu_1, \nu_2|\mu_i)]\}^2 = \frac{1}{[P(\nu_1, \nu_2|\mu_i)]^2}\left(\frac{\partial P(\nu_1, \nu_2|\mu_i)}{\partial\mu_i}\right)^2. \tag{D4}$$

With Wick's theorem for Gaussian states, the fourth-order statistic can be written as

$$\langle x_1 x_2 x_3 x_4\rangle = \langle x_1 x_2\rangle\langle x_3 x_4\rangle + \langle x_1 x_3\rangle\langle x_2 x_4\rangle + \langle x_1 x_4\rangle\langle x_2 x_3\rangle, \tag{D5}$$

where $x_i \in \{\nu_1, \nu_1^*, \nu_2, \nu_2^*\}$. We can also write $\langle|\nu_1|^2\rangle = \langle|\nu_2|^2\rangle = 1 + \bar{n}$ and $\langle\nu_1^*\nu_2\rangle = \xi$, $\langle\nu_2^*\nu_1\rangle = \xi^*$.

APPENDIX E: UNIFORM CIRCULAR SOURCE FOR A TWO-MODE INTERFEROMETER

We find the elements of the covariance matrix describing the state of two-mode interferometers in Eq. (55). Then for a circular source with size a located at position (x_0, y_0, R) with the assumption $x_0, y_0 \ll R$ in the source plane we have

$$\begin{aligned} \bar{n} &= \frac{\kappa T}{R^2}\int dx\, dy\, \mathrm{circ}(x - x_0, y - y_0) \\ &= \frac{\pi a^2\kappa T}{R^2}, \end{aligned} \tag{E1}$$

and χ and ξ become

$$\chi = \frac{1}{2} + \frac{\pi a^2 \kappa T}{R^2}, \tag{E2}$$

$$\xi = \langle b_2^\dagger b_1 \rangle = \frac{\kappa T}{R^2} \int dx\, dy\, \mathrm{circ}(x - x_0, y - y_0) \exp\left[2\pi i (x v_x + y v_y)\right]$$

$$= \frac{\kappa T a^2}{R^2} \frac{J_1\left(2\pi a \sqrt{v_x^2 + v_y^2}\right)}{a\sqrt{v_x^2 + v_y^2}} \exp\left[2\pi i (x_0 v_x + y_0 v_y)\right], \tag{E3}$$

where $v_x = \Delta r \cos\varphi/(\lambda R)$, $v_y = \Delta r \sin\varphi/(\lambda R)$, with $\mathbf{\Delta r} = \Delta r(\cos\varphi, \sin\varphi, 0)$. Note that $\sqrt{v_x^2 + v_y^2} = \Delta r/(\lambda R)$.

1. Quantum Fisher information: The uniform circular source

We found the QFI for estimating a is as

$$\mathscr{F}_a = \frac{8\pi^2 a \Delta r^2 \kappa T}{\mathscr{D}_a}\left[\pi a \Delta r^2 (\pi a^2 \kappa T + R^2)(J_0^2 + 1) - 2\Delta r \lambda R (2\pi a^2 \kappa T + R^2) J_0 J_1 + a\kappa\lambda^2 R^2 T (J_0^2 + 1) J_1^2\right], \tag{E4}$$

where

$$\mathscr{D}_a = \left(\pi^2 a^2 \Delta r^2 - \lambda^2 R^2 J_1^2\right)\left[\Delta r^2 (\pi a^2 \kappa T + R^2)^2 - \kappa^2 \lambda^2 R^2 T^2 J_1^2\right], \tag{E5}$$

and $J_i(\frac{2a\Delta r\pi}{R\lambda})$ are the Bessel functions of the first kind and ith order. The QFI for estimating T becomes

$$\mathscr{F}_T = \frac{2\kappa a^2\left[\pi \Delta r^2 (\pi a^2 \kappa T + R^2) - \kappa \lambda^2 R^2 T J_1^2\right]}{T\left[\Delta r^2 (\pi a^2 \kappa T + R^2)^2 - a^2 \kappa^2 \lambda^2 R^2 T^2 J_1^2\right]}. \tag{E6}$$

The other elements regarding the source size and the temperature of the circular source can be found as

$$\mathscr{F}_{aT} = \frac{4\pi a \Delta r \kappa [\Delta r (\pi a^2 \kappa T + R^2) - a\kappa\lambda R T J_0 J_1]}{\Delta r^2 (\pi a^2 \kappa T + R^2)^2 - a^2 \kappa^2 \lambda^2 R^2 T^2 {J_1}^2}. \tag{E7}$$

The QFI matrix elements for estimating the source locations can be written as

$$\mathscr{F}_{i_0 j_0} = \frac{8\pi^2 R^2 \lambda^2 \kappa T {J_1}^2 v_i v_j}{\pi \Delta r^2 (\pi a^2 \kappa T + R^2) - \kappa \lambda^2 R^2 T {J_1}^2}, \tag{E8}$$

where $i, j \in \{x, y\}$.

2. Elements of the matrix $\mathbf{M}_i$ for a two-mode interferometer: The uniform circular source

To combine two modes of the receivers for the optimum measurements, we calculate δ as given in Eq. (57). We find the matrix elements of $\mathbf{M}_a$ as

$$g_a^1 = \frac{2\pi \Delta r^2 R^2}{\mathscr{D}_a}\{\pi a \Delta r^2 (\pi a^2 \kappa T + R^2) + \lambda R J_1 [a\kappa\lambda R T J_1 - \Delta r (2\pi a^2 \kappa T + R^2) J_0]\}, \tag{E9}$$

$$g_a^2 = \frac{2\pi \Delta r^2 R^2}{\mathscr{D}_a}\{a J_0 [\pi \Delta r^2 (\pi a^2 \kappa T + R^2) + \kappa \lambda^2 R^2 T J_1^2] - \Delta r \lambda R (2\pi a^2 \kappa T + R^2) J_1\} e^{-i\delta}, \tag{E10}$$

where $\delta = v_x x_0 + v_y y_0$. For the temperature estimation we get the elements of $\mathbf{M}_T$ as

$$g_T^1 = \frac{\Delta r^2 R^2 (\pi a^2 \kappa T + R^2)}{\Delta r^2 T (\pi a^2 \kappa T + R^2)^2 - a^2 \kappa^2 \lambda^2 R^2 T^3 J_1^2}, \tag{E11}$$

$$g_T^2 = -\frac{a \Delta r \kappa \lambda R^3 J_1 e^{-i\delta}}{a^2 \kappa^2 \lambda^2 R^2 T^2 J_1^2 - \Delta r^2 (\pi a^2 \kappa T + R^2)^2}. \tag{E12}$$

Finally, for the source location we found

$$\begin{pmatrix} g^2_{x_0} \\ g^2_{y_0} \end{pmatrix} = -\frac{2\pi\Delta r^2 R^2 J_1 e^{i(-\delta+\pi/2)}}{a\left[\pi\Delta r^2(\pi a^2\kappa T + R^2) - \kappa\lambda^2 R^2 T J_1^2\right]} \begin{pmatrix} \cos(\varphi) \\ \sin(\varphi) \end{pmatrix}, \tag{E13}$$

and $g^1_{x_0} = g^1_{y_0} = 0$.

3. Classical Fisher information for heterodyne detection: The uniform circular source

Since we calculated the elements of the covariance matrix in Eqs. (E1) and (E2) we can calculate Eqs. (D2) and (D4). Using the CFI for the heterodyne detection in Eq. (D3), we can write the result for estimating the source size as

$$\begin{aligned} F_a = \frac{8\pi^2 a^2\kappa^2 T^2\Delta r^3(\pi a^2\kappa T + R^2)}{D_a}\big[&4a^5\kappa^5\lambda^5 R^5 T^5 J_0 {J_1}^5 - 2a^2\Delta r^3\kappa^2\lambda^2 R^2 T^2(\pi a^2\kappa T + R^2)^3({J_0}^2 + 1)J_1^2 \\ &+ \Delta r^5(\pi a^2\kappa T + R^2)^5({J_0}^2 + 1) - 4a\Delta r^4\kappa\lambda R T(\pi a^2\kappa T + R^2)^4 J_0 J_1 \\ &- 7a^4\Delta r\kappa^4\lambda^4 R^4 T^4(\pi a^2\kappa T + R^2)({J_0}^2 + 1){J_1}^4 + 16a^3\Delta r^2\kappa^3\lambda^3 R^3 T^3(\pi a^2\kappa T + R^2)^2 J_0 J_1^3\big], \end{aligned} \tag{E14}$$

with

$$D_a = \left[\Delta r^2(\pi a^2\kappa T + R^2)^2 - a^2\kappa^2\lambda^2 R^2 T^2 J_1^2\right]^4. \tag{E15}$$

The estimation of the temperature becomes

$$\begin{aligned} F_T = \frac{2a^2\Delta r^2\kappa^2(\pi a^2\kappa T + R^2)}{D_T}\big[&\pi^2 a^2\Delta r^6(\pi a^2\kappa T + R^2)^5 - a^4\kappa^4\lambda^6 R^6 T^4(3\pi a^2\kappa T + 7R^2)J_1^6 \\ &+ \Delta r^4\lambda^2 R^2(\pi a^2\kappa T + R^2)^3(-5\pi^2 a^4\kappa^2 T^2 - 2\pi a^2\kappa R^2 T + R^4)J_1^2 + a^2\Delta r^2\kappa^2\lambda^4 R^4 T^2(7\pi^3 a^6\kappa^3 T^3 \\ &+ 19\pi^2 a^4\kappa^2 R^2 T^2 + 10\pi a^2\kappa R^4 T - 2R^6)J_1^4\big], \end{aligned} \tag{E16}$$

where

$$D_T = \left[\Delta r^2(\pi a^2\kappa T + R^2)^2 - a^2\kappa^2\lambda^2 R^2 T^2 J_1^2\right]^4. \tag{E17}$$

APPENDIX F: TWO-POINT SOURCES FOR A TWO-MODE INTERFEROMETER

The temperature distribution of two circular sources with equal size a at locations (x_1, y_1, R) and (x_2, y_2, R) is given in Eq. (65). We assume that $\{|x_i|, |y_i|, a\} \ll R$. The elements of the covariance matrix in Eq. (55) for two-point sources with different temperature can be found using Eqs. (31), (32), and (65) as

$$\begin{aligned} \chi &= \frac{1}{2} + \sum_i \frac{\pi a^2\kappa T_i}{R^2} = \frac{1}{2} + \frac{2\pi a^2\kappa T}{R^2} \\ &= \frac{1}{2} + 2\eta\kappa T, \end{aligned} \tag{F1}$$

where $\eta = \pi a^2/R^2$, and

$$\begin{aligned} \xi = \langle b_1^\dagger b_2\rangle &= \frac{\kappa\pi a^2}{R^2}\frac{2J_1\left(\frac{2\pi a\Delta r}{R\lambda}\right)}{\frac{2\pi a\Delta r}{R\lambda}}(T_1 e^{2\pi i(v_x x_1 + v_y y_1)} \\ &\quad + T_2 e^{2\pi i(v_x x_2 + v_y y_2)}) \\ &= \frac{\kappa\eta\eta_2}{2}[(2T - \Delta T)e^{2\pi i(v_x x_1 + v_y y_1)} \\ &\quad + (2T + \Delta T)e^{2\pi i(v_x x_2 + v_y y_2)}], \end{aligned} \tag{F2}$$

where the average temperature is defined as $T \equiv (T_1 + T_2)/2$, and the temperature difference of the sources as $\Delta T \equiv T_2 - T_1$ with $T_2 \geqslant T_1$ assumed, while the parameter η_2 is given by

$$\eta_2 = \frac{2J_1\left(\frac{2\pi a\Delta r}{R\lambda}\right)}{\frac{2\pi a\Delta r}{R\lambda}}, \tag{F3}$$

which is related to the source size. In Fig. 7, we can see the behavior of η_2 with respect to the source size. For point sources one can approximate $\eta_2 \approx 1$.

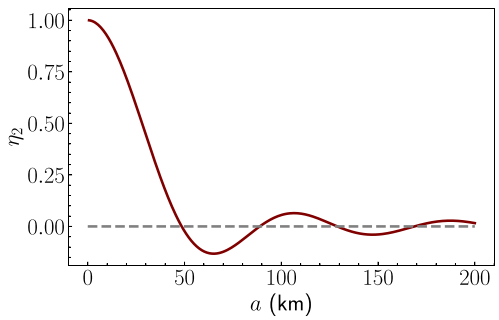

FIG. 7. Plot showing the behavior of η_2 with respect to the radius of the circular disk source with $\Delta r = 2$ m.

1. Quantum Fisher information: Two-point sources

We found the elements of the QFI matrix for estimating the source separation as

$$\mathscr{F}_{s_i s_j} = \frac{2\pi^2 \eta\kappa v_i v_j}{\mathscr{D}_{s_x s_y}} (\eta^2\kappa^2(4T^2-\Delta T^2)\{(4T^2-\Delta T^2)\cos[4\pi(s_x v_x + s_y v_y)] + 16T^2\cos[2\pi(s_x v_x + s_y v_y)]\}$$
$$-\eta^2\kappa^2(\Delta T^4 - 24\Delta T^2 T^2 + 80T^4) - 128\eta\kappa T^3 - 32T^2), \tag{F4}$$

where $i, j = \{x, y\}$ and the denominator is given by

$$\mathscr{D}_{s_x s_y} = \eta\kappa(4T^2-\Delta T^2)\{\eta^2\kappa^2(\Delta T^2 - 4T^2)\cos[4\pi(s_x v_x + s_y v_y)]$$
$$+ 4[\eta\kappa(-\Delta T^2\eta\kappa + 4\eta\kappa T^2 + 6T) + 1]\cos[2\pi(s_x v_x + s_y v_y)]\}$$
$$- 3\eta^3\kappa^3(\Delta T^2 - 4T^2)^2 + 24\eta^2\kappa^2 T(\Delta T^2 - 4T^2) + 4\eta\kappa(\Delta T^2 - 20T^2) - 16T. \tag{F5}$$

The elements of QFI matrix for estimating the centroid becomes

$$\mathscr{F}_{t_i t_j} = \frac{16\pi^2 v_i v_j \eta\kappa}{\mathscr{D}_t}[(4T^2-\Delta T^2)\cos(2\pi(s_x v_x + s_y v_y)) + \Delta T^2 + 4T^2], \tag{F6}$$

where the denominator is

$$\mathscr{D}_t = 4T + 4\eta\kappa T^2 - \Delta T^2\eta\kappa - \eta\kappa(4T^2-\Delta T^2)\cos[2\pi(s_x v_x + s_y v_y)]. \tag{F7}$$

Off-diagonal elements of the QFI matrix can be found as

$$\mathscr{F}_{s_i t_j} = \frac{32\pi^2\Delta T\eta\kappa T v_i v_j}{\Delta T^2\eta\kappa + \eta\kappa(4T^2-\Delta T^2)\cos[2\pi(s_x v_x + s_y v_y)] - 4\eta\kappa T^2 - 4T}. \tag{F8}$$

If we align two antennas parallel to the source separation, $v_x \to v$ and $v_y \to 0$. In the limit where $\Delta T \to 0$ the QFI for the source separation simplifies to

$$\mathscr{F}_s \to \frac{4\pi^2 v^2\eta\kappa T[\eta\kappa T\cos(2\pi s v) + 3\eta\kappa T + 1]}{[1 + 4\eta\kappa T + 2\eta^2\kappa^2 T^2 - 2\eta^2\kappa^2 T^2\cos(2\pi s v)]}, \tag{F9}$$

and the QFI for the centroid simplifies to

$$\mathscr{F}_t \to \frac{32\pi^2 v^2\eta\kappa T\cos^2(\pi s v)}{1 + \eta\kappa T - \eta\kappa T\cos(2\pi s v)}, \tag{F10}$$

which agrees with the results in Ref. [35] for ($\Delta T = 0$, $v_y = 0$, $s_y = 0$, $t_y = 0$) as expected.

2. Elements of the matrix $\mathbf{M}_i$ for a two-mode interferometer: Two-point sources

For simplicity let us assume that $\Delta T \to 0$. Then we have the elements of the matrix $\mathbf{M}_i$ for a two-mode interferometer for estimating the source sizes as

$$g^1_{s_i} = \frac{\pi v_i(4\eta\kappa T + 1)\cot[\pi(s_x v_x + s_y v_y)]}{\{1 + 4\eta\kappa T + 2\eta^2\kappa^2 T^2 - 2\eta^2\kappa^2 T^2\cos[2\pi(s_x v_x + s_y v_y)]\}},$$
$$g^2_{s_i} = \frac{\pi v_i\{\eta\kappa T\cos[2\pi(s_x v_x + s_y v_y)] + 3\eta\kappa T + 1\}\csc[\pi(s_x v_x + s_y v_y)]\exp(-i\delta_s)}{\{1 + 4\eta\kappa T + 2\eta^2\kappa^2 T^2 - 2\eta^2\kappa^2 T^2\cos[2\pi(s_x v_x + s_y v_y)]\}}, \tag{F11}$$

and

$$g^1_{t_i} = 0,$$
$$g^2_{t_i} = \frac{2\pi v\cos[\pi(s_x v_x + s_y v_y)]\exp(-i\delta_t)}{1 + \eta\kappa T - \eta\kappa T\cos[2\pi(s_x v_x + s_y v_y)]}, \tag{F12}$$

where $\delta_s = 2\pi(t_x v_x + t_y v_y) - \pi$ and $\delta_t = 2\pi(t_x v_x + t_y v_y) + \pi/2$.

3. Classical Fisher information for heterodyne detection: Two-point sources

Using the CFI given for the heterodyne detection in Eq. (D3), and assuming that both sources have the same temperature ($\Delta T \to 0$), one can find the CFI for estimating the centroid as

$$F_{t_i} = \frac{32\pi^2\eta^2\kappa^2 T^2 v_i^2(2\eta\kappa T + 1)^2\cos^2[\pi(s_x v_x + s_y v_y)]}{\{-2\eta^2\kappa^2 T^2\cos[2\pi(s_x v_x + s_y v_y)] + 2\eta\kappa T(\eta\kappa T + 2) + 1\}^2}. \tag{F13}$$

Again assuming ($\Delta T \to 0$), we can find the CFI for estimating the source separation as

$$F_{s_i} = \frac{1}{D_s} 8\pi^2\eta^2\kappa^2T^2v_i^2 \sin^2[\pi(s_xv_x + s_yv_y)](2\eta\kappa T + 1)^2(1 - 14\eta^4\kappa^4T^4\cos[4\pi(s_xv_x + s_yv_y)] - 4\eta^2\kappa^2T^2\cos[2\pi(s_xv_x + s_yv_y)][2\eta\kappa T(9\eta\kappa T + 2) + 1] - 2\eta\kappa T\{\eta\kappa T[\eta\kappa T(21\eta\kappa T - 8) - 10] - 4\}), \quad \text{(F14)}$$

where the denominator is given by

$$D_s = \{1 + 4\eta\kappa T + 2\eta^2\kappa^2T^2 - 2\eta^2\kappa^2T^2\cos[2\pi(s_xv_x + s_yv_y)]\}^4. \quad \text{(F15)}$$

[1] S. W. Hell and J. Wichmann, Breaking the diffraction resolution limit by stimulated emission: Stimulated-emission-depletion fluorescence microscopy, Opt. Lett. **19**, 780 (1994).

[2] S. W. Hell, Far-Field Optical Nanoscopy, Science **316**, 1153 (2007).

[3] M. Tsang, R. Nair, and X.-M. Lu, Quantum Theory of Superresolution for Two Incoherent Optical Point Sources, Phys. Rev. X **6**, 031033 (2016).

[4] C. W. Helstrom, Detection theory and quantum mechanics, Inform. Comput. **10**, 254 (1967).

[5] C. W. Helstrom, Quantum detection and estimation theory, J. Stat. Phys. **1**, 231 (1969).

[6] C. W. Helstrom, Cramer-Rao inequalities for operator-valued measures in quantum mechanics, Int. J. Theor. Phys. **8**, 361 (1973).

[7] C. W. Helstrom, Estimation of Object Parameters by a Quantum-Limited Optical System, J. Opt. Soc. Am. **60**, 233 (1970).

[8] M. Tsang, Quantum limits to optical point-source localization, Optica **2**, 646 (2015).

[9] M. Tsang, Quantum limit to subdiffraction incoherent optical imaging, Phys. Rev. A **99**, 012305 (2019).

[10] S. Zhou and L. Jiang, Modern description of Rayleigh's criterion, Phys. Rev. A **99**, 013808 (2019).

[11] G. Sorelli, M. Gessner, M. Walschaers, and N. Treps, Moment-based superresolution: Formalism and applications Phys. Rev. A **104**, 033515 (2021).

[12] J. Řehaček, Z. Hradil, B. Stoklasa, M. Paúr, J. Grover, A. Krzic, and L. L. Sánchez-Soto, Multiparameter quantum metrology of incoherent point sources: Towards realistic superresolution, Phys. Rev. A **96**, 062107 (2017).

[13] C. Napoli, S. Piano, R. Leach, G. Adesso, and T. Tufarelli, Towards Superresolution Surface Metrology: Quantum Estimation of Angular and Axial Separations, Phys. Rev. Lett. **122**, 140505 (2019).

[14] R. Nair and M. Tsang, Far-Field Superresolution of Thermal Electromagnetic Sources at the Quantum Limit, Phys. Rev. Lett. **117**, 190801 (2016).

[15] C. Lupo and S. Pirandola, Ultimate Precision Bound of Quantum and Subwavelength Imaging, Phys. Rev. Lett. **117**, 190802 (2016).

[16] W. Larson and B. E. A. Saleh, Resurgence of Rayleigh's curse in the presence of partial coherence, Optica **5**, 1382 (2018).

[17] S. Kurdziałek and R. Demkowicz-Dobrzański, Super-resolution optical fluctuation imaging—fundamental estimation theory perspective, J. Opt. **23**, 075701 (2021).

[18] M. I. Kolobov and C. Fabre, Quantum Limits on Optical Resolution, Phys. Rev. Lett. **85**, 3789 (2000).

[19] S. Z. Ang, R. Nair, and M. Tsang, Quantum limit for two-dimensional resolution of two incoherent optical point sources, Phys. Rev. A **95**, 063847 (2017).

[20] E. Bisketzi, D. Branford, and A. Datta, Quantum limits of localisation microscopy, New J. Phys. **21**, 123032 (2019).

[21] M. Bojer, Z. Huang, S. Karl, S. Richter, P. Kok, and J. von Zanthier, A quantitative comparison of amplitude versus intensity interferometry for astronomy, New J. Phys. **24**, 043026 (2022).

[22] C. Datta, M. Jarzyna, Y. L. Len, K. Łukanowski, J. Kołodyński, and K. Banaszek, Sub-Rayleigh resolution of two incoherent sources by array homodyning, Phys. Rev. A **102**, 063526 (2020).

[23] J. O. de Almeida, J. Kołodyński, C. Hirche, M. Lewenstein, and M. Skotiniotis, Discrimination and estimation of incoherent sources under misalignment, Phys. Rev. A **103**, 022406 (2021).

[24] K. Liang, S. A. Wadood, and A. N. Vamivakas, Coherence effects on estimating general sub-rayleigh object distribution moments Phys. Rev. A **104**, 022220 (2021).

[25] M. Tsang, Subdiffraction incoherent optical imaging via spatial-mode demultiplexing, New J. Phys. **19**, 023054 (2017).

[26] O. Pinel, J. Fade, D. Braun, P. Jian, N. Treps, and C. Fabre, Ultimate sensitivity of precision measurements with intense Gaussian quantum light: A multimodal approach, Phys. Rev. A **85**, 010101(R) (2012).

[27] M. P. Backlund, Y. Shechtman, and R. L. Walsworth, Fundamental Precision Bounds for Three-Dimensional Optical Localization Microscopy with Poisson Statistics, Phys. Rev. Lett. **121**, 023904 (2018).

[28] M. Mazelanik, A. Leszczynski, and M. Parniak, Optical-domain spectral super-resolution enabled by a quantum memory, Nat. Commun. **13**, 691 (2022).

[29] M. Paúr, B. Stoklasa, Z. Hradil, L. L. Sánchez-Soto, and J. Rehacek, Achieving the ultimate optical resolution, Optica **3**, 1144 (2016).

[30] A. A. Pushkina, G. Maltese, J. I. Costa-Filho, P. Patel, and A. I. Lvovsky, Super-Resolution Linear Optical Imaging in the Far Field, Phys. Rev. Lett. **127**, 253602 (2021).

[31] C. Lupo, Z. Huang, and P. Kok, Quantum Limits to Incoherent Imaging are Achieved by Linear Interferometry, Phys. Rev. Lett. **124**, 080503 (2020).

[32] D. Gottesman, T. Jennewein, and S. Croke, Longer-Baseline Telescopes Using Quantum Repeaters, Phys. Rev. Lett. **109**, 070503 (2012).

[33] E. T. Khabiboulline, J. Borregaard, K. De Greve, and M. D. Lukin, Optical Interferometry with Quantum Networks, Phys. Rev. Lett. **123**, 070504 (2019).

[34] M. Tsang, Quantum Nonlocality in Weak-Thermal-Light Interferometry, Phys. Rev. Lett. **107**, 270402 (2011).

[35] Y. Wang, Y. Zhang, and V. O. Lorenz, Superresolution in interferometric imaging of strong thermal sources, Phys. Rev. A **104**, 022613 (2021).

[36] E. Anterrieu, A resolving matrix approach for synthetic aperture imaging radiometers, IEEE Trans. Geosci. Remote Sens. **42**, 1649 (2004).

[37] I. Corbella, N. Duffo, M. Vall-llossera, A. Camps, and F. Torres, The visibility function in interferometric aperture synthesis radiometry, IEEE Trans. Geosci. Remote Sens. **42**, 1677 (2004).

[38] D. Le Vine, Synthetic aperture radiometer systems, IEEE Trans. Microw. Theory Tech. **47**, 2228 (1999).

[39] A. R. Thompson, J. M. Moran, and George W. Swenson Jr., *Interferometry and Synthesis in Radio Astronomy* (Springer, Cham, 2017).

[40] P. van Cittert, Die wahrscheinliche schwingungsverteilung in einer von einer lichtquelle direkt oder mittels einer linse beleuchteten ebene, Physica (Amsterdam) **1**, 201 (1934).

[41] F. Zernike, The concept of degree of coherence and its application to optical problems, Physica (Amsterdam) **5**, 785 (1938).

[42] D. Braun, Y. Monjid, B. Rougé, and Y. Kerr, Generalization of the Van Cittert–Zernike theorem: Observers moving with respect to sources, Meas. Sci. Technol. **27**, 015002 (2016).

[43] D. Braun, Y. Monjid, B. Rougé, and Y. Kerr, Fourier-correlation imaging, J. Appl. Phys. **123**, 074502 (2018).

[44] J. R. Jeffers, N. Imoto, and R. Loudon, Quantum optics of traveling-wave attenuators and amplifiers, Phys. Rev. A **47**, 3346 (1993).

[45] J. Liu, H. Yuan, X.-M. Lu, and X. Wang, Quantum Fisher information matrix and multiparameter estimation, J. Phys. A: Math. Theor. **53**, 023001 (2020).

[46] O. Pinel, P. Jian, N. Treps, C. Fabre, and D. Braun, Quantum parameter estimation using general single-mode Gaussian states, Phys. Rev. A **88**, 040102(R) (2013).

[47] J. Shapiro, The Quantum Theory of Optical Communications, IEEE J. Sel. Top. Quantum Electron. **15**, 1547 (2009).

[48] J. S. Sidhu and P. Kok, Geometric perspective on quantum parameter estimation, AVS Quantum Sci. **2**, 014701 (2020).

[49] D. Šafránek, Estimation of Gaussian quantum states, J. Phys. A: Math. Theor. **52**, 035304 (2019).

[50] R. Nichols, P. Liuzzo-Scorpo, P. A. Knott, and G. Adesso, Multiparameter Gaussian quantum metrology, Phys. Rev. A **98**, 012114 (2018).

[51] D. Braun, G. Adesso, F. Benatti, R. Floreanini, U. Marzolino, M. W. Mitchell, and S. Pirandola, Quantum-enhanced measurements without entanglement, Rev. Mod. Phys. **90**, 035006 (2018).

[52] A. Holevo, Statistical decision theory for quantum systems, J. Multivariate Anal. **3**, 337 (1973).

[53] S. Ragy, M. Jarzyna, and R. Demkowicz-Dobrzański, Compatibility in multiparameter quantum metrology, Phys. Rev. A **94**, 052108 (2016).

[54] C. Oh, S. Zhou, Y. Wong, and L. Jiang, Quantum Limits of Superresolution in a Noisy Environment, Phys. Rev. Lett. **126**, 120502 (2021).

[55] M. Gessner, C. Fabre, and N. Treps, Superresolution Limits from Measurement Crosstalk, Phys. Rev. Lett. **125**, 100501 (2020).

[56] Y. L. Len, C. Datta, M. Parniak, and K. Banaszek, Resolution limits of spatial mode demultiplexing with noisy detection, Int. J. Quantum Inf. **18**, 1941015 (2020).

[57] K. J. Blow, R. Loudon, S. J. D. Phoenix, and T. J. Shepherd, Continuum fields in quantum optics, Phys. Rev. A **42**, 4102 (1990).

[58] L. Mandel, E. Wolf, and P. Meystre, Optical Coherence and Quantum Optics, Am. J. Phys. **64**, 1438 (1996).

[59] R. J. Glauber, Coherent and Incoherent States of the Radiation Field, Phys. Rev. **131**, 2766 (1963).

[60] M. O. Scully, M. S. Zubairy, and I. A. Walmsley, Quantum Optics, Am. J. Phys. **67**, 648 (1999).

[61] R. Loudon and T. von Foerster, The Quantum Theory of Light, Am. J. Phys. **42**, 1041 (1974).

[62] J. Zmuidzinas, Cramér–Rao sensitivity limits for astronomical instruments: Implications for interferometer design, J. Opt. Soc. Am. A **20**, 218 (2003).

[63] J. Zmuidzinas, Thermal noise and correlations in photon detection, Appl. Opt. **42**, 4989 (2003).

[64] R. Kubo, The fluctuation-dissipation theorem, Rep. Prog. Phys. **29**, 255 (1966).

[65] S. Savasta, O. Di Stefano, and R. Girlanda, Light quantization for arbitrary scattering systems, Phys. Rev. A **65**, 043801 (2002).

[66] E. A. Sharkov, *Passive Microwave Remote Sensing of the Earth: Physical Foundations* (Springer, Berlin, 2011).

[67] L. D. Landau, E. M. Lifshits, L. P. Pitaevsk, L. D. Landau, and L. D. Landau, *Statistical Physics* (Pergamon, Oxford, 1980), Vols. 5, 9.

[68] R. Carminati and J.-J. Greffet, Near-Field Effects in Spatial Coherence of Thermal Sources, Phys. Rev. Lett. **82**, 1660 (1999).

[69] D. Braun, P. Jian, O. Pinel, and N. Treps, Precision measurements with photon-subtracted or photon-added Gaussian states, Phys. Rev. A **90**, 013821 (2014).

[70] G. Adesso, S. Ragy, and A. R. Lee, Continuous variable quantum information: Gaussian states and beyond, Open Syst. Inf. Dyn. **21**, 1440001 (2014).

[71] Y. Gao and H. Lee, Bounds on quantum multiple-parameter estimation with Gaussian state, Eur. Phys. J. D **68**, 347 (2014).

[72] S. Olivares, Quantum optics in the phase space: A tutorial on Gaussian states, Eur. Phys. J.: Spec. Top. **203**, 3 (2012).

[73] C. Weedbrook, S. Pirandola, R. García-Patrón, N. J. Cerf, T. C. Ralph, J. H. Shapiro, and S. Lloyd, Gaussian quantum information, Rev. Mod. Phys. **84**, 621 (2012).

[74] M. Szczykulska, T. Baumgratz, and A. Datta, Multi-parameter quantum metrology, Adv. Phys.: X **1**, 621 (2016).

[75] M. Tsang, F. Albarelli, and A. Datta, Quantum Semiparametric Estimation, Phys. Rev. X **10**, 031023 (2020).

[76] F. Albarelli, M. Barbieri, M. Genoni, and I. Gianani, A perspective on multiparameter quantum metrology: From theoretical tools to applications in quantum imaging, Phys. Lett. A **384**, 126311 (2020).

[77] S. L. Braunstein and C. M. Caves, Statistical Distance and the Geometry of Quantum States, Phys. Rev. Lett. **72**, 3439 (1994).

[78] M. G. A. Paris, Quantum estimation for quantum technology, Int. J. Quantum Inf. **07**, 125 (2009).

[79] J. W. Goodman, *Statistical Optics* (Wiley, New York, 1985), Vol. 1, p. 567.

[80] M. E. Pearce, E. T. Campbell, and P. Kok, Optimal quantum metrology of distant black bodies, Quantum **1**, 21 (2017).

[81] L. A. Howard, G. G. Gillett, M. E. Pearce, R. A. Abrahao, T. J. Weinhold, P. Kok, and A. G. White, Optimal Imaging of Remote Bodies Using Quantum Detectors, Phys. Rev. Lett. **123**, 143604 (2019).

[82] R. Lescanne, S. Deléglise, E. Albertinale, U. Réglade, T. Capelle, E. Ivanov, T. Jacqmin, Z. Leghtas, and E. Flurin, Irreversible Qubit-Photon Coupling for the Detection of Itinerant Microwave Photons, Phys. Rev. X **10**, 021038 (2020).

[83] C. S. Wang, J. C. Curtis, B. J. Lester, Y. Zhang, Y. Y. Gao, J. Freeze, V. S. Batista, P. H. Vaccaro, I. L. Chuang, L. Frunzio, L. Jiang, S. M. Girvin, and R. J. Schoelkopf, Efficient Multiphoton Sampling of Molecular Vibronic Spectra on a Superconducting Bosonic Processor, Phys. Rev. X **10**, 021060 (2020).

Second Publication

Superresolution imaging with multiparameter quantum metrology in passive remote sensing

Emre Köse [*] and Daniel Braun [†]
Institut für Theoretische Physik, Eberhard Karls Universität Tübingen, 72076 Tübingen, Germany

(Received 11 January 2023; accepted 24 February 2023; published 14 March 2023)

We study super-resolution imaging theoretically using a distant n-mode interferometer in the microwave regime for passive remote sensing, used, e.g., for satellites like the "Soil Moisture and Ocean Salinity" (SMOS) mission to observe the surface of the Earth. We give a complete quantum-mechanical analysis of multiparameter estimation of the temperatures on the source plane. We find the optimal detection modes by combining incoming modes with an optimized unitary that enables the most informative measurement based on photon counting in the detection modes and saturates the quantum Cramér-Rao bound from the symmetric logarithmic derivative for the parameter set of temperatures. In our numerical analysis, we achieved a quantum-enhanced super-resolution by reconstructing an image using the maximum likelihood estimator with a pixel size of 3 km, which is ten times smaller than the spatial resolution of SMOS with comparable parameters. Further, we find the optimized unitary for uniform temperature distribution on the source plane, with the temperatures corresponding to the average temperatures of the image. Even though the corresponding unitary was not optimized for the specific image, it still gives a super-resolution compared to local measurement scenarios for the theoretically possible maximum number of measurements.

DOI: 10.1103/PhysRevA.107.032607

I. INTRODUCTION

The technology of imaging is currently undergoing a rapid evolution both due to enhanced computational techniques [1] and due to insights from quantum information processing and quantum metrology. It has become clear that the paradigmatic resolution limit found by Abbe and Rayleigh, based on the interference of classical waves set by the wavelength of the light, is not the ultimate fundamental bound if the quantum nature of light is taken into account. In quantum optics it was realized already in the 1960s in the context of the explication of the Hanbury–Brown Twiss effect [2,3] that fundamentally the interference of light should be considered in Hilbert space and can lead to higher-order correlations that contain information beyond the first-order correlations relevant to the interference patterns of classical electromagnetic waves. Experimentally, super-resolution was demonstrated by Hell in 1994 (see Refs. [4,5]), who resolved a molecule with nanometer resolution with light in the optical domain by a decoration of the molecule with pointlike emitters and quenching them selectively. Early theoretical work used the techniques of optimal parameter estimation to estimate the ultimate sensitivities of radar and, in fact, led to the development of quantum parameter estimation theory [6–9]. Much later, quantum parameter estimation theory was applied to determine optimal detection modes and ultimate sensitivities for arbitrary parameters encoded in the quantum state of Gaussian light [10,11]. In 2016, Nair and Tsang [17] wrote a seminal paper that considered the problem of ultimate resolution as a quantum parameter estimation problem for the distance between the two sources. They found that the quantum Fisher information (QFI) that sets the ultimate bound remains finite for two point sources of low, identical intensity in the limit of vanishing separation, whereas the classical Fisher information linked to intensity measurements in direct imaging vanishes. A large amount of theoretical [12–36] and experimental research [37–42] followed that corroborated and generalized this insight.

Most of these works concentrated on estimating one or few parameters, however, typically linked to geometrical information like the spatial separation or position of point sources and, in some cases, optical phase imaging, i.e., the joint estimation of the phases with respect to a reference mode [43–46]. While this led to important insights and solid evidence that, in many situations, quantum parameter estimation techniques can enhance resolution beyond the classical diffraction limit, imaging typically does not aim at recovering information about the separation or, more generally, the spatial position of point sources. Instead, in a typical image, the scene is covered by pixels of known locations and one wants to know for each pixel the intensity of the source in that point, its spectral composition, polarization, etc. Since an image typically consists of many pixels, imaging is then inherently a (quantum) many-parameter estimation problem, and corresponding techniques should be applied to obtain the best possible image reconstruction quality based on the gathered measurement results.

In this paper, we take an important step in this direction in passive remote sensing of Earth in the micro-wave domain, building on our previous work [47]. Here, the state of the art is interferometric antenna synthesis, with which a large effective antenna can be formed from a set of small antennas, with corresponding enhanced resolution. For example, the "Soil Moisture and Ocean Salinity" (SMOS) satellite is an interferometer with a Y-shaped array of 69 antennas where

[*] saban-emre.koese@uni-tuebingen.de
[†] daniel.braun@uni-tuebingen.de

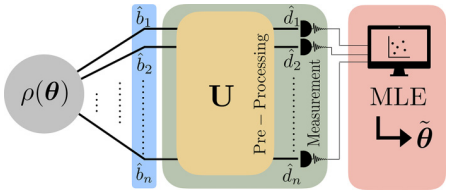

FIG. 1. The Gaussian state $\rho(\boldsymbol{\theta})$ of the n-mode interferometer contains the spatial and the radiometric information from current density sources. The incoming modes $\hat{b}_i$ are combined with an optimized $\mathbf{U}$ to have detection modes $\hat{d}_i$ of the photon counting measurement. For experimental realization, one can decompose $\mathbf{U}$ into $SU(2)$ group elements similar to optical quantum computing, i.e., using beam splitters and phase shifters. After the measurements, one estimates the parameter set using an estimator function such as a maximum likelihood estimator (MLE).

each arm has a length of around 4 m [48–51]. It achieves a resolution of about $d \simeq 35$ km, from a distance $R \simeq 758$ km above the surface of Earth by measuring the thermal noise in a narrow frequency band of electromagnetic fields (1420–1427 MHz, central wavelength $\lambda \simeq 21$ cm). The electric fields are sampled in real time, filtered, and interfered numerically, implementing thus purely classical interference. The diffraction limit analogous to the ones by Abbe and Rayleigh is given here by the van Cittert–Zernike theorem [52–54], $d \simeq \lambda R/\Delta x_{ij}$, where Δx_{ij} is the maximal spatial separation between two antennas. From the interferometric data one can, via inverse spatial Fourier transform, estimate the local brightness temperatures T_{eff} on the surface of Earth with resolution d, and from these, with appropriate models, the soil moisture and ocean salinity. This information is of great importance for the geosciences, monitoring of Earth, climate modeling, flood predictions, and much more. Driven by these applications, there is the desire to enhance the spatial resolution but simply increasing the size of the satellite becomes unpractical and lowering its orbit reduces its lifetime.

Here we show that with appropriate techniques from multiparameter quantum estimation theory, one can reconstruct images of Earth with roughly a factor 10 better spatial resolution than SMOS with a satellite of comparable size. We demonstrate this with images of up to 30 pixels, showing that they can be reconstructed faithfully with a pixel size of 3 km. Instead of local measurement of the incoming modes of the interferometer, we combine the modes with a unitary transformation that enables nonlocal measurements. We find the optimal unitary matrix that minimizes the scalar classical Cramér-Rao bound (CCRB) [55] for the classical Fisher information matrix for the chosen measurements contracted with a weight matrix. The corresponding unitary matrix can be decomposed into phase shifters and, at most, $n(n-1)/2$ beam splitters, as is well known from linear optical quantum computing [56]. This allows us to quantum program optimal measurement schemes for imaging. Contrary to classical computational imaging [1], the quantum computation for this new kind of "quantum-computational imaging" is done before the measurements (see Fig. 1).

Multiparameter quantum estimation theory is by itself a rapidly evolving field. Recently, there have been many different works, e.g., multiparameter estimation of several phases [43], estimation of all three components of a magnetic field [57], optimal estimation of the Bloch vector components of a qubit [58], multiparameter estimation from Markovian dynamics [59], etc. (see the review article [60]). For a limited sample size, like in passive sensing, it is crucial to estimate the image's parameters simultaneously. The multiparameter quantum Cramér-Rao bound (QCRB) can, in general, not be saturated. Optimal measurements linked to different parameters do not typically commute and hence lead to incompatible measurements. Once the commutation on average is satisfied, the quantum limit is asymptotically attainable [61].

We build on our previous work [47,54,62], where we showed that thermal fluctuations of the microscopic currents lead to Gaussian states of the microwave field and hence allow one to use the QCRB for Gaussian states [10,11,63,64]. As before, we assume that only the current densities at the surface of Earth contribute and neglect the cosmic microwave background as well as additional technical noises [65–67].

We organize the rest of the paper as follows. In Sec. II, we introduce the quantum state received by the n-mode interferometer, as well as the QFI, the symmetric logarithmic derivative (SLD), and the corresponding quantum Cramér-Rao lower bound. Further, we present the optimal positive operator-valued measure (POVM), which minimizes the most informative bound for the multiparameter estimation. In Sec. III, first, we discuss the simple problem as a benchmark considering two-pixel sources with the two-mode interferometer. We analyze the quantum advantage with the optimal unitary compared to local measurement scenarios. Second, we increase the number of pixels by considering a one-dimensional (1D) array of sources with a 1D array interferometer. We examine how closely we can approach the quantum limit of sensitivity with our parameter set. Third, we consider a two-dimensional (2D) source image with a 2D array interferometer. Using the maximum likelihood estimator (MLE), we reconstruct the image for the POVMs with the optimized unitary specific to the image, the optimized unitary for uniform temperature distribution, and local measurements. We conclude in Sec. IV.

II. THEORY

A. State received by the n-mode interferometer

In previous work [47], we analyzed the quantum state radiated from current current distribution $\mathbf{j}(\mathbf{r}, t)$ [62,68–77] on the source plane. We show that the state of the incoming modes of the n-mode interferometer from these radiated sources can be modeled as circularly symmetric Gaussian states with a partial coherence, which encodes the information of position and amplitudes distribution of the sources. Then after the scattering process [78,79] from the interferometer, the partially coherent state received in the n modes is represented by

$$\rho = \int d^{2n}\beta \Phi(\{\beta_i\}) |\{\beta_i\}\rangle\langle\{\beta_i\}|, \tag{1}$$

where $|\{\beta_i\}\rangle$ is a multimode coherent state for spatial antenna modes, $\{\beta_i\} = \beta_1, \beta_2, \ldots, \beta_n$, and

$$\Phi(\{\beta_i\}) = \frac{1}{\pi^n \det \Gamma} e^{-\bar{\beta}^\dagger \Gamma^{-1} \bar{\beta}}, \tag{2}$$

where $\bar{\beta}^T = (\beta_1, \beta_2, \ldots, \beta_n)$ is the Sudarshan-Glauber representation, and $d^{2n}\beta \equiv d\mathrm{Re}\beta_1 d\mathrm{Im}\beta_1 \ldots d\mathrm{Re}\beta_n d\mathrm{Im}\beta_n$. The matrix Γ is the coherence matrix for n antenna modes, and its elements are defined as $\Gamma_{ij} = \langle \hat{b}_i^\dagger \hat{b}_j \rangle$. Considering the sources of these fields are generated by random current distribution on the source plane and assuming that each antenna has the same polarization direction $\hat{e}_l$ and they filter incoming fields with the same frequency ω_0 with a bandwidth B, then one finds a relation between $\langle b_i^\dagger b_j \rangle$ and the average current density distribution on the source plane as [47]

$$\langle \hat{b}_i^\dagger \hat{b}_j \rangle = K \int d^3r \, \frac{\langle |\tilde{\mathcal{J}}_{t,l}(\mathbf{r},\omega)|^2 \rangle \, e^{i\omega_0(|\mathbf{r}-\mathbf{r}_j|-|\mathbf{r}-\mathbf{r}_i|)/c}}{|\mathbf{r}-\mathbf{r}_i||\mathbf{r}-\mathbf{r}_j|} \times \mathrm{sinc}\left[\frac{B}{2c}(|\mathbf{r}-\mathbf{r}_j| - |\mathbf{r}-\mathbf{r}_i|)\right], \tag{3}$$

where d^3r is the integral over the source volume, $\mathbf{r}_i$ is the location of the detector for received modes in the detection plane, and $\mathrm{sinc}(x) = \sin(x)/x$. $\tilde{\mathcal{J}}_{t,l}(\mathbf{r},\omega)$ is the Fourier transform of the locally transverse component of the current density $\mathcal{J}(\mathbf{r},t)$ and l stands for the component parallel to the source plane. Considering R as the distance between source and detection planes, we can parametrize the integral over Earth's surface as $\mathbf{r} = (x, y, R)$ with respect to the coordinate system of the detection plane. Assuming that we are in the far-field regime $|\Delta\mathbf{r}_{ij}| \ll R$, where $\Delta\mathbf{r}_{ij} = \mathbf{r}_j - \mathbf{r}_i$ is the distance between two antennas, we approximate $|\mathbf{r}-\mathbf{r}_j| - |\mathbf{r}-\mathbf{r}_i| \approx \Delta\mathbf{r}_{ij}\cdot\mathbf{r}/|\mathbf{r}|$. In the denominator, we approximate $|\mathbf{r}-\mathbf{r}_i| \approx R/\cos\tilde{\theta}(x,y)$ with $\tilde{\theta}(x,y)$ the polar angle between the z axis and the vector (x, y, R). We find the relation of the average amplitude of current density distribution to brightness temperature as $T_\mathrm{B}(x,y)$ by $\langle |\tilde{\mathcal{J}}_{t,i}(\mathbf{r},\omega)|^2 \rangle = K_1 T_\mathrm{B}(x,y)\cos\tilde{\theta}(x,y)\delta(z-R)$, where $K_1 = 32\tau_c k_B/(3l_c^3\mu_0 c)$. Further, one can define the effective temperature as $T_\mathrm{eff}(x,y) \equiv T_\mathrm{B}(x,y)\cos^3\tilde{\theta}(x,y)$. We include an extra constant prefactor μ for the additional losses, which can be justified by tracing out modes of losses $\hat{c}$ into which photons might scatter by writing $\hat{b} = \sqrt{\mu}\hat{\tilde{b}} + \sqrt{1-\mu}\hat{c}$. Compared to the actual physical temperature, the brilliance temperature is additionally modified by the albedo of the surface from which important information, such as the surface's water content or the ocean water's salinity, can be extracted. For simplicity, we work with the physical temperatures in the following, i.e., set $T_B(x,y) = T(x,y)$. Following these assumptions and dropping the $\sim$ from $\hat{\tilde{b}}$, we simplify Eq. (3) as

$$\langle \hat{b}_i^\dagger \hat{b}_j \rangle = \frac{\mu\kappa}{R^2} \int dxdy \, T_\mathrm{eff}(x,y) e^{2\pi i(v_x^{ij}x + v_y^{ij}y)}. \tag{4}$$

We introduced a new constant $\kappa = K_1 K \equiv 2k_B/(\pi\hbar\omega_0)$ where κ has the dimension of inverse temperature with SI units (1/K) and $v_y^{ij} = \Delta x_{ij}/(\lambda R)$, $v_x^{ij} = \Delta y_{ij}/(\lambda R)$ with $\omega_0/c = 2\pi/\lambda$. Considering the parameters of SMOS, we find $\kappa = 9.4$ 1/K. The SMOS has a Y shape where each arm has a length of almost 4 m. Therefore, it is reasonable to set maximum baselines $\Delta x_\mathrm{max} = \Delta y_\mathrm{max}$ around 10 m.

B. Estimation theory of the sources

1. Quantum Cramér-Rao bound

For a quantum state $\rho_{\boldsymbol{\theta}}$ that depends on a vector of l parameters $\boldsymbol{\theta} = (\theta_1, \theta_2, \ldots, \theta_l)^T$, an ultimate lower bound of an unbiased estimator of the parameter set is given by the quantum Cramér-Rao bound (CRB), which states that the covariance matrix of any such estimator is equal to or greater than the inverse of the QFI matrix (in the sense that their difference is a positive-semidefinite matrix). The CCRB from measurement is lower bounded by the QCRB [6,7,60] given by

$$\mathrm{Cov}(\tilde{\boldsymbol{\theta}}) \geqslant \mathscr{F}(\boldsymbol{\theta})^{-1}, \quad \mathscr{F}_{ij}(\boldsymbol{\theta}) = \tfrac{1}{2}\mathrm{Tr}(\rho_{\boldsymbol{\theta}}\{\mathscr{L}_i, \mathscr{L}_j\}), \tag{5}$$

where $\mathrm{Cov}(\tilde{\boldsymbol{\theta}})$ is a covariance matrix for the locally unbiased estimator $\tilde{\boldsymbol{\theta}}$ [61,80], the $\{\cdot,\cdot\}$ means the anticommutator, and $\mathscr{L}_i$ is the SLD related to parameter i, which is defined similarly to the single parameter case, $\frac{1}{2}(\mathscr{L}_i\rho_{\boldsymbol{\theta}} + \rho_{\boldsymbol{\theta}}\mathscr{L}_i) = \partial_i\rho_{\boldsymbol{\theta}}$. The SLD and the elements of the QFI matrix are given in Ref. [81] for any Gaussian state. The SLD can be written as

$$\mathscr{L}_i = \tfrac{1}{2}\mathfrak{M}^{-1}_{\alpha\beta,\gamma\delta}(\partial_i\Sigma^{\gamma\delta})(\mathbf{b}^\alpha\mathbf{b}^\beta - \Sigma^{\alpha\beta}), \tag{6}$$

where $\mathfrak{M}^{-1}_{\alpha\beta,\gamma\delta}$ is the fourth-order tensor form of the inverse of the matrix $\mathfrak{M} \equiv \Sigma\otimes\Sigma + \frac{1}{4}\Omega\otimes\Omega$, with $\Omega = \bigoplus_{k=1}^n i\sigma_y$, and the summation convention is used for repeated indices. In our case, the mean displacement of the Gaussian state is zero. Covariance matrix elements are given by $\Sigma^{\alpha\beta} = \frac{1}{2}\mathrm{Tr}[\rho(\mathbf{b}^\alpha\mathbf{b}^\beta + \mathbf{b}^\beta\mathbf{b}^\alpha)]$, with $\mathbf{b} = [b_1, b_1^\dagger, b_2, b_2^\dagger, \ldots, b_n, b_n^\dagger]$ [10,81–85]. Then the elements of the QFI matrix in [81] become

$$\mathscr{F}_{ij} = \tfrac{1}{2}\mathfrak{M}^{-1}_{\alpha\beta,\gamma\delta}\partial_j\Sigma^{\alpha\beta}\partial_i\Sigma^{\gamma\delta}. \tag{7}$$

Using the properties of the Gaussian state (circularly symmetric and with zero mean) we can write the SLD for n mode interferometers as [47]

$$\mathscr{L}_i = \sum_j^n g_i^j \hat{b}_j^\dagger\hat{b}_j + \sum_{j<k}^n \left[g_i^{jk}\hat{b}_j^\dagger\hat{b}_k + (g_i^{jk})^*\hat{b}_k^\dagger\hat{b}_j\right] + C, \tag{8}$$

where C is a constant term that can be dropped for diagonalization purposes. In the single parameter case, the optimal POVM is the set of projectors onto eigenstates of $\mathscr{L}_i$. It allows one to saturate the QCRB in the limit of infinitely many measurements using maximum likelihood estimation [6,86,87]. To find the POVMs from the SLD, we construct a Hermitian matrix $\mathbf{M}_i$ whose diagonal elements are real-valued functions which are defined as $g_i^j \equiv \mathfrak{M}^{-1}_{\alpha\beta,\gamma\delta}(\partial_i\Sigma^{\gamma\delta})$ with $\alpha = 2j$ and $\beta = 2j-1$. The off-diagonal elements are complex-valued functions and defined as $g_i^{jk} = \mathfrak{M}^{-1}_{\alpha\beta,\gamma\delta}(\partial_i\Sigma^{\gamma\delta})$ with $\alpha = 2j$ and $\beta = 2k-1$ and $k > j$. By introducing a new set for the field operators such that $\bar{\mathbf{b}}^\dagger \equiv [\hat{b}_1^\dagger, \hat{b}_2^\dagger, \ldots, \hat{b}_n^\dagger]$ and $\bar{\mathbf{b}} \equiv [\hat{b}_1, \hat{b}_2, \ldots, \hat{b}_n]^T$, we write the SLD in the following form:

$$\mathscr{L}_i = \bar{\mathbf{b}}^\dagger\mathbf{M}_i\bar{\mathbf{b}}. \tag{9}$$

As $\mathbf{M}_i$ is a Hermitian matrix it can be unitarily diagonalized by $\mathbf{M}_i = \mathbf{V}_i^\dagger\mathbf{D}_i\mathbf{V}_i$ with $\mathbf{V}_i^\dagger\mathbf{V}_i = \mathbb{I}$. A new set of operators can be defined as $\bar{\mathbf{d}}_i^\dagger = \bar{\mathbf{b}}^\dagger\mathbf{V}_i^\dagger$ where $\bar{\mathbf{d}}_i^\dagger = [\hat{d}_{i1}^\dagger, \hat{d}_{i2}^\dagger, \ldots, \hat{d}_{in}^\dagger]$. The optimal POVM for the single parameter case ($i = 1$, which we drop in the following)

can be found as a set of projectors in the Fock basis $\{|m_1, m_2, \ldots, m_n\rangle \langle m_1, m_2, \ldots, m_n|\}_{\{m_1,m_2,\ldots,m_n\}}$ of the $\hat{d}_l$ with $\hat{d}_l^\dagger \hat{d}_l |m_1, m_2, \ldots, m_n\rangle = m_l |m_1, m_2, \ldots, m_n\rangle$, where $l \in \{1, \ldots, n\}$. The $\hat{d}_l$ will be called "detection modes." By introducing a positive weight matrix $\boldsymbol{w}$, one can define the scalar inequalities from the matrix valued QCRB as $\mathrm{Tr}[\boldsymbol{w}\,\mathrm{Cov}(\tilde{\boldsymbol{\theta}})] \geqslant \mathrm{Tr}(\boldsymbol{w}\mathscr{F}(\boldsymbol{\theta})^{-1}) \equiv C^S(\boldsymbol{\theta}, \boldsymbol{w})$. Contrary to the single parameter case, the multiparameter QCRB can generally not be saturated. Holevo realized this problem and proposed a tighter and more fundamental bound [88] $C^H(\boldsymbol{\theta}, \boldsymbol{w})$, which is upper bounded by $2C^S(\boldsymbol{\theta}, \boldsymbol{w})$ [55,89]. If the SLD operators for different parameters commute on average $\mathrm{Tr}(\rho_{\boldsymbol{\theta}}[L_i, L_j]) = 0$, then the Holevo-CRB is equivalent to the QCRB, and the QCRB for multiparameter estimation can be saturated asymptotically with a collective measurement in the limit of an infinitely large number of copies $\rho_{\boldsymbol{\theta}}^{\otimes N}$ [55,61]. The standard deviation of the estimator decreases proportionally to $1/\sqrt{N}$ for the sample size of N. The SMOS satellite travels at a constant speed of around $v \simeq 7$ km/s. It takes time $\tau = L/v$ to fly at a distance L. Each sample has a lower bound for the detection time given by $t_D \simeq 1/B$. In practice, the practical detection time might be much larger due to, e.g., deadtimes of the sensors, slow electronics, etc. In addition, zero temperature of the detector and modes $\hat{b}_i$ is implicitly assumed in our calculations but would require cooling down to temperatures much smaller than $\hbar\omega_0$. If the actual detection time is t_D^{eff}, the maximum sample size becomes $N = \tau/t_D^{\mathrm{eff}}$.

2. *Most informative bound for multiparameter metrology*

The most informative bound minimizes the classical scalar Cramér-Rao bound over all the possible POVMs. In the single parameter case, from the diagonalization of the SLD, we see that one needs to combine the incoming modes with a unitary transformation to saturate the QCRB single parameter case. This transformation, even for a single parameter, depends on the parameter itself. In the multiparameter case, any of these specific unitary transformations for a specific parameter usually gives a more significant mean-square error for the remaining parameters. Using the clue from the SLD structure, we drop the index i from the unitary transformation of the modes and minimize the scalar bound of the classical Fisher information matrix for multiparameter estimation over all possible unitaries. Then, a new set of operators for the detection modes can be defined as $\bar{\mathbf{d}} = \mathbf{U}\bar{\mathbf{b}}$ where $\bar{\mathbf{d}}^T = [\hat{d}_1, \hat{d}_2, \ldots, \hat{d}_n]$, where $\mathbf{U}$ is the corresponding unitary transformation of the field modes. The average values of the elements of the new coherence matrix $\tilde{\Gamma}$ can be found by using $\hat{d}_i = \sum_l U_{il}\hat{b}_l$ as

$$\tilde{\Gamma}_{ij} = \langle d_i^\dagger d_j\rangle = \sum_{kl} U_{ik}^* U_{jl} \langle b_k^\dagger b_l\rangle. \tag{10}$$

Then we will have the probabilities after measurement $P(m_1, ..m_n|\theta_1, \theta_2, \ldots, \theta_l)$ as

$$\begin{aligned} P(\{m_k\}|\boldsymbol{\theta}) &= \int d^{2n}\delta\tilde{\Phi}(\{\delta_i\})|\langle\{m_k\}|\{\delta_i\}\rangle|^2 \\ &= \int d^{2n}\delta\tilde{\Phi}(\{\delta_i\}) \prod_i e^{-|\delta_i|^2}\frac{|\delta_i|^{2m_i}}{m_i!}, \end{aligned} \tag{11}$$

where $|\{\delta_i\}\rangle$ is a coherent state of the detection modes and $\tilde{\Phi}(\{\delta_i\})$ is the Sudarshan-Glauber function for the state of the detection modes. Due to the linear transformation from $\bar{\mathbf{b}}$ to $\bar{\mathbf{d}}$, it is still a Gaussian. It is difficult to evaluate the integral of $P(\{m_k\}|\boldsymbol{\theta})$ for all possible values of m_k and keep track of all possible combinations of photon number counts, both numerically and experimentally. Hence, instead of considering projections on the complete Fock basis as POVMs, we choose the POVMs with at most one photon per measurement and limit ourselves to $\sum_k m_k \leqslant 1$. Clearly, the resulting information loss is negligible for light that, from the very beginning, is very faint, with at most one photon per mode. However, it can be important for stronger light sources, for which one should try to resolve the photon numbers. We have the order of ten photons per mode for thermal microwave sources at room temperature. We see below that even without resolving their number, we can already largely surpass the classical resolution limit, but there is room for further improvement by going beyond the single-photon detection scheme we analyze in the following.

The selected POVM elements of single-photon detection are

$$\begin{aligned} \Pi_0 &= |0, 0, \ldots, 0\rangle \langle 0, 0, \ldots, 0|, \\ \Pi_k &= |0, 0, \ldots, 1_k, \ldots, 0\rangle \langle 0, 0, \ldots, 1_k, \ldots, 0|, \\ \Pi_{n+1} &= \mathbb{I} - \sum_{l=0}^{n} \Pi_l, \end{aligned} \tag{12}$$

where the last element $(n+1)$ ensures $\sum_{l=0}^{n+1}\Pi_l = \mathbb{I}$. The measurement probability of no photon in any interferometer mode becomes

$$\begin{aligned} P_0(\boldsymbol{\theta}) &= \frac{1}{\pi^n \det\tilde{\Gamma}} \int d^{2n}\delta e^{-\boldsymbol{\delta}^\dagger(\tilde{\Gamma}^{-1}+\mathbb{I})\boldsymbol{\delta}} \\ &= \frac{1}{\det(\tilde{\Gamma}+\mathbb{I})}. \end{aligned} \tag{13}$$

The single-photon detection probabilities in each mode of the interferometer follow as

$$\begin{aligned} P_k(\boldsymbol{\theta}) &= \frac{1}{\pi^n \det\tilde{\Gamma}} \int d^{2n}\delta e^{-\boldsymbol{\delta}^\dagger(\tilde{\Gamma}^{-1}+\mathbb{I})\boldsymbol{\delta}}|\delta_k|^2 \\ &= \frac{[(\tilde{\Gamma}^{-1}+\mathbb{I})^{-1}]_{kk}}{\det(\tilde{\Gamma}+\mathbb{I})}. \end{aligned} \tag{14}$$

The probability to find more than a single photon per measurement can be found as

$$P_{n+1}(\boldsymbol{\theta}) = \mathbb{I} - \sum_{k=0}^{n} P_k. \tag{15}$$

We also show the first derivative of the probability distributions of no photon detection from measurements analytically to be given by

$$\frac{\partial P_0(\boldsymbol{\theta})}{\partial\theta_i} = \left(\frac{1}{\det(\tilde{\Gamma}+\mathbb{I})}\right) \mathrm{Tr}\left(-(\tilde{\Gamma}+\mathbb{I})^{-1}\frac{\partial\tilde{\Gamma}}{\partial\theta_i}\right). \tag{16}$$

The first derivative for at most single-photon detection for all modes becomes

$$\frac{\partial P_k(\boldsymbol{\theta})}{\partial \theta_i} = \left(\frac{1}{\det(\tilde{\Gamma}+\mathbb{I})}\right) \times \left\{\left[(\tilde{\Gamma}^{-1}+\mathbb{I})^{-1}\tilde{\Gamma}^{-1}\frac{\partial \tilde{\Gamma}}{\partial \theta_i}\tilde{\Gamma}^{-1}(\tilde{\Gamma}^{-1}+\mathbb{I})^{-1}\right]_{kk} - [(\tilde{\Gamma}^{-1}+\mathbb{I})^{-1}]_{kk}\,\mathrm{Tr}\left((\tilde{\Gamma}+\mathbb{I})^{-1}\frac{\partial \tilde{\Gamma}}{\partial \theta_i}\right)\right\}. \quad (17)$$

Finally, using Eqs. (13)–(17), the elements of the classical Fisher information can be found from

$$\mathcal{F}_{ij} = \sum_{l}^{n+1} \frac{1}{P_l(\boldsymbol{\theta})}\frac{\partial P_l(\boldsymbol{\theta})}{\partial \theta_i}\frac{\partial P_l(\boldsymbol{\theta})}{\partial \theta_j}. \quad (18)$$

The most informative bound [55] in this case is the bound minimized over all possible unitary matrices:

$$\mathrm{Tr}[\boldsymbol{w}\,\mathrm{Cov}(\tilde{\boldsymbol{\theta}})] \geqslant \min_{\mathbf{U}}\{\mathrm{Tr}[\boldsymbol{w}\mathcal{F}^{-1}(\boldsymbol{\theta})]\}. \quad (19)$$

The weight matrix is a positive definite matrix to satisfy the scalar Cramér-Rao bound. For simplicity, we consider $\boldsymbol{w} = \mathbb{I}$ to optimize the average variance of all parameters. One can also consider a diagonal matrix with different weights. This will result in directly decreasing the variances of preferred estimators. Further, choosing a weight matrix with off-diagonal elements includes covariances of the estimators. Since we assume spatially uncorrelated currents, we focus here for simplicity on the temperatures, with equal weight, rather than their correlations, which is also a preferred choice in the literature (see Ref. [55]).

3. Maximum likelihood estimation

Maximum likelihood estimators are widely used in estimation theory and play an essential role in interpreting the Cramér-Rao theorem [90,91]. One can estimate the set of parameters with a given probability distribution with some observed data. The likelihood function is given by $l(\boldsymbol{\theta}) = \prod_k^{n+1}(P_k(\boldsymbol{\theta}))^{N_k}$, where the total number of samples is given by $N = \sum_k^{n+1} N_k$ with N_k realizations of outcome k. Since the logarithm is a monotonously increasing function, the log of the likelihood function is maximized by the same parameter vector $\boldsymbol{\theta}$. Thus, the MLE $\hat{\boldsymbol{\theta}}_{\mathrm{MLE}}$ is a value of $\boldsymbol{\theta}$ that maximizes the log likelihood $\mathcal{L}(\boldsymbol{\theta}) = \ln[l(\boldsymbol{\theta})]$,

$$\hat{\boldsymbol{\theta}}_{\mathrm{MLE}} = \arg\max_{\boldsymbol{\theta}\in\Theta}\mathcal{L}(\boldsymbol{\theta}), \quad (20)$$

where the max is taken over the entire parameter space Θ. For sufficiently large sample size, $N \to \infty$, $\hat{\boldsymbol{\theta}}_{\mathrm{MLE}}$ converges to the true value of the parameter set $\boldsymbol{\theta}$.

III. RESULTS: ESTIMATION OF SOURCE TEMPERATURES

In this paper, our purpose is to estimate the function $T(x, y)$. Equation (4) allows us to study any source distribution on the source plane. For that aim, we partition the electromagnetic field's source on Earth's surface into square pixels of size a and effective pixel temperature T_i, located under the interferometer in the x, y plane at a distance R from the satellite. Thus, we are interested in estimating the temperature distribution in the form

$$T_{\mathrm{eff}}(x, y) = \sum_i T_i \mathrm{Box}(x - x_i, y - y_i), \quad (21)$$

where $\mathrm{Box}(x, y)$ is defined as

$$\mathrm{Box}(x, y) \triangleq \begin{cases} 1 & |x| \leqslant \frac{a}{2} \quad \text{and} \quad |y| \leqslant \frac{a}{2} \\ 0 & \text{else} \end{cases}. \quad (22)$$

Of course, this is a choice to simplify our problem to a limited number of parameters. One could also describe $T(x, y)$ using different temperature distribution functions such as Gaussian and define the parameter set according to this choice. Further, we estimate the effective pixel temperatures T_i, assuming that all the other parameters are known to a sufficiently large precision. The diagonal elements of the coherence matrix (Γ) of Gaussian states become

$$\langle \hat{b}_k^\dagger \hat{b}_k \rangle = \frac{\mu\kappa a^2}{R^2}\sum_i^p T_i, \quad (23)$$

and the off-diagonal elements are

$$\langle \hat{b}_k^\dagger \hat{b}_l \rangle = \frac{\mu\kappa a^2 \eta_{kl}}{R^2}\sum_i^p T_i e^{2\pi i(v_{kl}^x x_i + v_{kl}^y y_i)}, \quad (24)$$

where $k \neq l$ and we defined $\eta_{kl} \equiv \mathrm{sinc}(v_{kl}^x a)\,\mathrm{sinc}(v_{kl}^y a)$. The number of pixels along the $\hat{x}$ and $\hat{y}$ axis is p_x and p_y, respectively, and the number of detection modes along these axes is n_x and n_y, respectively. In total, we have $p = p_x p_y$ pixels on the surface and $n = n_x n_y$ detectors in the detection plane, of which each measures one detection mode. We set the number of detection modes equal to the number of pixels in the source plane, $n = p$, to leave no redundant parameter for the estimation, and use $n_x = p_x$ and $n_y = p_y$.

A. Resolution of two pixel sources

Let us start with two pixels (pixel 1 and pixel 2) with temperatures T_1 and T_2 in the source plane with pixel size a. Our goal is to estimate the temperatures of each source. We set the central locations of these two sources in the source plane to $(-a/2, 0, R)$ and $(a/2, 0, R)$, i.e., both are on an axis parallel to the $\hat{x}$ axis without any distance between them. In the detection plane, we have two detection modes $\hat{d}_1$ and $\hat{d}_2$ with detectors centered at positions $(-\Delta x/2, 0, 0)$ and $(\Delta x/2, 0, 0)$ on the $\hat{x}$ axis, respectively. In our previous work [47], we showed that if the mean photon numbers in each received mode of the two-mode interferometer, with circular symmetric Gaussian state, are identical ($\langle b_1^\dagger b_1\rangle = \langle b_2^\dagger b_2\rangle$), then the SLDs for T_1 and T_2 commute on average $\mathrm{Tr}(\rho_{\boldsymbol{\theta}}[L_i, L_j]) = 0$. Thus the QCRB and Holevo-CRB are equivalent: $C^S(\boldsymbol{\theta}, \boldsymbol{w}) \equiv C^H(\boldsymbol{\theta}, \boldsymbol{w})$. For each parameter, the matrix $\mathbf{M}_i$ from the SLD with $i \in \{T_1, T_2\}$ is of the form

$$\mathbf{M}_i = \begin{bmatrix} g_1^i & |g_2^i|e^{i\phi_i} \\ |g_2^i|e^{-i\phi_i} & g_1^i \end{bmatrix}, \quad (25)$$

where the ϕ_i, in general, depend on both T_1 and T_2. The ϕ_1 and ϕ_2 differ for single parameter estimation of T_1 and T_2. The

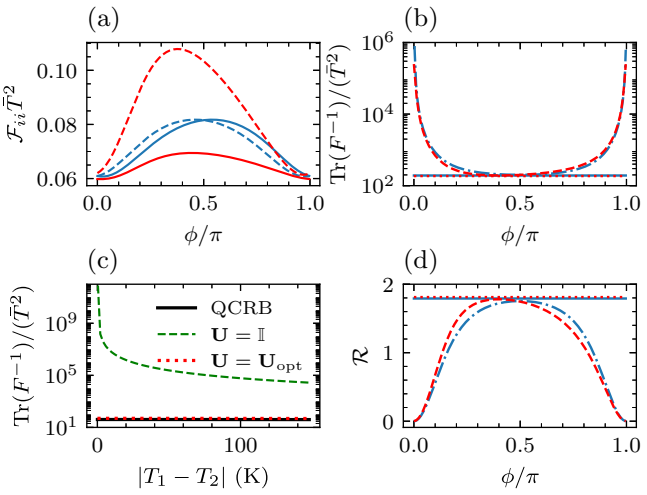

FIG. 2. Temperature estimation of two pixels. (a) The diagonal elements of the Fisher information matrix (dimensionless) as a function of ϕ. The dashed curves are for $\mathcal{F}_{T_1}$, and solid curves are for $\mathcal{F}_{T_2}$. (b) The scalar CRBs as a function of ϕ scaled with the average temperature $\bar{T}$ square of the sources. The flat lines are for the QCRBs, and the others are the CCRBs for the measurement. (c) The scalar CRBs as a function of the temperature difference of two pixels. Solid black is for QCRB, red dotted is for CCRB for optimized ϕ, and the green dashed curve is for the scalar CCRB for local measurement considering $\mathbf{U} = \mathbb{I}$. (d) The gain factor of the estimate $\mathcal{R}$ as a function of ϕ. The flat lines are from the QCRBs, and the others are the CCRBs from the measurement. In figures (a), (b), and (d), the blue curves are for uniform temperature, $T_1 = T_2 = 300$ K, and red curves are for nonuniform temperatures, $T_1 = 400$ K and $T_2 = 200$ K. The source size is $a = 4$ km. The average temperature in all figures is $\bar{T} = 300$ K and $\mu = 0.5$.

unitary that diagonalizes each SLD is found as

$$\mathbf{U}_i = \frac{1}{\sqrt{2}}\begin{bmatrix} 1 & e^{i\phi_i} \\ 1 & -e^{i\phi_i} \end{bmatrix}. \tag{26}$$

Since the unitary is parametrized with a single parameter, we can drop the index i and find the ϕ that gives the most informative bound for joint estimation of both T_1 and T_2. In Fig. 2(a), we plot the diagonal elements of the classical Fisher information (CFI) matrix in Eq. (18) as a function of ϕ. If T_1 (dashed) and T_2 (solid) are equal, $T_1 = T_2$ (blue lines), a diagonal element $\mathcal{F}_1$ or $\mathcal{F}_2$ can be obtained by mirroring the other with respect to $\phi = \pi/2$. For different temperatures, $T_1 > T_2$ (red lines), the CFI matrix elements are not symmetric anymore. We observe that $\max(\mathcal{F}_1) > \max(\mathcal{F}_2)$, and their difference is related to temperature changes, which means that we can estimate the pixel with higher temperature better. We keep the average temperature ($\bar{T}$) constant. In both cases, we have the maximum value of CFI matrix elements $\max(\mathcal{F}_1) = \max(\mathcal{F}_2)$ at different ϕ and diagonalize the SLD for each parameter for single parameter estimation.

In Fig. 2(b), we plot $\mathrm{Tr}(F^{-1})/(\bar{T}^2)$ as a function of ϕ for $T_1 = T_2$ (blue) and $T_1 > T_2$ (red) temperature configurations. The scalar QCRBs are given by solid blue ($T_1 = T_2$) and dotted red ($T_1 > T_2$) flat lines, respectively. We see that for $T_1 = T_2$ (dot-dashed blue curve), we have the minimum of the scalar CCRB at $\phi = 0.5\pi$, and for $T_1 > T_2$ (dashed red curve), the minimum value is slightly shifted to the left. In both cases, the QCRBs are saturated. We see that the magnitudes of scalar QCRBs for $T_1 = T_2$ and $T_1 > T_2$ are close to each other if we keep the same $\bar{T}$ in both configurations. We also observe that $\mathrm{Tr}(\mathcal{F}^{-1})/(\bar{T}^2)$ for $T_1 > T_2$ (dashed red curve) at $\phi = \pi/2$ is still close to the QCRB (red dotted flat line). Even though to saturate the QCRB, ϕ must depend on the temperatures of all pixels, one can find the ϕ for $T_1 = T_2 = \bar{T}$ and use it to estimate different temperature configurations ($T_1 > T_2$).

In Fig. 2(c), we compare the most informative bound for optimal ϕ with the CCRB of local measurement (i.e., $\mathbf{U} = \mathbb{I}$) for joint estimation of T_1 and T_2 for a single measurement. We see that the dimensionless CCRB for the local measurement (green dashed line) goes to ∞ when the two sources have the same temperature. For a temperature difference around $\approx$10 K, it is around $\approx 10^6$, which is almost $\approx 10^4$ times larger than for an optimal nonlocal measurement using $\mathbf{U}_{\rm opt}$ (red dotted line). We also see that the optimal unitary saturates the QCRBs (solid black line). The bounds given in Fig. 2 are for a single measurement ($N = 1$) and reduced by a factor N for N independent measurements.

One can wonder what is the advantage of joint estimation of parameters over single parameter estimation. To answer that question, we can define the gain factor of the joint estimate [92,93]:

$$\mathcal{R} = p\sum_i^p \frac{1/F_{ii}}{\mathrm{Tr}\,(F^{-1})}, \tag{27}$$

where p is the total number of the parameters we want to estimate. The F stands for both the QFI matrix $\mathscr{F}$ and the CFI matrix $\mathcal{F}$. The gain factor $\mathcal{R}$ is upper bounded by p ($0 < \mathcal{R} \leqslant p$), where the factor p arises from the fact that for p single parameter estimations, the number of samples available for each parameter is reduced by a factor p compared to the total sample size, as different optimal measurements are typically required for different parameters. Since we have only two parameters to estimate (T_1 and T_2), the upper bound of the gain factor becomes $\mathcal{R} \leqslant 2$. If the gain factor is smaller than 1, $\mathcal{R} < 1$, then we do not have any advantage from joint estimation. In Fig. 2(d), we show the gain factor $\mathcal{R}$ of the estimation as a function of ϕ. It is close to 2 for the scalar QCRBs of $T_1 = T_2$ (solid blue) and $T_1 > T_2$ (dotted red straight lines). Furthermore, this advantage is achieved by the optimized unitary for CCRBs of $T_1 = T_2$ (dot-dashed blue curve) and $T_1 > T_2$ (dashed red curve). We have almost twice the advantage compared to single parameter estimation.

B. Resolution of a 1D array of pixel sources

We next consider a 1D array of pixels aligned parallel to the detector modes on the $\hat{x}$ axis ($p_x = n_x$ and $p_y = n_y = 1$). The size a of a pixel is the same for all pixels, and the separation between the two nearest pixels vanishes. The central position of each pixel is given by $\tilde{x}_j = (2j - p_x - 1)a/2$, and the position of detector k is $x_k = (2k - n_x - 1)\Delta x_{\max}/n_x$, where $j \in \{1, \ldots, p_x\}$ and $k \in \{1, \ldots, n_x\}$. The parameters that we want to estimate are the temperatures of each pixel given by a vector $\boldsymbol{\theta} = \{T_1, T_2, \ldots, T_{p_x}\}$.

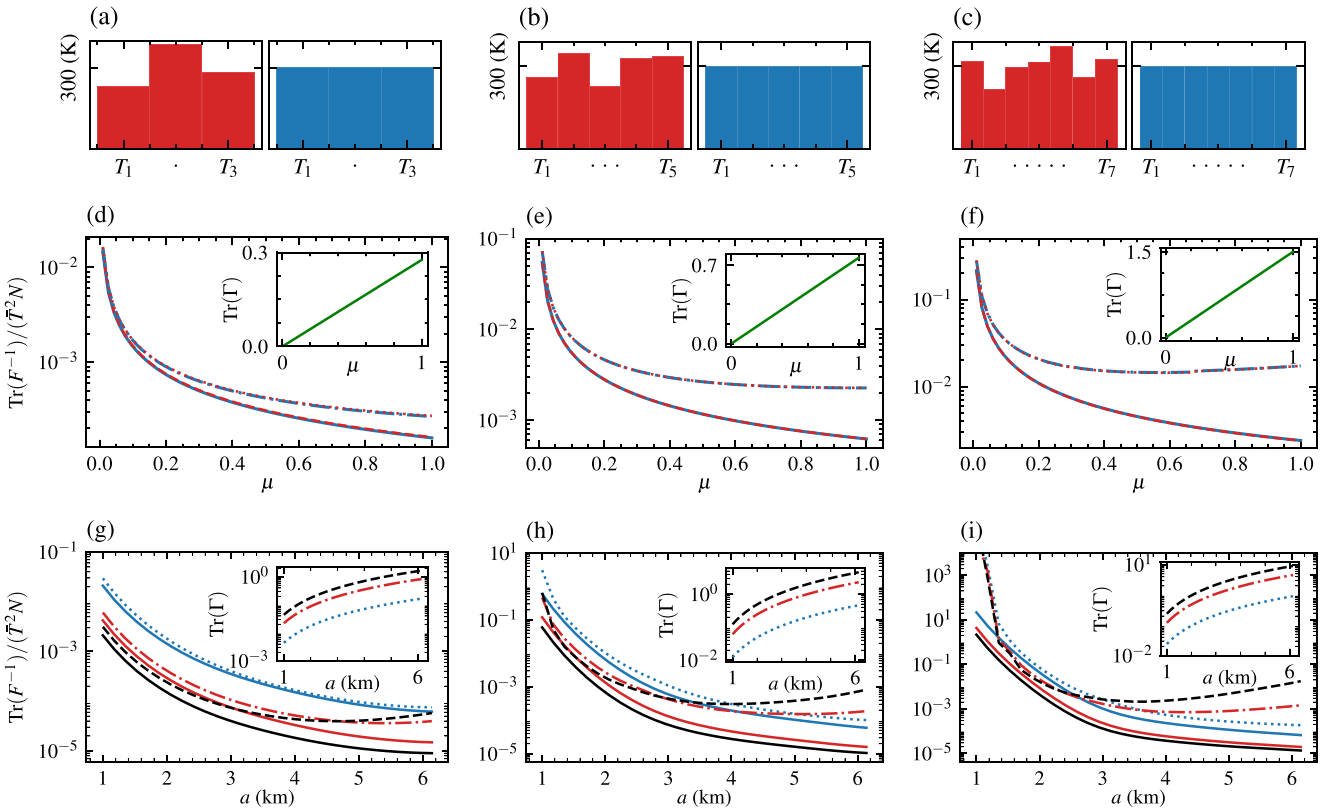

FIG. 3. (a)–(c) The temperature distribution of the 1D pixels with uniform temperature (blue bars) and different temperatures (red bars) for three, five, and seven pixels of the sources from (a) to (c), respectively. (d)–(f) The scalar CRBs (dimensionless) as a function of μ for the number of source pixels corresponding to (a)–(c). The solid blue and dashed red curves describe the QCRBs, and dotted red curves and dashed dotted blue curves describe the CCRBs for uniform and random temperature configurations. The insets show the total photon number as a function of μ with a solid green line. The pixel size for (d)–(f) is 2.5 km. (g)–(i) The scalar CRBs as a function of the source size a. The blue, red, and black lines correspond to different $\mu = (0.1, 0.5, 1.0)$, respectively. The solid lines represent the QCRBs, and dashed, dash-dotted, and dotted lines represent the scalar CCRBs of single-photon measurements with optimized unitary specific to different pixel configurations. The insets show the total photon number in the detector as a function of pixel size a, with the corresponding color of different μ. The average temperatures are assumed to be $\bar{T} = 300$ K, and the sample size is set to be $N = 10^6$.

The unitary $\mathbf{U}$ becomes a $n_x \times n_x$ matrix, and we need n_x^2 real parameters. Varying all the parameters of $\mathbf{U}$ independently to find a minimum for our cost function is a difficult task. Therefore, for $n > 2$, we use the steepest decent algorithm to minimize the most informative bound in Eq. (19). An efficient algorithm to minimize a given cost function with an argument of the Lie group of unitary matrices $U(n)$ is proposed in Ref. [94]. The unitary group $U(n)$ is a real Lie group of dimension n^2. In each iteration step, the conjugate gradient (CG) algorithm moves towards a minimum along the geodesic on the Riemannian manifold, corresponding to a straight line in Euclidean space. We explain the details of the CG algorithm adapted from Refs. [94–97] in the Appendix. These types of algorithms are widely used in classical communication systems. This paper uses the algorithm to optimize the POVM to achieve the quantum limit for imaging in passive remote sensing. We verified numerically that for our choice of the parameter set, the SLDs for different parameters commute on average over the corresponding quantum state for the n-mode interferometer.

In Fig. 3, we analyze the QCRB and the CCRB for different numbers of source pixels p_x (3, 5, and 7). The average temperatures are fixed to $\bar{T} = 300$ K for both random temperature distributions (left, red bars) and the uniform temperature distribution of the pixel sources (right, blue bars). From Figs. 3(d)–3(f), we show how the classical bounds from our measurement with optimized unitary change as a function of μ; insets show the changes of the corresponding total photon numbers as a function of μ in each configuration. Since the total mean photon number of the detection modes (solid green lines) decreases with μ and tends to $\mathrm{Tr}(\Gamma) \ll 1$, the POVMs of single-photon detections (red dotted and blue dash-dotted) saturate the QCRBs (red dashed and solid blue) for different and uniform temperature configurations, respectively. When $\mathrm{Tr}(\Gamma)$ gets close to 1, we see that the gap between the QCRB and the CCRB for single-photon measurement with optimized unitary ($\mathbf{U}_{\mathrm{opt}}$) increases. Additionally, the QCRBs decrease as the number of photons increases with μ, which means more photons from each pixel increase the QFI of the parameters. Thus, one needs to perform photon-number measurements rather than just single-photon ones to achieve the QCRB in this limit. Increasing the number of pixels p increases the total photon number on the interferometer. Thus the gap between the QCRBs and the CCRBs for measurement

with optimized $\mathbf{U}_{\text{opt}}$ in each figure from Fig. 3(d) to Fig. 3(f) increases.

In Figs. 3(g)–3(i), we compare how both bounds change as a function of source size a for different temperature configurations. The black, red, and blue solid lines provide the QCRBs, and dashed black, dot-dashed red, and dotted blue provide the CRBs for single-photon POVMs measurement for different μ (0.1, 0.5, 1.0), respectively. Further, the insets provide the total photon numbers in the detection modes. We observe that the blue dotted lines ($\mu = 0.1$) are very close to the quantum limit and almost saturate the QCRBs for each source configuration for different source sizes. Once we increase μ, the gap between the two bounds increases as a function of source size a due to the increased number of photons. For instance, compare the gap for black dashed lines ($\mu = 1.0$) and blue dotted lines ($\mu = 0.1$). This is due to the limitation of the single-photon statistics for sources with a total photon number greater than 1 [$\text{Tr}(\Gamma) > 1$].

In general, the optimal unitary depends on the parameters (temperature distributions) we want to estimate. However, in real-life cases, we need to gain knowledge of the parameters to optimize the unitary completely. As we discuss in the section on two-pixel sources, a unitary for uniform temperature distributions can also be used to estimate different temperatures with the same $\bar{T}$ value. Experimentally, one can estimate the average temperature separately and construct the optimized unitary for the uniform temperature distribution ($\mathbf{U}_{\text{opt}}^{\text{uniform}}$). One then uses it to estimate the actual nonuniform temperature distribution. Further, we examine how both bounds change as a function of the number of pixels (p_x). In Fig. 4, we show the CCRBs for different $\mu = (0.05, 0.1, 0.5, 1.0)$ in Figs. 4(a)–4(d), respectively. The blue circles represent the initial random unitary for the CG algorithm. The black triangles are the scalar QCRBs. The red upward wedges are the scalar CCRBs from the optimized unitary ($\mathbf{U}_{\text{opt}}^{\text{image}}$) specific to random temperature distributions of pixels. Further, the green downward wedges are for the optimized unitary for uniform temperature distributions ($\mathbf{U}_{\text{opt}}^{\text{uniform}}$) of the pixels, used to estimate the corresponding random unitary temperature distributions with the same pixel number and the same average temperatures. The bounds from $\mathbf{U}_{\text{opt}}^{\text{uniform}}$ (green wedges) and $\mathbf{U}_{\text{opt}}^{\text{image}}$ (red wedges) are very close to each other in this logarithmic scale. Also, both almost saturate the QCRBs for $\mu = 0.05$ and 0.1 for different p_x. When we raise the number of pixels (p_x), we see that all bounds increase. Moreover, the gap between QCRBs and CCRBs from single-photon measurements becomes more significant for $\mu = 0.5$ and 1.0 compared to $\mu = 0.1$.

C. Resolution of 2D sources

This section considers an image with a total number of pixels $p = p_x p_y$ on the image plane. The number n of the modes of the 2D array interferometers will be considered the same as p, with $n = n_x n_y$. The size of each pixel is set to $a = 3$ km, which is around ten times smaller than the spatial resolution of SMOS considering the van Cittert–Zernike theorem, and the separation between the two nearest pixels is again set to zero. The parameters that we want to estimate are the temperatures of the 2D image $\boldsymbol{\theta} = \{T_1, T_2, \ldots, T_p\}$. We consider the case

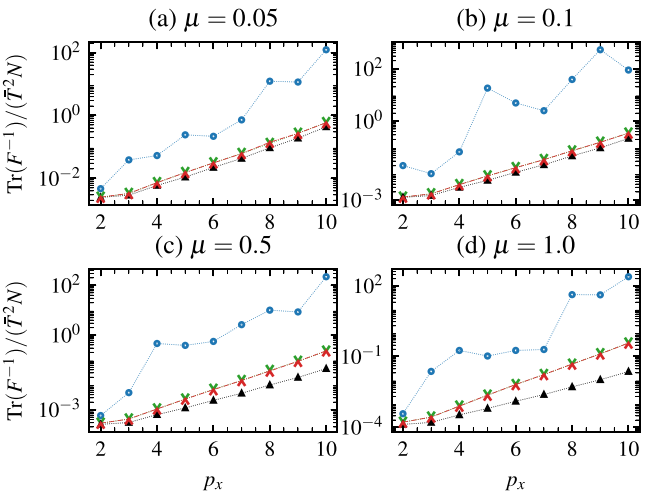

FIG. 4. (a)–(d) The scalar CRBs (dimensionless) for different numbers of pixels p_x along the $\hat{x}$ axis in a 1D array and $\mu = (0.05, 0.1, 0.5, 1.0)$, respectively. The black triangles represent QCRBs, and red upward wedges represent the scalar CCRBs that we get using the optimized unitary $\mathbf{U}_{\text{opt}}^{\text{image}}$ specific to the actual temperature distributions of source pixels. Green downward wedges are for the unitary $\mathbf{U}_{\text{opt}}^{\text{uniform}}$ optimized for the uniform temperature of the pixels used to estimate the actual temperature distribution with the same average temperature. Blue circles correspond to scalar CRBs for the initial random unitary before optimization. Pixel size is $a = 2.5$ km, average temperature $\bar{T} = 300$ K, and sample size $N = 10^6$.

of drastic photon losses and set $\mu = 0.01$, which for $\bar{T} \approx 293$ K gives the total photon number around $\text{Tr}(\Gamma) \simeq 0.39$. In Fig. 5(a), we consider an actual image of $\hbar$ using 30 pixels on the image plane and a 30-mode interferometer on the source plane. The unitary optimized ($\mathbf{U}_{\text{opt}}^{\text{image}}$) for this image or the unitary for a uniform temperatures distribution ($\mathbf{U}_{\text{opt}}^{\text{uniform}}$) is applied in the preprocessing stage to estimate the parameters. For the classical measurement, we consider a local measurement scenario with $\mathbf{U} = \mathbb{I}$. Further, the image from different measurement strategies is reconstructed by using a maximum likelihood estimator for a sample of size N. In Fig. 5(b), we reconstructed the image by using $\mathbf{U}_{\text{opt}}^{\text{image}}$. We have the advantage of the nonlocal measurement and the optimized unitary specific to the image. The reconstructed image is close to the actual image for this parameter regime. Though this unitary depends on the parameter set, we estimate that the same resolution limit may be achieved using adaptive types of measurement [98] by iteratively updating the unitary for each sample after measurement.

However, this is beyond the scope of this paper. On the other hand, for easy experimental realization, we reconstruct the image by using $\mathbf{U}_{\text{opt}}^{\text{uniform}}$ in Fig. 5(c). One can independently estimate the average temperature from the source distribution and construct this general unitary for any image. As we see, the reconstructed image still reveals the actual image nicely, but as expected, it is not as sharp as the image from a specifically optimized unitary. We reconstructed the image from local measurement in Fig. 5(d). Clearly, this reconstructed image is not close to the original one. This is

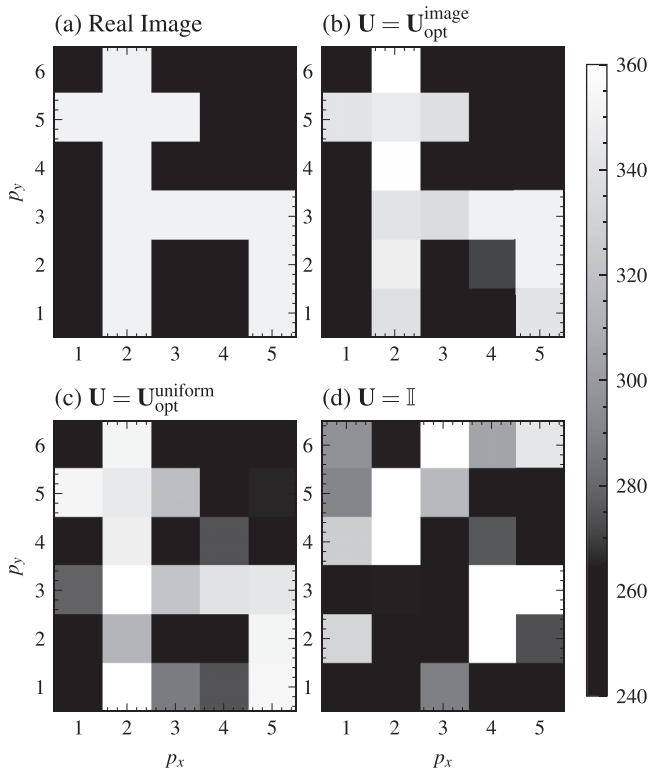

FIG. 5. (a) The image on the source plane with 30 pixels will be estimated using a maximum likelihood estimator. (b) The reconstructed image after single-photon detection in detection modes $\hat{d}_i$ obtained from using the optimized unitary $\mathbf{U}_{\text{opt}}^{\text{image}}$ specific to the temperature distribution. (c) The reconstructed image using a unitary optimized for uniform temperature distribution $\mathbf{U}_{\text{opt}}^{\text{uniform}}$. (d) The reconstructed image using a local measurement of single photons considering $\mathbf{U} = \mathbb{I}$. Pixel size $a = 3.0$ km, average temperature $\bar{T} \approx 293$ K, and sample size $N = 10^8$.

expected for our pixel size $a = 3$ km, well below the limit of the Rayleigh resolution for SMOS, which is around 35 km, based on the van Cittert–Zernike theorem [48–51].

IV. CONCLUSION

In summary, we formulated passive remote sensing as a quantum multiparameter estimation problem, where we focused on the temperatures on the ground as parameters rather than geometrical information of sources that are currently at the center of attention in quantum imaging, such as the separation, centroid, or phases of sources. An antenna array with as many antennas as desired pixels in the source plane receives thermal electromagnetic radiation in receiver modes that are then mixed according to an optimized unitary transformation. Single-photon detectors detect the photons in the corresponding optimized detection modes. The function to be optimized is a scalar classical Cramér-Rao bound obtained by contracting the inverse Fisher information matrix for estimating the temperatures from the photon-counting results with a positive weight matrix. With the latter one we can give different preferences for high resolution to different parts of the image. The optimization of the bound over all unitary mode mixings leads to a "most-informative bound [55]." For a uniform weight over all pixels, we show that with this procedure, one can, in the case of the Gaussian white-noise characteristic of thermal states, approximatively saturate the scalar quantum Cramér-Rao bound based on the contraction of the quantum Fisher information matrix for the multiparameter estimation problem with the same positive weight matrix (chosen as the identity in the present paper). In principle, the optimized unitary depends on the actual temperature distribution, but we showed that the unitary obtained from a uniform temperature distribution gives still much better resolution than direct photon counting in the incoming modes. For the optimization over the unitaries, we used a conjugate gradient algorithm. We showed that the found optimal mode of mixing, followed by single-photon detection, leads to a spatial resolution of the reconstructed images that are at least about an order of magnitude better than Rayleigh's limit (about 3 km instead of 35 km for an antenna array comparable with the

Algorithm 1. Conjugate gradient algorithm for unitary optimization

Require: $k = 0$, $\mathbf{U}_k = $ Random Unitary, $n = \mathbf{dim}(\mathbf{U}_k)$, $\alpha = 1$
while $k \neq k_{\max}$ **do**
  if k modulo $n^2 = 0$ **then**
    $\mathbf{G}_k = \frac{\partial}{\partial \mathbf{U}^*} F(\mathbf{U}_k)$
    $\mathbf{W}_k = \mathbf{G}_k \mathbf{U}_k^\dagger - \mathbf{U}_k \mathbf{G}_k^\dagger$
    $\mathbf{H}_k := \mathbf{W}_k$
  else
    $\mathbf{W}_k \leftarrow \mathbf{W}_{k+1}$
    $\mathbf{H}_k \leftarrow \mathbf{H}_{k+1}$
  end if

  $\mathbf{P}_k = \exp(-\alpha \mathbf{H}_k)$
  $\mathbf{Q}_k = \mathbf{P}_k \mathbf{P}_k$

  while $F(\mathbf{U}_k) - F(\mathbf{Q}_k \mathbf{U}_k) \geq \alpha \langle \mathbf{W}_k, \mathbf{H}_k \rangle$ **do**
    $\mathbf{P}_k = \mathbf{Q}_k$
    $\mathbf{Q}_k = \mathbf{P}_k \mathbf{P}_k$
    $\alpha = 2\mu$
  end while

  while $F(\mathbf{U}_k) - F(\mathbf{P}_k \mathbf{U}_k) < (\alpha/2) \langle \mathbf{W}_k, \mathbf{H}_k \rangle$ **do**
    $\alpha = \alpha/2$
    $\mathbf{P}_k = \exp(-\alpha \mathbf{H}_k)$
  end while

  $\mathbf{U}_{k+1} = \mathbf{P}_k \mathbf{U}_k$
  $\mathbf{G}_{k+1} = \frac{\partial}{\partial \mathbf{U}^*} F(\mathbf{U}_{k+1})$
  $\mathbf{W}_{k+1} = \mathbf{G}_{k+1} \mathbf{U}_{k+1}^\dagger - \mathbf{U}_{k+1} \mathbf{G}_{k+1}^\dagger$
  $\gamma_k := \frac{\langle \mathbf{W}_{k+1} - \mathbf{W}_k, \mathbf{W}_k \rangle}{\langle \mathbf{W}_k, \mathbf{W}_k \rangle}$
  $\mathbf{H}_{k+1} = \mathbf{W}_{k+1} + \gamma_k \mathbf{H}_k$

  if $\langle \mathbf{W}_{k+1}, \mathbf{H}_{k+1} \rangle \leq 0$ **then**
    $\mathbf{H}_{k+1} = \mathbf{W}_{k+1}$
  end if

  $\mathbf{U}_k \leftarrow \mathbf{U}_{k+1}$
  $k \leftarrow k + 1$
end while

one of SMOS, even for substantial photon losses), given in the present case by the van Cittert–Zernike theorem. The optimal unitary can be decomposed into $SU(2)$ group elements using beam splitters and phase shifters and can be realized as linear optical quantum computing. Given the recent availability of single-photon detection in the microwave domain, our results show a path towards substantially enhanced resolution in passive remote sensing compared to classical interferometers that essentially implement homodyne quadrature measurements. Further improvements might be possible for larger photon numbers or smaller losses if photon-number resolved measurements are available.

ACKNOWLEDGMENTS

D.B. and E.K. are grateful for support by Deutsche Forschungsgemeinschaft Project No. BR 52213-1. We thank Gerardo Adesso for discussions, and D.B. thanks Yann Kerr, Bernard Rougé, and the entire SMOS team in Toulouse for valuable insights into that mission.

APPENDIX: CONJUGATE GRADIENT ALGORITHM FOR OPTIMIZATION

This section summarizes a practical CG algorithm given by Refs. [94,96,97]. The generic CG algorithm starts with $(k = 0)$ finding the conjugate gradient $\mathbf{G}_k$ of the cost function $F(\mathbf{U}_k)$ for an initial unitary matrix, where

$$\mathbf{G}_k = \frac{\partial}{\partial \mathbf{U}^*} F(\mathbf{U}_k). \tag{A1}$$

Then, the Riemannian gradient $\mathbf{W}_k$ at that point can be found by

$$\mathbf{W}_k = \mathbf{G}_k \mathbf{U}_k^\dagger - \mathbf{U}_k \mathbf{G}_k^\dagger. \tag{A2}$$

By determining the step size α using the Armijo method (see Ref. [95]) along the geodesic direction (in the direction of $-\mathbf{H}_k$), one can update the unitary by

$$\mathbf{U}_{k+1} = \exp(-\alpha \mathbf{H}_k)\mathbf{U}_k. \tag{A3}$$

Further, the new search direction can be found by using the Polak-Ribierre formula $\mathbf{H}_{k+1} = \mathbf{W}_{k+1} + \boldsymbol{\gamma}_k \mathbf{H}_k$, where

$$\boldsymbol{\gamma}_k := \frac{\langle \mathbf{W}_{k+1} - \mathbf{W}_k, \mathbf{W}_k \rangle}{\langle \mathbf{W}_k, \mathbf{W}_k \rangle}. \tag{A4}$$

The inner product defined as $\langle X, Y \rangle \equiv \mathrm{Tr}(X^\dagger Y)/2$ induces a bi-invariant metric on the unitary group $U(n)$. We reset the search direction periodically to ensure the direction of $\mathbf{H}_k$ is a descent direction. Then the next iteration continues accordingly (see pseudocode in Algorithm 1). The algorithm runs until it converges to a minimum value of the cost function or a maximum number of iterations $k_{\max}$. To efficiently deal with the gradient of the cost functions, we used the PYTORCH gradient function. PYTORCH is used in machine learning for its GPU capabilities.

[1] A. Bhandari, A. Kadambi, and R. Raskar, *Computational Imaging* (MIT, Cambridge, MA, 2022).
[2] R. Hanbury Brown and R. Q. Twiss, A test of a new type of stellar interferometer on sirius, Nature (London) **178**, 1046 (1956).
[3] U. Fano, Quantum theory of interference effects in the mixing of light from phase-independent sources, Am. J. Phys. **29**, 539 (1961).
[4] S. W. Hell and J. Wichmann, Breaking the diffraction resolution limit by stimulated emission: Stimulated-emission-depletion fluorescence microscopy, Opt. Lett. **19**, 780 (1994).
[5] S. W. Hell, Far-field optical nanoscopy, Science **316**, 1153 (2007).
[6] C. W. Helstrom, Detection theory and quantum mechanics, Inform. Comput. **10**, 254 (1967).
[7] C. W. Helstrom, Quantum detection and estimation theory, J. Stat. Phys. **1**, 231 (1969).
[8] C. W. Helstrom, Cramer-Rao inequalities for operator-valued measures in quantum mechanics, Int. J. Theor. Phys. **8**, 361 (1973).
[9] C. W. Helstrom, Estimation of object parameters by a quantum-limited optical system, J. Opt. Soc. Am. **60**, 233 (1970).
[10] O. Pinel, J. Fade, D. Braun, P. Jian, N. Treps, and C. Fabre, Ultimate sensitivity of precision measurements with intense Gaussian quantum light: A multimodal approach, Phys. Rev. A **85**, 010101(R) (2012).
[11] O. Pinel, P. Jian, N. Treps, C. Fabre, and D. Braun, Quantum parameter estimation using general single-mode Gaussian states, Phys. Rev. A **88**, 040102(R) (2013).
[12] M. Tsang, Quantum limit to subdiffraction incoherent optical imaging, Phys. Rev. A **99**, 012305 (2019).
[13] S. Zhou and L. Jiang, Modern description of Rayleigh's criterion, Phys. Rev. A **99**, 013808 (2019).
[14] G. Sorelli, M. Gessner, M. Walschaers, and N. Treps, Moment-based superresolution: Formalism and applications, Phys. Rev. A **104**, 033515 (2021).
[15] J. Řehaček, Z. Hradil, B. Stoklasa, M. Paúr, J. Grover, A. Krzic, and L. L. Sánchez-Soto, Multiparameter quantum metrology of incoherent point sources: Towards realistic superresolution, Phys. Rev. A **96**, 062107 (2017).
[16] C. Napoli, S. Piano, R. Leach, G. Adesso, and T. Tufarelli, Towards Superresolution Surface Metrology: Quantum Estimation of Angular and Axial Separations, Phys. Rev. Lett. **122**, 140505 (2019).
[17] R. Nair and M. Tsang, Far-Field Superresolution of Thermal Electromagnetic Sources at the Quantum Limit, Phys. Rev. Lett. **117**, 190801 (2016).
[18] C. Lupo and S. Pirandola, Ultimate Precision Bound of Quantum and Subwavelength Imaging, Phys. Rev. Lett. **117**, 190802 (2016).
[19] W. Larson and B. E. A. Saleh, Resurgence of Rayleigh's curse in the presence of partial coherence, Optica **5**, 1382 (2018).

[20] S. Kurdziałek and R. Demkowicz-Dobrzański, Super-resolution optical fluctuation imaging: Fundamental estimation theory perspective, J. Opt. **23**, 075701 (2021).

[21] M. I. Kolobov and C. Fabre, Quantum Limits on Optical Resolution, Phys. Rev. Lett. **85**, 3789 (2000).

[22] S. Z. Ang, R. Nair, and M. Tsang, Quantum limit for two-dimensional resolution of two incoherent optical point sources, Phys. Rev. A **95**, 063847 (2017).

[23] M. Tsang, Quantum Nonlocality in Weak-Thermal-Light Interferometry, Phys. Rev. Lett. **107**, 270402 (2011).

[24] E. Bisketzi, D. Branford, and A. Datta, Quantum limits of localisation microscopy, New J. Phys. **21**, 123032 (2019).

[25] M. Bojer, Z. Huang, S. Karl, S. Richter, P. Kok, and J. von Zanthier, A quantitative comparison of amplitude versus intensity interferometry for astronomy, New J. Phys. **24**, 043026 (2021).

[26] C. Datta, M. Jarzyna, Y. L. Len, K. Łukanowski, J. Kołodyński, and K. Banaszek, Sub-Rayleigh resolution of two incoherent sources by array homodyning, Phys. Rev. A **102**, 063526 (2020).

[27] J. O. de Almeida, J. Kołodyński, C. Hirche, M. Lewenstein, and M. Skotiniotis, Discrimination and estimation of incoherent sources under misalignment, Phys. Rev. A **103**, 022406 (2021).

[28] K. Liang, S. A. Wadood, and A. N. Vamivakas, Coherence effects on estimating general sub-rayleigh object distribution moments, Phys. Rev. A **104**, 022220 (2021).

[29] M. Tsang, Subdiffraction incoherent optical imaging via spatial-mode demultiplexing, New J. Phys. **19**, 023054 (2017).

[30] M. Tsang, Quantum limits to optical point-source localization, Optica **2**, 646 (2015).

[31] I. Karuseichyk, G. Sorelli, M. Walschaers, N. Treps, and M. Gessner, Resolving mutually-coherent point sources of light with arbitrary statistics, Phys. Rev. Res. **4**, 043010 (2022).

[32] C. Lupo, Z. Huang, and P. Kok, Quantum Limits to Incoherent Imaging are Achieved by Linear Interferometry, Phys. Rev. Lett. **124**, 080503 (2020).

[33] D. Gottesman, T. Jennewein, and S. Croke, Longer-Baseline Telescopes Using Quantum Repeaters, Phys. Rev. Lett. **109**, 070503 (2012).

[34] E. T. Khabiboulline, J. Borregaard, K. De Greve, and M. D. Lukin, Optical Interferometry with Quantum Networks, Phys. Rev. Lett. **123**, 070504 (2019).

[35] Y. Wang, Y. Zhang, and V. O. Lorenz, Superresolution in interferometric imaging of strong thermal sources, Phys. Rev. A **104**, 022613 (2021).

[36] C. Datta, Y. L. Len, K. Łukanowski, K. Banaszek, and M. Jarzyna, Sub-Rayleigh characterization of a binary source by spatially demultiplexed coherent detection, Opt. Express **29**, 35592 (2021).

[37] M. P. Backlund, Y. Shechtman, and R. L. Walsworth, Fundamental Precision Bounds for Three-Dimensional Optical Localization Microscopy with Poisson Statistics, Phys. Rev. Lett. **121**, 023904 (2018).

[38] M. Mazelanik, A. Leszczynski, and M. Parniak, Optical-domain spectral super-resolution enabled by a quantum memory, Nat. Commun. **13**, 691 (2021).

[39] M. Paúr, B. Stoklasa, Z. Hradil, L. L. Sánchez-Soto, and J. Rehacek, Achieving the ultimate optical resolution, Optica **3**, 1144 (2016).

[40] A. A. Pushkina, G. Maltese, J. I. Costa-Filho, P. Patel, and A. I. Lvovsky, Super-Resolution Linear Optical Imaging in the Far Field Phys. Rev. Lett. **127**, 253602 (2021).

[41] P. Boucher, C. Fabre, G. Labroille, and N. Treps, Spatial optical mode demultiplexing as a practical tool for optimal transverse distance estimation, Optica **7**, 1621 (2020).

[42] G. Sorelli, M. Gessner, M. Walschaers, and N. Treps, Optimal Observables and Estimators for Practical Superresolution Imaging, Phys. Rev. Lett. **127**, 123604 (2021).

[43] P. C. Humphreys, M. Barbieri, A. Datta, and I. A. Walmsley, Quantum Enhanced Multiple Phase Estimation, Phys. Rev. Lett. **111**, 070403 (2013).

[44] C. N. Gagatsos, D. Branford, and A. Datta, Gaussian systems for quantum-enhanced multiple phase estimation, Phys. Rev. A **94**, 042342 (2016).

[45] P. A. Knott, T. J. Proctor, A. J. Hayes, J. F. Ralph, P. Kok, and J. A. Dunningham, Local versus global strategies in multiparameter estimation, Phys. Rev. A **94**, 062312 (2016).

[46] L. Pezzè, M. A. Ciampini, N. Spagnolo, P. C. Humphreys, A. Datta, I. A. Walmsley, M. Barbieri, F. Sciarrino, and A. Smerzi, Optimal Measurements for Simultaneous Quantum Estimation of Multiple Phases, Phys. Rev. Lett. **119**, 130504 (2017).

[47] E. Köse, G. Adesso, and D. Braun, Quantum-enhanced passive remote sensing, Phys. Rev. A **106**, 012601 (2022).

[48] E. Anterrieu, A resolving matrix approach for synthetic aperture imaging radiometers, IEEE Trans. Geosci. Remote Sens. **42**, 1649 (2004).

[49] I. Corbella, N. Duffo, M. Vall-llossera, A. Camps, and F. Torres, The visibility function in interferometric aperture synthesis radiometry, IEEE Trans. Geosci. Remote Sens. **42**, 1677 (2004).

[50] D. Le Vine, Synthetic aperture radiometer systems, IEEE Trans. Microwave Theory Techn. **47**, 2228 (1999).

[51] A. R. Thompson, J. M. Moran, and George W. Swenson, Jr., *Interferometry and Synthesis in Radio Astronomy* (Springer, New York, 2017).

[52] P. van Cittert, Die wahrscheinliche schwingungsverteilung in einer von einer lichtquelle direkt oder mittels einer linse beleuchteten ebene, Physica **1**, 201 (1934).

[53] F. Zernike, The concept of degree of coherence and its application to optical problems, Physica **5**, 785 (1938).

[54] D. Braun, Y. Monjid, B. Rougé, and Y. Kerr, Generalization of the Van Cittert–Zernike theorem: Observers moving with respect to sources, Meas. Sci. Technol. **27**, 015002 (2016).

[55] F. Albarelli, M. Barbieri, M. Genoni, and I. Gianani, A perspective on multiparameter quantum metrology: From theoretical tools to applications in quantum imaging, Phys. Lett. A **384**, 126311 (2020).

[56] P. Kok, W. J. Munro, K. Nemoto, T. C. Ralph, J. P. Dowling, and G. J. Milburn, Linear optical quantum computing with photonic qubits, Rev. Mod. Phys. **79**, 135 (2007).

[57] T. Baumgratz and A. Datta, Quantum Enhanced Estimation of a Multidimensional Field, Phys. Rev. Lett. **116**, 030801 (2016).

[58] E. Bagan, M. A. Ballester, R. D. Gill, A. Monras, and R. Muñoz-Tapia, Optimal full estimation of qubit mixed states, Phys. Rev. A **73**, 032301 (2006).

[59] M. Guta and J. Kiukas, Information geometry and local asymptotic normality for multi-parameter estimation of quantum Markov dynamics, J. Math. Phys. **58**, 052201 (2017).

[60] M. Szczykulska, T. Baumgratz, and A. Datta, Multi-parameter quantum metrology, Adv. Phys.: X **1**, 621 (2016).
[61] S. Ragy, M. Jarzyna, and R. Demkowicz-Dobrzański, Compatibility in multiparameter quantum metrology, Phys. Rev. A **94**, 052108 (2016).
[62] D. Braun, Y. Monjid, B. Rougé, and Y. Kerr, Fourier-correlation imaging, J. Appl. Phys. **123**, 074502 (2018).
[63] J. Liu, H. Yuan, X.-M. Lu, and X. Wang, Quantum Fisher information matrix and multiparameter estimation, J. Phys. A: Math. Theor. **53**, 023001 (2020).
[64] J. Shapiro, The quantum theory of optical communications, IEEE J. Sel. Top. Quantum Electron. **15**, 1547 (2009).
[65] C. Oh, S. Zhou, Y. Wong, and L. Jiang, Quantum Limits of Superresolution in a Noisy Environment, Phys. Rev. Lett. **126**, 120502 (2021).
[66] M. Gessner, C. Fabre, and N. Treps, Superresolution Limits from Measurement Crosstalk, Phys. Rev. Lett. **125**, 100501 (2020).
[67] Y. L. Len, C. Datta, M. Parniak, and K. Banaszek, Resolution limits of spatial mode demultiplexing with noisy detection, Int. J. Quantum. Inform. **18**, 1941015 (2020).
[68] K. J. Blow, R. Loudon, S. J. D. Phoenix, and T. J. Shepherd, Continuum fields in quantum optics, Phys. Rev. A **42**, 4102 (1990).
[69] L. Mandel, and E. Wolf, *Optical Coherence and Quantum Optics* (Cambridge University Press, Cambridge, 1995).
[70] R. J. Glauber, Coherent and incoherent states of the radiation field, Phys. Rev. **131**, 2766 (1963).
[71] M. O. Scully, and M. S. Zubairy, *Quantum Optics* (Cambridge University Press, Cambridge, 1997).
[72] R. Loudon and T. von Foerster, The quantum theory of light, Am. J. Phys. **42**, 1041 (1974).
[73] R. Kubo, The fluctuation-dissipation theorem, Rep. Prog. Phys. **29**, 255 (1966).
[74] S. Savasta, O. Di Stefano, and R. Girlanda, Light quantization for arbitrary scattering systems, Phys. Rev. A **65**, 043801 (2002).
[75] E. A. Sharkov, *Passive Microwave Remote Sensing of the Earth: Physical Foundations* (Springer-Verlag, Berlin, 2011).
[76] L. D. Landau, and E. M. Lifshits, *Statistical Physics* (Elsevier Science, 1980), Vol. 5.
[77] R. Carminati and J.-J. Greffet, Near-Field Effects in Spatial Coherence of Thermal Sources, Phys. Rev. Lett. **82**, 1660 (1999).
[78] J. Zmuidzinas, Cramér–Rao sensitivity limits for astronomical instruments: Implications for interferometer design, J. Opt. Soc. Am. A **20**, 218 (2003).
[79] J. Zmuidzinas, Thermal noise and correlations in photon detection, Appl. Opt. **42**, 4989 (2003).
[80] J. S. Sidhu and P. Kok, Geometric perspective on quantum parameter estimation, AVS Quantum Sci. **2**, 014701 (2020).
[81] Y. Gao and H. Lee, Bounds on quantum multiple-parameter estimation with Gaussian state, Eur. Phys. J. D **68**, 347 (2014).
[82] D. Braun, P. Jian, O. Pinel, and N. Treps, Precision measurements with photon-subtracted or photon-added Gaussian states, Phys. Rev. A **90**, 013821 (2014).
[83] G. Adesso, S. Ragy, and A. R. Lee, Continuous variable quantum information: Gaussian states and beyond, Open Syst. Inf. Dyn. **21**, 1440001 (2014).
[84] S. Olivares, Quantum optics in the phase space: A tutorial on Gaussian states, Eur. Phys. J. Spec. Top. **203**, 3 (2012).
[85] C. Weedbrook, S. Pirandola, R. García-Patrón, N. J. Cerf, T. C. Ralph, J. H. Shapiro, and S. Lloyd, Gaussian quantum information, Rev. Mod. Phys. **84**, 621 (2012).
[86] S. L. Braunstein and C. M. Caves, Statistical distance and the geometry of quantum states, Phys. Rev. Lett. **72**, 3439 (1994).
[87] M. G. A. Paris, Quantum estimation for quantum technology, Int. J. Quantum. Inform. **07**, 125 (2009).
[88] A. Holevo, Statistical decision theory for quantum systems, J. Multivariate Anal. **3**, 337 (1973).
[89] M. Tsang, F. Albarelli, and A. Datta, Quantum Semiparametric Estimation, Phys. Rev. X **10**, 031023 (2020).
[90] I. J. Myung, Tutorial on maximum likelihood estimation, J. Math. Psychol. **47**, 90 (2003).
[91] M. Paris and J. Řeháček, *Quantum State Estimation* (Springer Berlin, Heidelberg, 2004).
[92] R. Nichols, P. Liuzzo-Scorpo, P. A. Knott, and G. Adesso, Multiparameter Gaussian quantum metrology, Phys. Rev. A **98**, 012114 (2018).
[93] R. Yousefjani, R. Nichols, S. Salimi, and G. Adesso, Estimating phase with a random generator: Strategies and resources in multiparameter quantum metrology, Phys. Rev. A **95**, 062307 (2017).
[94] T. Abrudan, J. Eriksson, and V. Koivunen, Conjugate gradient algorithm for optimization under unitary matrix constraint, Signal Process. **89**, 1704 (2009).
[95] T. Abrudan, J. Eriksson, and V. Koivunen, Efficient line search methods for Riemannian optimization under unitary matrix constraint, in *Proceedings of the 2007 Conference Record of the Forty-First Asilomar Conference on Signals, Systems and Computers* (IEEE, New York, 2007), pp. 671–675.
[96] T. E. Abrudan, J. Eriksson, and V. Koivunen, Steepest descent algorithms for optimization under unitary matrix constraint, IEEE Trans. Signal Process. **56**, 1134 (2008).
[97] T. Abrudan, J. Eriksson, and V. Koivunen, Efficient Riemannian algorithms for optimization under unitary matrix constraint, in *Proceedings of the 2008 IEEE International Conference on Acoustics, Speech and Signal Processing* (IEEE, New York, 2008), pp. 2353–2356.
[98] A. Fujiwara, Strong consistency and asymptotic efficiency for adaptive quantum estimation problems, J. Phys. A: Math. Theor. **44**, 079501 (2011).